Proceedings of

MMM

Third International Conference

Multiscale Materials Modeling

September 18-22, 2006, Freiburg, Germany

Symposium 1
Mathematical methods for bridging length and time scales

Peter Gumbsch
Editor and Conference Chair

Organized by Fraunhofer-Institute for Mechanics of Materials.
Hosted by University of Freiburg.

IWM
Fraunhofer Institut Werkstoffmechanik

ALBERT-LUDWIGS-UNIVERSITÄT FREIBURG

Imprint

Papers published in this volume constitute the proceedings of the Third International Conference on Multiscale Materials Modeling. Papers were selected by the program committee for oral or poster presentation. They are published as submitted, in the interest of timely dissemination.

Contact
Fraunhofer Institute for Mechanics of Materials IWM
Woehlerstraße 11
79108 Freiburg
Germany
Phone + 49 761 5142 0
Fax + 49 761 5142 110

The complete proceedings of the conference are available at

Fraunhofer Information-Centre for Regional Planning and Building Construction IRB
P.O. Box 80 04 69, D-70504 Stuttgart
Nobelstrasse 12, D-70569 Stuttgart
Fon +49 (0) 7 11/9 70-25 00
Fax +49 (0) 7 11/9 70-25 07
E-Mail irb@irb.fraunhofer.de
URL www.irb.fraunhofer.de
ISBN-10: 3-8167-7206-4
ISBN-13: 978-3-8167-7206-4

Foreword

Computational modeling of materials behavior by multiscale materials modeling (MMM) approaches is becoming a reliable tool to underpin scientific investigations and to complement traditional theoretical and experimental approaches of component assessment. At transitional (microstructural) scales continuum approaches begin to break down and atomistic methods reach inherent limitations in time and length scale. Transitional theoretical frameworks and modeling techniques are developed to bridge the gap between the different length scales.

Industrial success in high technology fields relies on the possibility to specifically engineer materials and products with improved performance. The success factor is the ability to make these material related developments timely at relatively low-costs. This demands not only the rapid development of new or improved processing techniques but also better understanding and control of material chemistry, processing, structure, performance, durability, and their relationships. This scenario usually involves multiple length and time scales and multiple processing and performance stages, which are usually only accessible via multi-scale / multi-stage modeling or simulation.

In high-payoff, high-risk technologies such as the design of large structures in the aerospace and nuclear industries, the effects of aging and environment on failure mechanisms cannot be left to conservative approaches. Increasing efforts are now focused on advancing MMM approaches to develop new material systems components and devices. Appropriate validation experiments are crucial to verify that the models predict the correct behavior at each length scale. Thus, one of the advantages of these MMM approaches is that, at each scale, physically meaningful parameters are predicted and used in models for subsequent scales, avoiding the use of empiricism and fitting parameters.

Recent interest in nanotechnology is challenging the scientific community to design nanometer to micrometer size devices for applications in new generations of computers, electronics, photonics or drug delivery systems. These new application areas of multiscale materials modeling require novel and sophisticated science-based approaches for design and performance evaluation. Theory and modeling are playing an increasing role to reduce development costs and manufacturing times. With the sustained progress in computational power and MMM methodologies, new materials and new functionalities are increasingly more likely discovered by MMM approaches than by traditional trial and error approach. This is part of a paradigm shift in modeling, away from reproducing known properties of known materials towards simulating the behavior of hypothetical composites as a forerunner to finding real materials with these novel properties.

The MMM 2006 conference provides an international forum for the scientific advances of multiscale modeling methodologies and their applications.

I would like to thank the members of the international advisory committee, the local program committee and particularly the organizing team, the symposium organizers and the session chairs and the University of Freiburg for their engagement and support. Without their hard work and their devotion of time and ressources, the Third International Conference Multiscale Materials Modeling would not have been possible.

Finally, I would like to thank our conference sponsors for their financial support: The German Research Foundation DFG, Accelrys Inc., Plansee S.E. and the Ministry of Science, Research and Art, Baden-Württemberg.

Peter Gumbsch
Conference Chair

Conference Committee

International Advisory Committee

Prof. Bacon, David	University of Liverpool, UK
Dr. Baskes, Michael	Los Alamos National Laboratory, USA
Prof. Busso, Esteban	Imperial College, London, UK
Prof. Cale, Timothy S.	Rensselaer Polytechnic Institute, Troy, USA
Dr. Diaz de la Rubia, Tomas	Lawrence Livermore National Lab., USA
Prof. Ghoniem, Nasr	University of California, Los Angeles, USA
Prof. Guo, Xiao	Queens College, London, UK
Prof. Iwata, Shuichi	University of Tokyo, Japan
Prof. Kratochvil, Jan	Technical University, Prague, Czech Republic
Prof. Kremer, Kurt	Max Planck Institute, Mainz, Germany
Dr. Kubin, Ladislas	ONERA-LEM, Chatillon, France
Dr. LeSar, Richard	Los Alamos National Laboratory, USA
Prof. Meguid, Shaker	University of Toronto, Canada
Prof. Needleman, Alan	Brown University, Providence, USA
Prof. Odette, Robert	University of California, Santa Barbara, USA
Prof. Ortiz, Michael	California Institute of Technology, USA
Prof. Pettifor, David	Oxford University, UK
Prof. Phillips, Robert	California Institute of Technology, USA
Prof. Raabe, Dierk	Max Planck Institute, Düsseldorf, Germany
Prof. Shibutani, Yoji	Osaka University, Japan
Dr. Soneda, Naoki	Komae Research Laboratory, Tokyo, Japan
Prof. Suresh, Subra	Massachusetts Institute of Technology, USA
Prof. Tomita, Yoshihiro	Kobe University, Japan
Prof. Van der Giessen, Erik	University of Groningen, Netherlands
Prof. Walgraef, Daniel	Free University of Brussels, Belgium
Dr. Wolf, Dieter	Argonne National Laboratory, USA
Prof. Yip, Sidney	Massachusetts Institute of Technology, USA
Dr. Zinkle, Steve	Oak Ridge National Laboratory, USA

Organizing Committee

M. J. Alava	Helsinki University of Technology, Finland
D. Dimiduk	The Ohio State University, USA
M. Dao	Massachusetts Institute of Technology, USA
M. Doi	University of Tokyo, Japan
C. Elsässer	Fraunhofer IWM, Germany
E. v. d Giessen	University of Gronigen, Netherlands
N. Gov	The Weizmann Institute of Science, Israel
H. J. Herrmann	University of Stuttgart, Germany
R. James	University of Minnesota, USA
K. Kremer	Max Planck Institute for Polymer Research, Germany
J. Korvink	IMTEK, University of Freiburg, Germany
J. Li	The Ohio State University, USA
S. Müller	Max Planck Institute for Mathematics in the Sciences, Germany
A. Paxton	Queen’s University, Belfast, UK
M. Payne	University of Cambridge, UK
D. Raabe	Max Planck Institute fuer Eisenforschung, Germany
N. Soneda	Central Research Institute of Electric Power Industry, Japan
M. Zaiser	University of Edinburgh , UK
S. Zapperi	University of Rome, Italy
F. Willaime	Commissariat a l’Energie Atomique (CEA), France
B. Wirth	University of California, Berkely, USA

Contents

Symposium 1

Symposium 1

Mathematical methods for bridging length and time scales

Computational Coarse-graining for the strength of materials

Amit Acharya

Civil & Environmental Engineering, Carnegie Mellon University, 15213 Pittsburgh, United States of America

We present an invariant-manifold-theory inspired computational approach to the problem of coarse-graining autonomous system of ODE (fine system). Coarse variables are introduced as either functions of the fine state or time-averages of functions of the fine state. The objective is to come up with a closed theory of evolution for the coarse variables. Application to a model problem in phase transformation (Abeyaratne-Chu-James wiggly energy problem) and strength of materials (Frenkel-Kontorova model) will be demonstrated. We discuss how the method explains the emergence of memory and stochastic effects in coarse response. We then outline a procedure for the selection of a small number of coarse variables that is designed to allow for an autonomous coarse response, thus leading to unambiguous initialization as a function of the coarse state.

Part of this work was done jointly with Aarti Sawant.

Evolution of Interfaces and Boundaries in Solids: Phase Field Models

Hans-Dieter Alber, Zhu Peicheng

Department of Mathematics, Darmstadt University of Technology,
Schlossgartenstraße 7, 64289 Darmstadt, Germany
alber@mathematik.tu-darmstadt.de, zhu@mathematik.tu-darmstadt.de

ABSTRACT

The evolution of phase interfaces in solids showing martensitic transformations and the evolution of interfaces in solids by interface diffusion are usually described by sharp interface models. In simulations it is however advantageous to use diffusive interface models. Such models should also be useful in proving that solutions of the sharp interface models exist. We found that these sharp interface models can indeed be transformed to models with diffusive interfaces. We sketch these transformed models. The models contain evolution equations for the order parameter, which differ from the Allen-Cahn and Cahn-Hilliard equations only by a term containing the gradient of the order parameter.

1. Diffusion dominated and martensitic phase transformations

An interface between different material phases moves if the crystal lattice in front of the interface is transformed from one crystal structure to the other. Such transformation processes can be diffusion dominated or diffusionless. Transformations belonging to the first type are triggered by diffusion processes. An example is the γ–γ' phase transformation in Ni-Al superalloys, where the phase interface is moving by diffusion of aluminium atoms in the crystal lattice.

Diffusionless transformations are also called martensitic. In a material showing martensitic transformations the free energy has local minima at two or more differing configurations of the crystal lattice. The lattice can switch between these configurations without associated diffusion processes. In a particular configuration the material is stress free at the values of the strain tensor corresponding to this configuration of the crystal; since the crystal structure, and hence also these values of the strain tensor, change along the phase interface, this interface is a surface of discontinuity for the stress free strain states. The difference $\overline{\varepsilon}$ of the stress free strain tensors is called transformation strain.

Diffusion dominated phase transformations in solids are often modeled by the Cahn-Hilliard equation coupled with the quasistatic equations of linear elasticity

$$\begin{aligned} -\mathrm{div}_x T(x,t) &= b(x,t), && (1)\\ T(x,t) &= D\big(\varepsilon(\nabla_x u(x,t)) - \overline{\varepsilon} S(x,t)\big), && (2)\\ S_t(x,t) &= c\,\Delta_x\Big(\psi_S(\varepsilon(\nabla_x u(x,t)), S(x,t)) - \nu \Delta_x S(x,t)\Big), && (3)\end{aligned}$$

where $u(x,t) \in \mathbb{R}^3$ is the displacement, $T(x,t)$ is the stress tensor, $S(x,t) \in \mathbb{R}$ is an order parameter, $\varepsilon(\nabla_x u)$ is the strain tensor and D denotes the elasticity tensor. b denotes the given volume force, c and ν are positive constants and ψ_S is the partial derivative of the free energy

$$\psi(\varepsilon, S) = \frac{1}{2}\big(D(\varepsilon - \overline{\varepsilon}S)\big) \cdot (\varepsilon - \overline{\varepsilon}S) + \psi_1(S),$$

where $\psi_1 : \mathbb{R} \to [0,\infty)$ is a double well potential with minima at $S = 0$ and $S = 1$. The phases are characterized by values of the order parameter close to 0 or 1. This model has diffusive phase interfaces, since the order parameter is smooth.

On the other hand, martensitic transformations are usually described by a sharp interface model, which consists of an initial-boundary value problem for the functions u, T and for the unknown phase interface $\tilde{\gamma}(t)$. The different phases are characterized by a discontinuous order parameter S, which only takes the values $S = 0$ and $S = 1$ and which jumps at the interface. The initial-boundary value problem consists of the equation (1) expressing conservation of momentum, of the equation (2) stating the linear stress-strain relations in the two material phases, of suitable boundary and initial conditions and of the interface conditions

$$\begin{aligned} s(x,t)\,[S(x,t)] &= c\,n(x,t)\cdot\big[C(\nabla_x u(x,t), S(x,t))\big]n(x,t), &(4)\\ [u(x,t)] &= 0, \qquad [T(x,t)]n(x,t) = 0, &(5)\end{aligned}$$

which must hold for $x \in \tilde{\gamma}(t)$. Square brackets denote the jump along the interface, $n(x,t) \in \mathbb{R}^3$ is a unit normal vector to the interface oriented such that the jump $[S]$ in the direction of n is positive, and $s(x,t)$ is the normal speed of the interface measured positive in the direction of n. Moreover, $[C]$ denotes the jump of the Eshelby tensor

$$C = \psi(\varepsilon, S)I - (\nabla_x u)^T T.$$

Here I is the identity matrix on $\mathbb{R}^3$ and $(\nabla_x u)^T T$ denotes the matrix product. We have inserted the jump $[S]$ on the left hand side of (4), since in our analysis jumps of $[S]$ different from 1 must be considered.

Equation (4), a constitutive equation, determines the normal speed s of the phase interface as a function of the term $n \cdot [C(\nabla_x u, S)]n$, a configurational force. We assumed that s is proportional to this configurational force, which is the most simple constitutive assumption guaranteeing that the second law of thermodynamics holds, cf. [1]. Thus, in this model the evolution of the phase interface is driven by the configurational forces generated at the interface by the transformation strain, an assumption appropriate for martensitic transformations.

2. Diffusive interface model for martensitic transformations

Models with diffusive phase interfaces have several advantages over models with sharp interfaces. Therefore the question arises, whether it is possible to formulate a diffusive interface model for martensitic phase transformations. In [1, 2] we were able to derive such a model by a rigorous mathematical transformation and regularization of the sharp interface model (1), (2), (4), (5). The final diffusive interface model consists of the equations (1), (2) coupled to the equation

$$S_t = -c\big(\psi_S(\varepsilon, S) - \nu\Delta_x S\big)|\nabla_x S|\,. \tag{6}$$

Note that this equation differs from the Allen-Cahn equation

$$S_t = -c\big(\psi_S(\varepsilon, S) - \nu\Delta_x S\big) \tag{7}$$

only by the gradient term $|\nabla_x S|$. The regularization is chosen such the second law of thermodynamics holds. Existence of solutions of initial-boundary value problems in one space dimension to the transformed model and to the regularized model (1), (2), (6) was proved in [2, 3]. We believe that this diffusive interface model can also be used to study existence of solutions of the sharp interface model (1), (2), (4), (5) in three space dimensions by approximation with smooth solutions of the diffusive interface model. This problem is however open.

3. Diffusive interface model for interface motion by interface diffusion

For both equations (6) and (7) the integral $\int_\Omega S(x,t)dx$ is not conserved in time during the evolution. By a modification of the considerations leading to (6) the equation

$$S_t = c\,\mathrm{div}_x\big(|\nabla_x S|\nabla_x\big(\psi_S - \nu\Delta_x S\big)\big) \tag{8}$$

is obtained, which differs from the Cahn-Hilliard equation (3) only by the gradient term $|\nabla_x S|$, and for which the integral $\int_\Omega S(x,t)dx$ is conserved. In [4] a formal calculation is sketched which shows that solutions of an initial-boundary value problem to the equations (1), (2), (8) converge for $\nu \to 0$ to solutions of a sharp interface problem with the condition (4) replaced by the jump condition

$$s[S] = -c\tilde{\Delta}_x(n \cdot [C]n).$$

Here $\tilde{\Delta}_x$ denotes the surface Laplacian of the interface. Since this sharp interface model describes interface motion by interface diffusion, we surmise that (1), (2), (8) is a phase field model for the evolution of interfaces driven by interface diffusion. In [4] it is proved that the initial-boundary value problem to (1), (2), (8) has solutions in one space dimension.

References

[1] Hans-Dieter Alber: *Evolving microstructure and homogenization.* Continuum Mech. Thermodyn. **12** (2000), 235-287

[2] Hans-Dieter Alber, Zhu Peicheng: *Evolution of phase boundaries by configurational forces.* To appear in Arch. Rational Mech. Anal.

[3] Hans-Dieter Alber, Zhu Peicheng: Solutions to a model with nonuniformly parabolic terms for phase evolution driven by configurational forces. SIAM J. Appl. Math. **66,2** (2006), 680–699

[4] Hans-Dieter Alber, Zhu Peicheng: *Solutions to a model for interface motion by interface diffusion.* Manuskript (2006)

Non-associated flow arising from non-planar dislocation core structures and its effect on macroscopic failure mechanisms

J. L. Bassani, V. Racherla
Mechanical Engineering and Applied Mechanics, University of Pennsylvania, PA 19104;
Email: bassani@seas.upenn.edu

ABSTRACT

In non-close-packed crystalline lattices, e.g. of bcc metals and intermetallics, the stress-state dependence of the Peierls barrier for the motion of a screw dislocation violates Schmid's law and leads to non-associated flow behavior for polycrystalline aggregates (Bassani, 1994; Bassani et al., 2001). Plasticity models based upon distinct yield and flow functions are proposed to describe such behavior and specialized to case of isotropic response. Studies of sheet necking using both a M-K analysis and by finite elements predict that non-associated flow has a significant effect on the evolution of inhomogenieties in the sheet. For nearly rate-insensitive response, intermittent bursts of strain arise for non-associated flow behavior, particularly for deformations near the plane strain state.

1. Introduction

Many experimental and theoretical studies performed in last 50 years have convincingly established that screw dislocations in non-close-packed crystal lattices control essential aspects of plastic deformation due to non-planar dislocation core structures. This includes bcc metals and many intermetallic compounds, and especially their stress-state (including a tension-compression asymmetry), temperature and strain-rate dependencies of plastic flow (see, e.g., Vitek, Pope and Bassani, 1996). In bcc metals the most prominent characteristic of these dislocations is core spreading onto several non-parallel {110} planes containing the <111]> Burgers vector as confirmed by atomistic studies (Vitek et al., 2004). When the dislocation core is non-planar, Schmid's law – which states that glide commences when the resolved shear stress on the slip system reaches a critical value – is no longer valid. In general, and in accord with both atomistic simulations and experiments, non-glide shear stresses (shear stresses on planes other than the slip plane) as well as the Schmid stress determine the Peierls barrier to dislocation motion. Consequently, non-glide stresses must be included in the slip-system yield criteria (Qin and Bassani, 1992a,b; Bassani, 1994; Vitek, et al., 1994; Bassani et al., 2001; Vitek et al., 2004; Groger et al., 2005) .

Qin and Bassani (1992a,b) proposed a model of single crystals incorporating such behaviors that has the structure of a non-associated flow theory of plasticity, i.e. one with a distinct yield function and flow potential (see also Bassani, 1994). They demonstrated a significant affect of non-glide stresses on shear localization in single crystals under both single and multiple slip. In this paper we address aspects of strain localization in polycrystals that undergo non-associated plastic flow. We consider isotropic behavior and utilize recent results of a Taylor calculation for random polycrystals, which demonstrate that the effects of non-glide stresses at the single crystal level persists at macroscopic scales. The predicted yield and flow surfaces for a random bcc polycrystal (based upon slip system yield functions derived from atomistic simulations for Finnis-Sinclair molybdenum) are plotted in Fig. 1 (circles) for plane states of stress (Bassani et al., 2001). It is worth noting that the flow surface is indistinguishable from the yield surface for associated flow behavior (Bishop and Hill, 1951). In the analyses of sheet necking presented in this paper, rather simple yield (F) and flow functions (G) that describe isotropic surfaces are adopted:

$$F = \sqrt{3}\left[\left(J_2\right)^{3/2} + bJ_3\right]^{1/3} = \sqrt{3}\left[\left(\frac{s_{kl}s_{kl}}{2}\right)^{3/2} + b\frac{s_{mn}s_{no}s_{om}}{3}\right]^{1/3} \tag{1}$$

$$G = \sqrt{3J_2} = \sqrt{\frac{3}{2}s_{kl}s_{kl}} \tag{2}$$

where $J_2 = s_{kl}s_{kl}/2$ and $J_3 = s_{ij}s_{jk}s_{ki}/3$ are the second and third invariants of the deviatoric Cauchy stress, s_{ij}. For this simple isotropic theory, the parameter *b* entering the yield function *F* (1.1) is the measure of non-associated flow; *b*=0 is the classical Mises yield function given in (2), which is found to very accurately represent the flow surfaces predicted by the Taylor calculation. These surfaces are plotted as the continuous curves in Fig. 1, with $b = -0.72$ for the least-square best fit to the yield surface. The yield and flow functions (1.1) are used in the sheet necking analyses that are the subject of this paper.

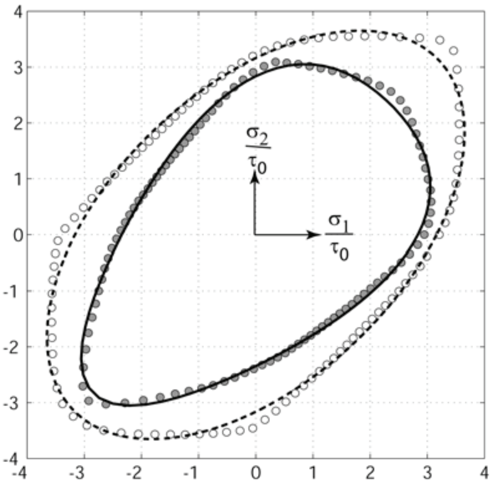

Figure 1. Yield and flow surfaces predicted from a Taylor model for bcc Mo (circles) and fits to F , with *b*=-0.72, and *G* defined in (1).

In materials undergoing strain hardening and associated flow, instabilities are generally a consequence of geometric effects arising from finite deformations. For infinitesimal deformations positive second-order work (SOW), $\overset{\nabla}{\sigma}_{ij} D_{ij} > 0$ (where $\overset{\nabla}{\sigma}_{ij}$ is an appropriate objective rate of Cauchy stress and D_{ij} is the rate of deformation tensor), is a sufficient condition for uniqueness and stability of an initial-boundary-value problem for rate-independent, incrementally linear behavior with smooth yield and flow functions (Hill, 1958; Raniecki, 1979). For non-associated flow, Li and Drucker (1994) have noted that the possibility of negative second-order work can lead to material instabilities even for infinitesimal deformations. One way to offset unstable behavior is to adopt a rate-dependent, non-associated flow theory, which is outline in Sec. 2.

In Sec. 3, the effect of non-associated flow on forming limit strains is studied via M-K analysis with rate-dependent theory, for a moderately large strain-rate sensitivity. Then full three-dimensional finite element analysis of sheet necking are carried out, which allows for a relatively small strain-rate sensitivity to approximate rate-independent behavior. For loading histories near the plane-strain state, an unexpected phenomenon of intermittent strain bursts is predicted, perhaps shedding light on the discontinuous behavior observed by Azrin and Backofen (1970). For sufficiently high strain-rate sensitivity the strain bursts are suppressed.

2. Rate-dependent, non-associated flow theory

For non-associated flow, the plastic part of rate of deformation tensor in a rate-dependent theory can be expressed as

$$D_{ij}^{\mathrm{p}} = \dot{\phi}\frac{\partial G}{\partial \sigma_{ij}}, \tag{3}$$

where the effective plastic strain-rate $\dot{\phi}$ is defined as a function of effective stress $\sigma_{\mathrm{e}} = F\left(\sigma_{ij}\right)$ and the effective plastic strain, $\varepsilon_{\mathrm{e}}^{\mathrm{p}}$, i.e.

$$\dot{\phi} = \dot{\phi}\left(\sigma_{\mathrm{e}}, \varepsilon_{\mathrm{e}}^{\mathrm{p}}\right). \tag{4}$$

Generally, the functional form of $\dot{\phi}$ is highly non-linear in both σ_{e} and $\varepsilon_{\mathrm{e}}^{\mathrm{p}}$, leading to stiff differential equations. Therefore, (3) cannot be integrated effectively using an explicit scheme.

In order to investigate the effects of strain-rate sensitivity on SOW, we consider implicit integration of (3) over a time-interval δt. The average plastic part of rate of deformation tensor is approximated as

$$\left(D_{ij}^{\mathrm{p}}\right)_{\mathrm{ave}} = \dot{\phi}_{t+\delta t}\left(\frac{\partial G}{\partial \sigma_{ij}}\right)_{t+\delta t}. \tag{5}$$

From Taylor series expansions, $\dot{\phi}_{t+\delta t}$ is approximated as

$$\dot{\phi}_{t+\delta t} \simeq \frac{1}{1-(\partial\dot{\phi}/\partial\varepsilon_{\mathrm{e}}^{\mathrm{p}})_t\,\delta t}\left[\dot{\phi}_t + \left(\frac{\partial\dot{\phi}}{\partial\sigma_{\mathrm{e}}}\right)_t \delta\sigma_{\mathrm{e}}\right], \tag{6}$$

and $(\partial G/\partial\sigma_{ij})_{t+\delta t}$ is approximated as

$$\left(\frac{\partial G}{\partial\sigma_{ij}}\right)_{t+\delta t} \simeq \left(\frac{\partial G}{\partial\sigma_{ij}}\right)_t + \delta t\left(\frac{\partial^2 G}{\partial\sigma_{ij}\partial\sigma_{kl}}\right)_t\left(\overset{\nabla}{\sigma}_{kl}\right)_{\mathrm{ave}}, \tag{7}$$

where $(\overset{\nabla}{\sigma}_{kl})_{\mathrm{ave}}$ is the average Jaumann rate of Cauchy stress over the interval . With all terms depending on the total stress and effective plastic strain taken to be evaluated at time t, from here on the subscript *t* will be omitted. From (6) and (7) $\left(D_{ij}^{\mathrm{p}}\right)_{\mathrm{ave}}$ is

$$\left(D_{ij}^{\mathrm{p}}\right)_{\mathrm{ave}} \simeq \frac{\dot{\phi}_t}{1-\delta t\,\partial\dot{\phi}/\partial\varepsilon_{\mathrm{e}}^{\mathrm{p}}}\left[N_{ij}^{\mathrm{G}} + \delta t\frac{1}{\dot{\phi}_t}\frac{\partial\dot{\phi}}{\partial\sigma_{\mathrm{e}}}N_{ij}^{\mathrm{G}}\tilde{N}_{kl}^{\mathrm{F}}\left(\overset{\nabla}{\sigma}_{kl}\right)_{\mathrm{ave}} + \delta t\frac{\partial^2 G}{\partial\sigma_{ij}\partial\sigma_{kl}}\left(\overset{\nabla}{\sigma}_{kl}\right)_{\mathrm{ave}}\right], \tag{8}$$

where

$$N_{ij}^{\mathrm{G}} = \frac{\partial G}{\partial\sigma_{ij}}, \quad N_{ij}^{\mathrm{F}} = \frac{\partial F}{\partial\sigma_{ij}}, \quad \text{and} \quad \tilde{N}_{kl}^{\mathrm{F}} = \frac{\partial F}{\partial\sigma_{ij}} - \frac{\dot{\phi}_t}{G\left(\partial\dot{\phi}/\partial\sigma_{\mathrm{e}}\right)}\frac{\partial G}{\partial\sigma_{ij}}.$$

To estimate SOW for a finite time increment (and for the computations presented in the next two sections) a power-law form for $\dot{\phi}$ is adopted:

$$\dot{\phi} = \dot{\phi}_{\mathrm{o}} \left(\frac{\sigma_{\mathrm{e}}}{F_{\mathrm{cr}}(\varepsilon_{\mathrm{e}}^{\mathrm{p}})} \right)^{1/m}, \tag{9}$$

where $\dot{\phi}_{\mathrm{o}}$ is a material constant and m is the strain-rate sensitivity parameter, therefore

$$\left(\frac{\partial \dot{\phi}}{\partial \sigma_{\mathrm{e}}} \right)_{\mathrm{t}} = \frac{\dot{\phi}_{\mathrm{t}}}{m\sigma_{\mathrm{e}}} \text{ and } \left(\frac{\partial \dot{\phi}}{\partial \varepsilon_{\mathrm{e}}^{\mathrm{p}}} \right)_{\mathrm{t}} = -\frac{\dot{\phi}_{\mathrm{t}}}{mF_{\mathrm{cr}}} \frac{\partial F_{\mathrm{cr}}}{\partial \varepsilon_{\mathrm{e}}^{\mathrm{p}}}. \tag{10}$$

From (10) the constitutive equation for $\left(D_{ij}^{\mathrm{p}}\right)_{\mathrm{ave}}$ is

$$\left(D_{ij}^{\mathrm{p}}\right)_{\mathrm{ave}} \simeq \frac{\dot{\phi}_t}{1-\delta t\, \partial\dot{\phi}/\partial\varepsilon_{\mathrm{e}}^{\mathrm{p}}} N_{ij}^{\mathrm{G}} + \frac{\delta t\ \dot{\phi}_t}{\left(1-\delta t\, \partial\dot{\phi}/\partial\varepsilon_{\mathrm{e}}^{\mathrm{p}}\right) m\sigma_{\mathrm{e}}} \left[N_{ij}^{\mathrm{G}} \tilde{N}_{kl}^{\mathrm{F}} \left(\overset{\nabla}{\sigma}_{kl} \right)_{\mathrm{ave}} + m\sigma_{\mathrm{e}} \frac{\partial^2 G}{\partial\sigma_{ij}\partial\sigma_{kl}} \left(\overset{\nabla}{\sigma}_{kl} \right)_{\mathrm{ave}} \right] \tag{11}$$

For a convex flow potential the contribution to SOW from the third term in (11) is always positive. Therefore in rate-dependent theory, for a finite time increment and for a moderately large strain-rate sensitivity, that term tends to increase SOW.

3. Sheet necking analysis

A standard M-K analysis (Hutchinson and Neale, 1978) is used to estimate the forming limit strains for loadings ranging from uni-axial tension to equi-biaxial tension. As discussed above for small values of m, for e.g. $m = 0.0002$, SOW can be negative at small strains and instabilities can occur at strains, that are much smaller than the forming limit strains. Finite element analysis is used to study the nature of deformation fields in nearly rate-insensitive, non-associated flow, and somewhat surprisingly, jerky flow and strain bursts are seen.

The M-K analysis is conducted with conducted with rate-dependent theory presented in Sec. 2. In the analysis, the strain hardening function that enters the rate-dependent constitutive equations (10), is assumed to be of the form

$$F_{\mathrm{cr}}\left(\varepsilon_{\mathrm{e}}^{\mathrm{p}}\right) = k\left(\varepsilon_{\mathrm{e}}^{\mathrm{p}}\right)^{N}, \tag{12}$$

where N is the strain hardening exponent and k is the hardening constant. For the results presented below, we consider $N = 0.05$ and take $k = 595$ MPa, $\dot{\phi}_{\mathrm{o}} = 1\ \mathrm{s}^{-1}$, and $m = 0.02$. Isotropic hypo-elasticity is adopted, therefore the constitutive equation for D_{ij}^{e} is

$$D_{ij}^{\mathrm{e}} = \frac{1+\upsilon}{E} \overset{\nabla}{\sigma}_{ij} - \frac{\upsilon \overset{\nabla}{\sigma}_{kk}}{E} \delta_{ij}, \tag{13}$$

where E is the Young's Modulus and υ is the Poisson's ratio. We take $E = 200$ GPa and $\upsilon = 1/3$. In addition, the initial imperfection is taken to be $\xi = 0.01$.

Forming limit diagrams are plotted in Fig. 2 and the critical strain as a function of strain state in Fig. 3. The degree of non-associated flow can be parameterized in terms of the strength differential (*SD*), which is defined as

$$SD=\frac{2\left(\sigma_{\mathrm{T}}-\sigma_{\mathrm{C}}\right)}{\left(\sigma_{\mathrm{T}}+\sigma_{\mathrm{C}}\right)}=\frac{2\left[\left(1-2b/3\sqrt{3}\right)^{1/3}-\left(1+2b/3\sqrt{3}\right)^{1/3}\right]}{\left(1-2b/3\sqrt{3}\right)^{1/3}+\left(1+2b/3\sqrt{3}\right)^{1/3}}, \tag{14}$$

where σ_{C} is the initial yield stress in compression and σ_{T} is the initial yield stress in tension.

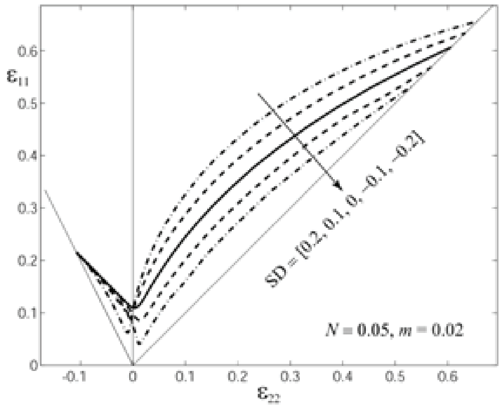

Fig. 2 Forming limits of sheet necking from M-K analysis for various SDs.

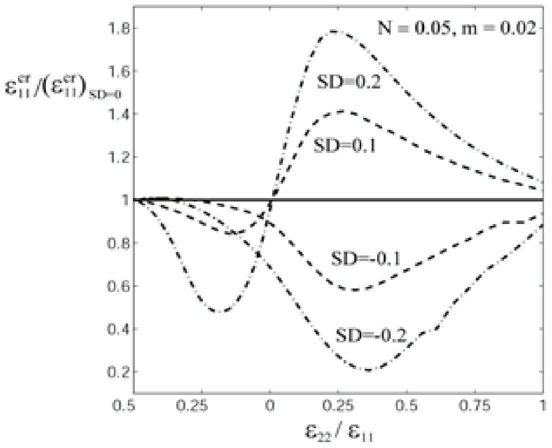

Fig. 3 Strength of non-associated flow effects on critical strains at failure

Next we consider a finite element analysis of the sheet necking problem; the configuration is shown schematically in Fig. 4. Loading near the plane strain state is considered with velocity boundary conditions imposed in the ratio $v_2/v_1=-0.04$. The analysis is done using implicit dynamics scheme in ABAQUS. For the results presented below, the non-associated flow parameter $b=-0.7$, which corresponds to SD=0.2; the hardening exponent $N=0.1$, the material density $\rho=7.8\text{E-}9$, and, unless otherwise specified, all other material constants are the same as in the M-K analysis. The geometric parameters are: $\xi=0.05$ (initial inhomogeneity), $L=45$ mm, $W=9$ mm, and $H=0.75$ mm.

The evolution of effective plastic strain for several strain-rate sensitivities is shown in Fig. 5 for both associated and non-associated flow – the overbar denotes an average over the corresponding region. For a moderately large strain-rate sensitivity, e.g. $m=0.01$, the behavior is smooth for both associated and non-associated flow. For non-associated flow and relatively small strain-rate sensitivity, e.g. $m=0.002$ and $m=0.0002$ (which corresponds to nearly rate independent behavior), the deformation is jerky as a result of strain bursts. During periods of bursts, when the strain in the band increases rapidly, the overall load also drops precipitously. This occurs do to very small or negative values of SOW. At the same time, the stress state in the band tends to rotate and lead to an increase in SOW which, as it becomes positive, tends to stabilize the deformation in the band. Several bursts occur before the deformation becomes unstable at the forming limit. In this case of $b=-0.7$ (SD=0.2), the forming limit strain is reduced by more than a half due to non-associated flow effects.

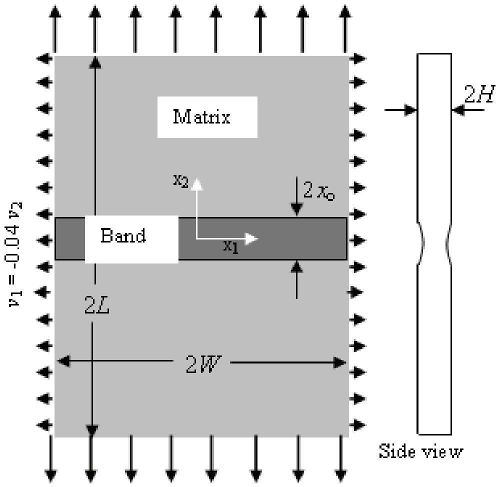

Fig. 4. Loading configuration in ABAQUS finite element implementation

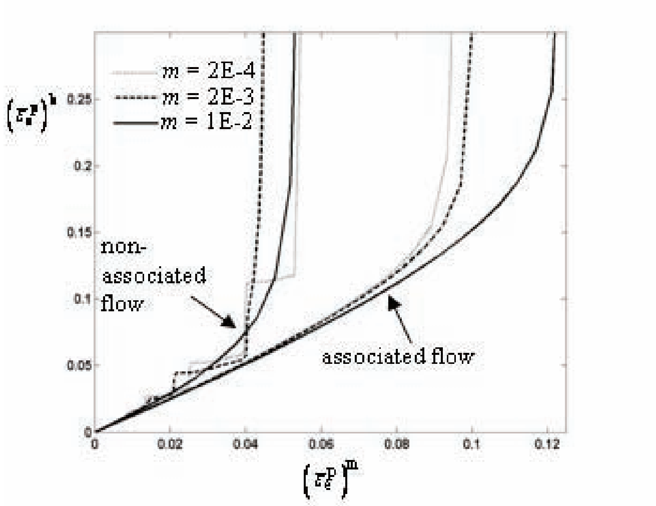

Fig. 5 Effect of strain-rate sensitivity on the evolution of the neck with associated and non-associated flow

4. Conclusions

The stress-state dependence of the Peierls barrier for the motion of a screw dislocation in non-close-packed crystalline lattices violates Schmid's law, and its effect persists in multiple slip in single crystals and leads to non-associated flow behavior for polycrystalline aggregates. Plasticity models based upon distinct yield and flow functions are proposed to describe such behavior and specialized to case of isotropic response. For non-associated flow behavior, second-order work can be negative even for positive hardening moduli, and that can strongly affect the deformation behavior. Studies of sheet necking using both a M-K analysis and by finite elements predict that non-associated flow has a significant effect on the evolution of inhomogenieties in the sheet. For nearly rate-insensitive response, intermittent bursts of strain arise for non-associated flow behavior, particularly for deformations near the plane strain state. Moderately large strain-rate sensitivities are shown to suppress the instabilities.

5. Acknowledgements

This research was supported by the NSF Grant no. DMR 02-19243 and by DOE/ASCI through Lawrence Livermore National Laboratory.

6. References

[1] Azrin M, Backofen W A 1970. The deformation and failure of a bi-axially stretched sheet. Metallurgical Transactions
[2] Bassani J L, 1994. Plastic-flow of crystals. Advances in Applied Mechanics 30, 191-258.
[3] Bassani J L, 2001. Incompatibility and a simple gradient theory of plasticity. Journal of Mechanics and Physics of Solids 49, 1983-1996.

[4] Bassani J L, Ito K, Vitek V, 2001. Complex macroscopic plastic flow arising from non-planar dislocation core structures. Material Science and Engineering A 319-321, 97-101.

[5] Groger R, Vitek V, 2005. Breakdown of the Schmid law in bcc molybdenum related to the effect of shear stress perpendicular to the slip direction. Materials science Forum 482, 123-126.

[6] Hutchinson J W, Neale K W, 1978. Mechanics of Sheet Metal Forming, Plenum Publishing Corporation, N. Y., 127-153.

[7] Li M, Drucker D C 1994. Instability and bifurcation of a Nonassociated extended mises model in the hardening regime. Journal of Mechanics and Physics of Solids 42 (12), 1883-1904.

[8] Qin Q, Bassani J L, 1992. Non-Schmid yield behavior in single-crystals. Journal of Mechanics and Physics of Solids 40 (4), 813-833.

[9] Qin Q, Bassani J L, 1992. Non-associated plastic-flow in single crystals. Journal of Mechanics and Physics of Solids 40 (4), 835-862.

[10] Racherla V, Bassani J L, 2006. Non-associated flow theories of plasticity with emphasis on uniqueness and stability of solutions to incremental boundary value problems. (to be submitted)

[11] Raniecki B 1979. Uniqueness criteria in solids with non-associated plastic-flow laws at finite deformations. Bulletin De L Academie Polonaise Des Sciences-Serie Des Sciences Techniques 27 (8-9), 721-729.

[12] Vitek V, Mrovec M, Bassani J L, 2004. Influence of non-glide stresses on plastic flow: from atomistic to continuum modeling. Material Science and Engineering A 265, 31-37.

[13] Vitek, V., Pope, D. P., and Bassani, J. L., 1996. Anomalous yield behaviour of compounds with $L1_2$ structure, in *Dislocations in Solids*, F. R. N. Nabarro and M. S. Duesbery, eds., pp. 136-185 Elsevier Science.

FIRE: Fast Inertial Relaxation Engine for structural optimisations on all scales

Erik Bitzek[1], *Pekka Koskinen*[2,3], *Peter Gumbsch*[2,1], *Michael Moseler*[3,2]

[1]*Institut fuer Zuverlaessigkeit von Bauteilen und Systemen, Universitaet Karlsruhe (TH), Kaiserstrasse12, 76131 Karlsruhe, Germany*

[2]*Fraunhofer-Institut für Werkstoffmechanik IWM, Wöhlerstr. 11, 79108 Freiburg, Germany*

[3]*Faculty of Physics, University of Freiburg, Hermann-Herder-Str. 3, 79104 Freiburg, Germany*

We introduce a simple structural optimization algorithm which is significantly faster than standard implementations of the conjugated gradient method and which is competitive with more sophisticated quasi-Newton schemes typically used in ab initio calculations. It is based on conventional Newtonian dynamics with additional velocity modifications and adaptive time steps. The efficiency, robustness and versatility of the method is illustrated using a variety of test cases, including typical systems encountered in nanoscience, solid state physics, materials research and biochemistry. The examples range from electronic structure calculations of bio molecules and nanotubes, via large scale molecular dynamics of complex alloys, cracks and thin films to the continuum mechanics of nanocomposits. Despite its simplicity FIRE performs amazingly fast on all scales. It can even be applied to the efficient minimisation of objective functions in other scientific branches like the sum of least squares in statistical modelling or fitness functions in evolutionary theories.

Gamma-convergence methods for multi-scale modeling

Andrea Braides[1], *Lev Truskinovsky*[2]

[1] *Universita' di Roma „Tor Vergata", Dipartimento di Matematica, via della ricerca scientifica 1, 00133 Roma, Italy*
[2] *Laboratory of Solid Mechanics, École Polytechnique, Palaiseau, Paris, France*

The use of Gamma-convergence in the description of the asymptotic behaviour of systems with small parameters (homogenization of composites, phase transitions, discrete-to-continuum theories, thin structures, etc.) is a common practice in multi-scale variational analysis. Unfortunately, the limit `theories' resulting from such an approach are simplistic, or inaccurate in some regimes, or simply different from those commonly used by practitioners.

We propose a new use of the methods of Gamma-convergence, whose aim is to pinpoint singular regimes, and possibly provide alternative limit theories other than those given by the Gamma-limit.

First-passage Monte Carlo

Vasily Bulatov[1], T. Oppelstrup[1], M.H. Kalos[1], B. Sadigh[1], G.H Gilmer[1]

[1]Lawrence Livermore National Laboratory, University of California, L-367, 94551 Livermore, USA

We unveil a principally new Monte Carlo algorithm for simulations of multiple diffusing particles of finite dimensions that coallesce or annihilate on collisions. The algorithm is derived from the theory of first-passage processes and a time-dependent Green's function formalism. The new method circumvents the need for long and tedious diffusion hops by which the particles find each other in space. At the same time, the algorithm is exact and its computational efficiency is astonishing. The new algorithm is generally applicable in 1d, 2d, 3d, ... and to a wide variety of important physical situtations, including nucleation, growth and coarsening of alloy particles and interstitial and vacancy clusters after quench or under irradiation. We will present simulation of multi-million particle ensembles covering over 10 decades of time of microstructural evolution.

Dislocations In Cubic Crystals Described By Discrete Models

Ana Carpio[1], Luis L. Bonilla[2], I. Plans[2]

[1]**Departamento de Matemática Aplicada, Universidad Complutense**
28040 Madrid, Spain, ana_carpio@mat.ucm.es;
[2]**Departamento de Materiales, Universidad Carlos III, 28911 Leganés**
Spain, bonilla@ing.uc3m.es, ignacio.plans@uc3m.es.

ABSTRACT

Discrete equations of motion for dislocations in cubic crystals including dissipation and fluctuations are derived. These models have the standard linear anisotropic elasticity as their continuum limit and their main ingredients are the elastic stiffness constants of the material and a dimensionless periodic function that restores the translation invariance of the crystal and influences the dislocation size. Static and moving dislocations are identified with wave solutions of the model.

1. Introduction

Understanding mechanical, optical and electronic properties of materials requires a better understanding of the relation between defects and observed macroscopic behavior. The atomic scale can be resolved by *ab initio* or molecular dynamics simulations, which are very costly at the present time. Thus, it is interesting to have systematic models of defect motion in crystals that can be solved cheaply, are compatible with elasticity and yield useful information about the defect cores and their mobility.

In a previous paper, we have proposed a discrete model of dislocations and their motion in cubic crystals with a one atom basis [1]. Let us consider a simple cubic crystal. Firstly, we discretize space along the primitive vectors defining the unit cell of the crystal $\mathbf{x} \equiv (x, y, z) = (l, m, n)a$, in which a is the length of the primitive cubic cell, and l, m and n are integer numbers. Secondly, we replace the gradient of the displacement vector $\tilde{u}_i(x, y, z, t) = a\, u_i(l, m, n; t)$ ($u_i(l, m, n; t)$ is a nondimensional vector) in the strain energy density by an appropriate periodic function of the discrete gradient, $g(D_j^+ u_i)$: We shall define the *discrete* distortion tensor as

$$w_i^{(j)} = g(D_j^+ u_i), \tag{1}$$

$$D_1^{\pm} u_i(l, m, n; t) = \pm\, [u_i(l \pm 1, m, n; t) - u_i(l, m, n; t)], \tag{2}$$

etc., where $g(x)$ is a periodic function of period one satisfying $g(x) \sim x$ as $x \to 0$. The strain energy density for the discrete model is obtained by substituting the strain tensor in the usual strain energy density:

$$W = \frac{1}{2} c_{ijkl} e_{ij} e_{kl}, \tag{3}$$

$$c_{ijkl} = C_{12}\, \delta_{ij}\delta_{kl} + \frac{C_{11} - C_{12}}{2}\, (\delta_{ik}\delta_{jl} + \delta_{il}\delta_{jk})$$

$$+H\left(\frac{\delta_{ik}\delta_{jl}+\delta_{il}\delta_{jk}}{2}-\delta_{1i}\delta_{1j}\delta_{1k}\delta_{1l}-\delta_{2i}\delta_{2j}\delta_{2k}\delta_{2l}-\delta_{3i}\delta_{3j}\delta_{3k}\delta_{3l}\right), \tag{4}$$

$$H = 2C_{44}+C_{12}-C_{11}, \tag{5}$$

$$e_{ij} = \frac{1}{2}\,(w_i^{(j)}+w_j^{(i)}) = \frac{g(D_j^+u_i)+g(D_i^+u_j)}{2} \tag{6}$$

(sum over repeated indices is assumed), where c_{ijkl} are the elastic constants of the crystal. Summing over all lattice sites, we obtain the potential energy of the crystal:

$$V(\{u_i\}) = a^3\sum_{l,m,n} W(l,m,n;t), \tag{7}$$

in which we have considered the strain energy deensity to be a function of the point $W(\mathbf{u}) = W(l,m,n;t)$, $(l,m,n) = (x,y,z)/a$. Next, we find the equations of motion by the usual methods of classical mechanics. For conservative dynamics:

$$\rho a^4\,\ddot{u}_i(l,m,n;t) = -\frac{1}{a}\,\frac{\partial V(\{u_k\})}{\partial u_i(l,m,n;t)}, \tag{8}$$

or, equivalently [1],

$$\rho a^2\,\ddot{u}_i = \sum_{j,k,l} D_j^-[c_{ijkl}\,g'(D_j^+u_i)\,g(D_l^+u_k)]. \tag{9}$$

Here $\ddot{u}_i \equiv \partial^2 u_i/\partial t^2$ and the displacement vector is dimensionless, so that both sides of Eq. (9) have units of force per unit area. Let us now restore dimensional units to Equation (9), so that $\tilde{u}_i(x,y,z) = a\,u_i(x/a,y/a,z/a)$, then let $a\to 0$, use Eq. (9) and that $g(x)\sim x$ as $x\to 0$. Then we obtain the usual Cauchy equations of linear elasticity:

$$\rho\,\frac{\partial^2\tilde{u}_i}{\partial t^2} \;=\; \sum_{j,k,l}\frac{\partial}{\partial x_j}\left(c_{ijkl}\,\frac{\partial\tilde{u}_k}{\partial x_l}\right), \tag{10}$$

provided the components of the distortion tensor are very small. Far from the core of a defect, the discrete gradient approaches the continuous one. Then, provided the slope $g'(0)$ is one in the appropriate units, the spatially discrete equations of motion become those of the anisotropic elasticity. The periodic function $g(x)$ ensures that sliding a plane of atoms an integer number of times the lattice distance a parallel to a primitive direction does not change the potential energy of the crystal.

Once the discrete model is specified, different dislocation configurations can be selected by requiring that their far field should adopt the well-known form of continuous elasticity [1,2]. Static dislocations move when the applied force surpasses a critical threshold. The magnitude of this threshold is controlled by the size of the regions where g' becomes negative: it decreases as their size increase. This information allows to fit g for particular materials. A possible choice is:

$$g(x) = \begin{cases} x, & |x| < \frac{1}{2}-\alpha, \\ \frac{(1-2\alpha)(1-2x)}{4\alpha}, & \frac{1}{2}-\alpha < x < \frac{1}{2}+\alpha, \end{cases} \tag{11}$$

which is periodically extended outside the interval $(\alpha-1/2,\alpha+1/2)$ for a given $\alpha\in(0,1/2)$. To select α, we calculate numerically the Peierls stress needed to move a given dislocation as a function of α and fit it to data from experiments or molecular dynamics calculations.

In all cases, the procedure to obtain numerically the dislocation from the discrete model is the same. We first solve the stationary equations of elasticity with appropriate singular source terms to obtain the *dimensional* displacement vector $\tilde{\mathbf{u}}(x,y,z) = (\tilde{u}_1(x,y,z), \tilde{u}_2(x,y,z), \tilde{u}_3(x,y,z))$ of the static dislocation *under zero applied stress.* This displacement vector yields the far field of the corresponding dislocation for the discrete model, which is the *nondimensional* displacement vector:

$$\mathbf{U}(l,m,n) = \frac{\tilde{\mathbf{u}}\left((l+\delta_1)a, (m+\delta_2)a, (n+\delta_3)a\right)}{a}. \tag{12}$$

Here $0 \le \delta_i < 1$, $i = 1,2,3$, are chosen so that the singularity at $x = y = z = 0$ does not coincide with a lattice point. For a sc crystal, it is often convenient to select the center of a unit cell, $\delta_i = 1/2$. We use the nondimensional static displacement vector $\mathbf{U}(l,m,n)$ defined by (12) in the boundary and initial conditions for the discrete equations of motion.

Take for example, a pure screw dislocation along the z axis with Burgers vector $\mathbf{b} = (0,0,\mathrm{b})$ has a displacement vector $\tilde{\mathbf{u}} = (0,0,\tilde{u}_3(x,y))$ with $\tilde{u}_3(x,y) = \mathrm{b}\,(2\pi)^{-1}\tan^{-1}(y/x)$ [2]. The discrete equation for the z component of the *nondimensional* displacement $u_3(l,m;t)$ is:

$$\rho a^2\, \ddot{u}_3 \;=\; C_{44}\,\{D_1^-[g(D_1^+u_3)\,g'(D_1^+u_3)] + D_2^-[g(D_2^+u_3)\,g'(D_2^+u_3)]\}. \tag{13}$$

To find the static solution of this equation corresponding to a screw dislocation, we could minimize an energy functional. However, it is more efficient to solve the following overdamped equation:

$$\beta\,\dot{u}_3 \;=\; C_{44}\,\{D_1^-[g(D_1^+u_3)\,g'(D_1^+u_3)] + D_2^-[g(D_2^+u_3)\,g'(D_2^+u_3)]\}. \tag{14}$$

The stationary solutions of Eqs. (13) and (14) are the same, but the solutions of (14) relax rapidly to the stationary solutions if we choose appropriately the damping coefficient β. We solve Eq. (14) with initial condition $u_3(l,m;0) = U_3(l,m) \equiv \mathrm{b}\,(2\pi a)^{-1}\tan^{-1}[(m+1/2)/(l+1/2)]$ (corresponding to $\delta_i = 1/2$), and with boundary conditions $u_3(l,m;t) = U_3(l,m) + F\,m$ at the upper and lower boundaries of our lattice. At the lateral boundaries, we use zero-flux Neumann boundary conditions. Here F is an applied dimensionless stress (the dimensional stress is $C_{44}F$). For small stresses, the solution of Eq. (14) relaxes to a static screw dislocation $u_3(l,m)$ with the desired far field. A static screw dislocation moves if the applied shear stress surpasses the static Peierls stress, F_{cs}. A moving dislocation continues doing so until the applied shear stress falls below a lower threshold F_{cd} (dynamic Peierls stress); see [3] for a similar situation for edge dislocations. The numerical solution shows that moving a dislocation requires that we should have $g'(D_j^+u_3) < 0$ (with either $j = 1$ or 2) at its core [3], which is harder to achieve as α decreases. A discusion of the changes in the size of the dislocation core and the Peierls stress due to α can be found in [1]. Using the same technique, stationary planar edge dislocations for an isotropic sc material have been constructed and a variety of dipole and loops of edge dislocations have been numerically found [1].

In this paper, we explain how to treat dissipative dynamics and the effect of fluctuations.

2. Dissipative equations of motion

Overdamped dynamics obtained by replacing the time differential of the displacement vector instead of the inertial term in the equation of motion (9) is not too realistic.

Instead, we can add dissipation to the equations of motion by considering a quadratic dissipative function with cubic symmetry. The resulting equations are:

$$\rho a^2\,\ddot{u}_i \;=\; \sum_j D_j^-[(\sigma_{ij}+\Sigma_{ij})\,g'(D_j^+u_i)]. \tag{15}$$

Here $\sigma_{ij}=c_{ijkl}e_{kl}=c_{ijkl}g(D_l^+u_k)$ is the elastic part of the stress tensor, and

$$\begin{aligned}\Sigma_{ij} &= \eta_{ijkl}\dot{e}_{kl}, &(16)\\ \eta_{ijkl} &= \left(\zeta-\frac{2}{3}\eta\right)\delta_{ij}\delta_{kl}+\eta\,(\delta_{ik}\delta_{jl}+\delta_{il}\delta_{jk})\\ &+\;\gamma\left(\frac{\delta_{ik}\delta_{jl}+\delta_{il}\delta_{jk}}{2}-\delta_{1i}\delta_{1j}\delta_{1k}\delta_{1l}-\delta_{2i}\delta_{2j}\delta_{2k}\delta_{2l}-\delta_{3i}\delta_{3j}\delta_{3k}\delta_{3l}\right), &(17)\end{aligned}$$

is the viscous part. In the cubic case, the viscosity tensor η_{iklm} is determined by the three scalar quantities ζ, η and γ. For isotropic sc crystals, $C_{11}=\lambda+2\mu$, $C_{12}=\lambda$, $C_{44}=\mu$, $\gamma=0$. In the isotropic case and taking the continuum limit $a\to 0$, Eqs. (15) to (17) yield the viscous Navier's equations for isotropic elasticity [4]:

$$\rho\,\frac{\partial^2\tilde{\mathbf{u}}}{\partial t^2}=\mu\,\Delta\tilde{\mathbf{u}}+(\lambda+\mu)\,\nabla(\nabla\cdot\tilde{\mathbf{u}})+\eta\,\Delta\frac{\partial\tilde{\mathbf{u}}}{\partial t}+\left(\zeta+\frac{\eta}{3}\right)\,\nabla\left(\nabla\cdot\frac{\partial\tilde{\mathbf{u}}}{\partial t}\right). \tag{18}$$

3. Discrete model including dissipation and fluctuations

To consider dissipation and fluctuations of the stress tensor and of the heat flux in the equation for the temperature we follow Onsager's ideas as used in Fluctuating Hydrodynamics [5] and obtain the equations of motion:

$$\begin{aligned}&\rho a^2\,\ddot{u}_i=\sum_j D_j^-[(\sigma_{ij}+\Sigma_{ij}+s_{ij})\,g'(D_j^+u_i)], &(19)\\ &\langle s_{ij}\rangle=0,\\ &\langle s_{ij}(l,m,n;t)s_{ab}(l',m',n';t')\rangle=k_BT\frac{\eta_{ijab}+\eta_{abij}}{a^3}\delta_{ll'}\delta_{mm'}\delta_{nn'}\,\delta(t-t'), &(20)\end{aligned}$$

[with $\sigma_{ij}=\sum_{k,l}c_{ijkl}g(D_l^+u_k)-\alpha_{ij}(T-T_0)$] for the displacement vector, and

$$\begin{aligned}&\rho ac\dot{T}+a\,T\sum_{i,j}\alpha_{ij}g'(D_j^+u_i)\,D_j^+\dot{u}_i=-\sum_i D_i^-(Q_i+\xi_i), &(21)\\ &\langle\xi_i\rangle=0,\\ &\langle\xi_i(l,m,n;t)\xi_j(l',m',n';t')\rangle=k_BT^2\,\frac{\kappa_{ij}+\kappa_{ji}}{a^3}\,\delta_{ll'}\delta_{mm'}\delta_{nn'}\,\delta(t-t'), &(22)\end{aligned}$$

for the local temperature $T(l,m,n)$. In Eq. (21), c is the specific heat of the solid, and the heat flux Q_i is related to the discrete gradient of the temperature by the constitutive relation $Q_i=-\sum_j\kappa_{ij}D_j^+T/a$, where κ_{ij} is the thermal conductivity tensor. k_B is the Boltzmann constant and the temperature is measured in Kelvin. The correlations of the fluctuating stress tensor and the fluctuating heat flux contain the viscosity tensor and the thermal conductivity tensor, respectively. In crystals with cubic symmetry, the elastic constants and the viscosity tensor are given by Eqs. (4) and (17), respectively. The thermal conductivity and thermal expansion tensors are isotropic, $\kappa_{ij}=\kappa\delta_{ij}$, $\alpha_{ij}=\alpha\delta_{ij}$. Note that the correlations of s_{ij} in (20) and of ξ_i in (22) are proportional to $1/a^3$, which becomes $\delta(\mathbf{x}-\mathbf{x}')$ in the continuum limit as $a\to 0$.

4. Extensions to fcc and bcc crystals

Let us explain how to extend our discrete models of dislocations to fcc or bcc crystal symmetry, assuming that we have one atom per lattice site. For fcc or bcc crystals, the primitive vectors of the unit cell are not orthogonal. To find a discrete model for these crystals, we should start by writing the strain energy density in a non-orthogonal vector basis, a_1, a_2, a_3, instead of the usual orthonormal vector basis e_1, e_2, e_3 determined by the cube sides. Let x_i denote coordinates in the basis e_i, and let x'_i denote coordinates in the basis a_i. Notice that the x_i have dimensions of length while the x'_i are dimensionless. The matrix $\mathcal{T} = (a_1, a_2, a_3)$ whose columns are the coordinates of the new basis vectors in terms of the old orthonormal basis can be used to change coordinates as follows:

$$x'_i = \mathcal{T}^{-1}_{ij} x_j, \; x_i = \mathcal{T}_{ij} x'_j. \tag{23}$$

Similarly, the displacement vectors in both basis are related by

$$u'_i = \mathcal{T}^{-1}_{ij} \tilde{u}_j, \; \tilde{u}_i = \mathcal{T}_{ij} u'_j, \tag{24}$$

and partial derivatives obey

$$\frac{\partial}{\partial x'_i} = \mathcal{T}_{ji} \frac{\partial}{\partial x_j}, \; \frac{\partial}{\partial x_i} = \mathcal{T}^{-1}_{ji} \frac{\partial}{\partial x'_j}. \tag{25}$$

Note that u'_i and x'_i are nondimensional while $\tilde{u}_i$ and x_i have dimensions of length. By using these equations, the strain energy density $W = (1/2) c_{iklm} e_{ik} e_{lm}$ can be written as

$$W = \frac{1}{2}\, c_{ijlm} \frac{\partial \tilde{u}_i}{\partial x_j} \frac{\partial \tilde{u}_l}{\partial x_m} = \frac{1}{2}\, c'_{rspq} \frac{\partial u'_r}{\partial x'_s} \frac{\partial u'_p}{\partial x'_q}, \tag{26}$$

where the new elastic constants are:

$$c'_{rspq} = c_{ijlm} \mathcal{T}_{ir} \mathcal{T}^{-1}_{sj} \mathcal{T}_{lp} \mathcal{T}^{-1}_{qm}. \tag{27}$$

Notice that the elastic constants have the same dimensions in both the orthogonal and the non-orthogonal basis. To obtain a discrete model, we shall consider that the dimensionless displacement vector u'_i depends on dimensionless coordinates x'_i that are integer numbers $u'_i = u'_i(l, m, n; t)$. As in the simple cubic case, we replace the distortion tensor (gradient of the displacement vector in the non-orthogonal basis) by a periodic function of the corresponding forward difference, $w^{(j)}_i = g(D^+_j u'_i)$. As in Eq. (11), g is a periodic function with $g'(0) = 1$ and period 1. The discretized strain energy density is

$$W(l, m, n; t) = \frac{1}{2}\, c'_{rspq} g(D^+_s u'_r)\, g(D^+_q u'_p). \tag{28}$$

The elastic constants c'_{rspq} in (27) can be calculated in terms of the Voigt stiffness constants for a cubic crystal, C_{11}, C_{44} and C_{12}, which determine the tensor of elastic constants (4). The elastic energy can be obtained from Eq. (28) for W by means of Eqs. (7). Then the conservative equations of motion (8) are

$$\rho a^3 \frac{\partial^2 u'_i}{\partial t^2} = -\mathcal{T}^{-1}_{iq} \mathcal{T}^{-1}_{pq} \frac{\partial V}{\partial u'_p},$$

which, together with Eqs. (7) and (28), yield

$$\rho \frac{\partial^2 u_i'}{\partial t^2} = \mathcal{T}_{iq}^{-1}\mathcal{T}_{pq}^{-1}\, D_j^-[g'(D_j^+ u_p')\, c'_{pjrs}\, g(D_s^+ u_r')]. \tag{29}$$

This equation becomes (9) for orthogonal coordinates, $\mathcal{T}_{iq}^{-1} = \delta_{iq}/a$.

To add dissipation and fluctuations to these equations, we need to replace $c'_{pjrs} g(D_s^+ u_r')$ by $c'_{pjrs} g(D_s^+ u_r') - \alpha'_{pj}(T - T_0) + \eta'_{pjrs} g'(D_s^+ u_r')\, D_s^+ \dot{u}_r' + s'_{pj}$, in which η'_{pjrs} is related to the viscosity tensor (17) in the same way as c'_{pjrs} is related to c_{ijlm} by (27). The random stress tensor s'_{pj} has zero mean and correlation given by (20) with the modified viscosity tensor η'_{ijab} instead of the viscosity tensor (17). The heat conduction equations are

$$\rho c \frac{\partial T}{\partial t} + T\, \alpha'_{ij} g'(D_j^+ u_i')\, D_j^+ \frac{\partial u_i'}{\partial t} = D_i^- \left(\kappa'_{ij} D_j^+ T + \frac{\xi_i'}{a} \right), \tag{30}$$

$$\langle \xi_i' \rangle = 0,$$

$$\langle \xi_i'(l,m,n;t)\xi_j'(l',m',n';t') \rangle = k_B T^2\, \frac{\kappa'_{ij} + \kappa'_{ji}}{a}\, \delta_{ll'}\delta_{mm'}\delta_{nn'}\, \delta(t - t'), \tag{31}$$

$$\kappa'_{pq} = \mathcal{T}_{pi}^{-1}\mathcal{T}_{qj}^{-1}\kappa_{ij}, \quad \alpha'_{pq} = \frac{1}{2}\left(\mathcal{T}_{ip}\mathcal{T}_{qj}^{-1} + \mathcal{T}_{jp}\mathcal{T}_{qi}^{-1}\right)\alpha_{ij}. \tag{32}$$

Note that the both the original and the modified tensors α_{ij} and κ_{ij} are symmetric.

Once we have derived the equations of motion, stationary dislocations can be calculated by first finding the corresponding solution to the equations of anisotropic elasticity and using it to set up initial and boundary conditions for overdamped equations of motion. For fcc and bcc crystals, screw and edge dislocations have been constructed in [1].

5. Conclusions

We have proposed discrete models describing defects in crystal structures whose continuum limit is the standard linear anisotropic elasticity, including fluctuations according to the fluctuation-dissipation theorem. The main ingredients entering the models are the elastic stiffness constants of the material and a dimensionless periodic function that restores the translation invariance of the crystal (and together with the elastic constants determines the dislocation size). For simple cubic crystals, their equations of motion with conservative or damped dynamics are derived. For fcc and bcc metals, the primitive vectors along which the crystal is translationally invariant are not orthogonal. Similar discrete models and equations of motion are found by writing the strain energy density and the equations of motion in non-orthogonal coordinates. These models to investigate dislocation motion and interaction in simple geometries.

Acknowledgements

This work has been supported by the Spanish MEC Grant MAT2005-05730-C02.

References

[1] Carpio, A., Bonilla, L.L., 2005, Discrete models for dislocations and their motion in cubic crystals, Phys. Rev. B **71**, 134105.

[2] Hirth, J.P., Lothe, J., 1982. Theory of Dislocations. John Wiley & Sons, New York.

[3] Carpio, A., Bonilla, L.L., 2003. Edge dislocations in crystal structures considered as traveling waves of discrete models. Phys. Rev. Lett. **90**, 135502.

[4] Landau, L.D., Lifshitz, E.M., 1986. Theory of elasticity. Pergamon Press, London.

[5] Landau, L.D., Lifshitz, E.M., 1959. Fluid Mechanics, Pergamon Press, London.

Relaxation of single-slip single-crystal plasticity with linear hardening

Sergio Conti

**Fachbereich Mathematik, Universität Duisburg-Essen
Lotharstr. 65, 47057 Duisburg, Germany**

ABSTRACT

We consider a model for single-crystal plasticity with a single active slip system and linear hardening, with geometrically nonlinear but rigid elasticity. We determine the relaxation of the incremental variational problem, i.e., the quasiconvex envelope of the appropriate energy density. We show that fine-scale structures are spontaneously formed, in the form of laminates between regions with slip in opposite directions.

1. Introduction

Plastic deformation of single crystals leads to the spontaneous formation of microstructures, which largely influence the macroscopic material response. The work by Ortiz and Repetto [1] started a large effort to understand plastic microstructure formation in a variational setting. This formulation is admissible if one assumes monotonicity, leading to the so-called *deformation theory of plasticity*; or more in general for short times (in the sense of an incremental problem). Minimizing out the internal variables one obtains a variational problem of the form

$$\int_\Omega W(\nabla u)dx \text{ plus external forces, boundary conditions etc.}.$$

The discrete nature of crystalline slip systems makes the energy density W not convex, which in turn favors the spontaneous formation of microstructures. In practice, one is often interested in the macroscopic material behavior, on length scales much larger than that of the microstructure. It is therefore convenient to adopt a scale separation, solving locally (ideally, at each material point for the macroscopic computation) a microscopic, scale-invariant problem. The theory of relaxation shows that the macroscopic material behavior can be studied directly by replacing W with its quasiconvex envelope, which under suitable assumptions takes the form [2, 3, 4]

$$W^{\mathrm{qc}}(F) = \inf \left\{ \int_{(0,1)^n} W(F + \nabla\varphi)dx : \varphi \in W_0^{1,\infty}((0,1)^n;\mathbb{R}^n) \right\}.$$

This definition corresponds to optimizing locally (i.e., at any material point) over all possible microstructures, which are here described by all possible Lipschitz continuous functions φ which vanish on the boundary. In a geometrically linear setting, quasiconvexity often reduces to the much simpler concept of convexity. For example, for a model of crystal plasticity without hardening the quasiconvex envelope W^{qc} turns out to be convex [5].

In a finite-deformation context however convexity contrasts with invariance under rotations. Whereas abstract theory shows that quasiconvexity is the appropriate concept, in practice this turns out to be much more difficult to handle. Ortiz and Repetto have shown that energy densities describing a system with a single slip system in finite deformation lack quasiconvexity, and therefore lead to spontaneous microstructure formation in the form of laminates, a fact known as geometric softening [1]. A two-dimensional energy density with linear hardening and with a polyconvex elastic part was proposed and shown also to lack quasiconvexity in [6]. There is up to now only one model problem in finite plasticity for which the quasiconvex envelope W^{qc} could be computed explicitly, namely, the model with a single slip system and without hardening considered in [7] and presented in (2) below. Interest has also been devoted to numerical approximations; in particular, in [8] the two-dimensional model with a single slip system from [6] was studied numerically. An approximate numerical relaxation for the same model was then integrated in a macroscopic finite-element computation in [9]. A finer analysis of the quasiconvex envelope of the same energy density is now under way, preliminary results are presented in [10, 11].

We consider here the rigid-elasticity limiting case of the model considered in [8, 9] for small critical stress. The resulting energy densityresulting $W : \mathbb{R}^{2\times 2} \to [0, \infty]$ has the form

$$W(F) = \begin{cases} \gamma^2 & \text{if } F = Q(\mathrm{Id} + \gamma s \otimes m) \quad \text{for some } Q \in SO(2),\ \gamma \in \mathbb{R} \\ \infty & \text{else.} \end{cases} \tag{1}$$

Here s, m are a pair of orthonormal vectors in $\mathbb{R}^2$, representing the slip direction and the slip-plane normal, and γ is the slip. For comparison, the problem considered in [7] is

$$W_{\mathrm{CT}}(F) = \begin{cases} |\gamma| & \text{if } F = Q(\mathrm{Id} + \gamma s \otimes m) \quad \text{for some } Q \in SO(2),\ \gamma \in \mathbb{R} \\ \infty & \text{else.} \end{cases} \tag{2}$$

We determine here the full relaxation of (1), by extending the method developed in [7]. We obtain a characterization of the optimal microstructures which compares favorably with the previous numerical results from [8, 9]. This result had been announced in [12] and has been used in [10, 11] as a basis to develop an efficient numerical relaxation algorithm.

2. Main result

Theorem 1. *The quasiconvex, rank-one convex, and polyconvex envelopes of the energy W defined in (1) are equal and given by*

$$W^{\mathrm{qc}}(F) = \begin{cases} |Fm|^2 - 1 & \textit{if } \det F = 1 \textit{ and } |Fs| \le 1\,, \\ \infty & \textit{else.} \end{cases} \tag{3}$$

The optimal energy is realized by a first-order laminate, which is supported on two matrices which have plastic deformation γ of the same magnitude and opposite sign.

We recall that a function $W : \mathbb{R}^{2\times 2} \to \mathbb{R} \cup \{\infty\}$ is rank-one convex if it is convex along rank-one lines, i.e., if $W(F + ta \otimes n)$ is convex in t for any fixed F, a, n. A function $W : \mathbb{R}^{2\times 2} \to \mathbb{R} \cup \{\infty\}$ is polyconvex if it can be written as a convex function of F and $\det F$, i.e., if $W(F) = g(F, \det F)$ for some convex $g : \mathbb{R}^5 \to \mathbb{R} \cup \{\infty\}$. The rank-one (quasi-, poly-) convex envelope of W is defined as the highest rank-one (quasi-, poly-) convex function not larger than W, see [2, 3, 4].

Proof. Let ψ denote the quantity on the right-hand side, i.e.,

$$\psi(F) = \begin{cases} |Fm|^2 - 1 & \text{if } \det F = 1 \text{ and } |Fs| \leq 1 \\ \infty & \text{else.} \end{cases}$$

We first show that ψ constitutes a lower bound for the polyconvex envelope of W, and hence for the other ones (see [3, 4, 7]). To prove this it suffices to show that ψ is polyconvex and that $\psi \leq W$. The polyconvexity of ψ follows from the fact that the function $|Fm|^2 - 1$ is convex, and the conditions $\det F = 1$ and $|Fs| \leq 1$ are polyconvex. It remains to show that $\psi \leq W$. This is trivial for all matrices on which $W = \infty$, hence we only consider the matrices of the form $F = Q(\mathrm{Id} + \gamma s \otimes m)$, where W is finite. A straightforward computation gives

$$|F^2| - 2 = |Fm|^2 - 1 = \gamma^2 \,.$$

Therefore on those matrices $\psi = W$, and globally $\psi \leq W$. This concludes the proof of the lower bound.

We now turn to the upper bound. We shall show that ψ constitutes an upper bound for the rank-one convex envelope of W. To do so, it suffices for any matrix F to find a pair of matrices F_+, F_- and weights $\lambda_+, \lambda_- \in (0, 1)$ such that $\mathrm{rank}(F_+ - F_-) = 1$, $\lambda_+ - \lambda_- = 1$, and

$$F = \lambda_+ F_+ + \lambda_- F_- \,, \qquad \psi(F) \leq \lambda_+ W(F_+) + \lambda_- W(F_-) \,.$$

Consider any matrix F such that $\det F = 1$ and $|Fs| \leq 1$. If $|Fs| = 1$ then necessarily $F = Q(\mathrm{Id} + \gamma s \otimes m)$, for some $Q \in SO(2)$ and $\gamma \in \mathbb{R}$, and there is nothing to prove. Assume therefore $|Fs| < 1$. Choose two unit vectors a, b and consider the rank-one perturbation of F given by

$$F_\mu = F + \mu a \otimes b \,. \tag{4}$$

The constraint $\det F_\mu = 1$ corresponds to $a^\perp F b^\perp = 0$, and gives $a = F b^\perp / |F b^\perp|$ (here and below, $(x, y)^\perp = (-y, x)$). It remains to determine the optimal b and μ.

The function $W(F_\mu)$ is finite only if $|F_\mu s| = 1$. Therefore for any given b the values of μ are necessarily those that satisfy

$$|F_\mu s|^2 - 1 = (b \cdot s)^2 \mu^2 + 2\mu (b \cdot s)(a \cdot Fs) + |Fs|^2 - 1 = 0 \,. \tag{5}$$

This is a quadratic equation in μ, with the last coefficient negative, and the first positive (except for $b = m$). It has two solutions of opposite sign, call them

μ_+ and μ_-. We conclude that for any choice of $b \neq m$, setting $a = Fb^\perp/|Fb^\perp|$, we have a laminate of the form

$$F = \lambda_+ F_+ + \lambda_- F_- \,, \qquad \lambda_+ = -\frac{\mu_-}{\mu_+ - \mu_-} \,, \qquad \lambda_- = \frac{\mu_+}{\mu_+ - \mu_-} \,,$$

where $F_+ = F_{\mu_+}$ and $F_- = F_{\mu_-}$. The corresponding energy is given by

$$E = \lambda_+ W(F_+) + \lambda_- W(F_-) = \lambda_+(|F_+|^2 - 2) + \lambda_-(|F_-|^2 - 2)$$

Computing explicitly $|F_\mu|^2 - 2 = \mu^2 + 2\mu a \cdot Fb + |F|^2 - 2$ and substituting we obtain

$$\begin{aligned} E &= |F|^2 - 2 + \lambda_+\mu_+^2 + \lambda_-\mu_-^2 = |F|^2 - 2 - \mu_+\mu_- \\ &= |F|^2 - 2 + \frac{1 - |Fs|^2}{(b \cdot s)^2} \end{aligned} \tag{6}$$

where we used the explicit expression for $\lambda_\pm$ and replaced the product of $\mu_+\mu_-$ with the value apparent from (5).

The optimal choice for b is determined as the one that minimizes (6), and is $b = s$. This gives

$$E = |F|^2 - 2 + (1 - |Fs|^2) = |Fm|^2 - 1$$

and therefore shows that the rank-one convex envelope of W is less than or equal to ψ (precisely, ψ is the first-lamination convex envelope of W). This concludes the proof for the rank-one convex and polyconvex envelopes. For the quasiconvex one an additional construction is needed in the boundary layer. This can be done using the convex integration results by Müller and Šverák [13] as discussed in [7], we omit the details.

Finally, we show that the matrices $F_\pm$ on which the laminate is supported have the same plastic slip γ (in absolute value). This corresponds to the condition $W(F_+) = W(F_-)$, or equivalently $|F_+m| = |F_-m|$. Since $m \cdot s = 0$, the latter is a trivial consequence of (4) and the fact that $b = s$. ☐

We finally remark that, much as in [7], in three dimensions the function W defined in (1) turns out to be quasiconvex. This is however to be seen as a degeneracy originating from the rigid-elasticity assumption, and not as a physically meaningful effect. The rank-one convex and polyconvex envelopes, indeed, are different from W, and are given by $|Fm|^2 - 1$ on the set $\{F \in \mathbb{R}^{3\times3} : \det F = |F(s \wedge m)| = |\operatorname{cof} F(s \wedge m)| = 1, |Fs| \leq 1\}$, and ∞ elsewhere. A proof of these facts can be obtained from the one of [7, Th. 2] with minor changes.

3. Discussion

For a comparison, we recall that the quasiconvex envelope of W_{CT} derived in [7] is

$$W_{\mathrm{CT}}^{\mathrm{qc}}(F) = \begin{cases} \lambda_2(F) - \lambda_1(F) & \text{if } \det F = 1 \text{ and } |Fs| \leq 1 \\ \infty & \text{else,} \end{cases} \tag{7}$$

where λ_i denote the ordered singular values of F, i.e., the eigenvalues of $(F^TF)^{1/2}$. The optimal microstructure was also in that case a simple laminate; one of the two matrices $F_\pm$ was a rotation.

In comparing with the present result two qualitative differences appear. Firstly, the relaxation of W_{CT} turned out to be isotropic, on the given subset of strain space, the present one is not. Secondly, the relaxation of W_{CT} involved a microstructure in which part of the sample had a purely elastic deformation; in the situation considered here instead the entire sample deforms plastically, the microstructure corresponds to oscillations in the sign of γ. This is in agreement with numerical results [8, 9, 10, 11].

Given these two results, it is interesting to guess the behavior of a mixed model, i.e., of a problem of the type

$$W_{\mathrm{mixed}}(F) = \begin{cases} \tau\gamma + \gamma^2 & \text{if } F = Q(\mathrm{Id} + \gamma s \otimes m) \quad \text{for } Q \in SO(2),\ \gamma \in \mathbb{R} \\ \infty & \text{else,} \end{cases}$$

for a small parameter τ. For small strains, i.e., for matrices whose distance from a rotation is small compared to τ, one expects that the optimal laminate will be analogous to the one obtained for W_{CT}, i.e., will contain one phase which is a rotation. For strains much larger than τ (but which still do not reach the hard constraint) we instead expect W to be a good model, and the optimal microstructure to involve two regions, with slip of opposite sign. A transition between exactly these two regimes is observed in faulting and kink banding of geological rocks and on experiments on compressed paper sheets [14, Fig. 1b], and it is tempting to imagine that the two phenomena are related. It is however at present not clear to which extent an energy like $W_{\mathrm{mixed}}(F)$ gives a good model for kink banding in rocks.

Acknowledgements

Useful discussions with Antonio Orlando and Mark Peletier are gratefully acknowledged. This work was supported by the Deutsche Forschungsgemeinschaft through the Schwerpunktprogramm 1095 *Analysis, Modeling and Simulation of Multiscale Problems.*

References

[1] M. Ortiz and E. A. Repetto, *Nonconvex energy minimization and dislocation structures in ductile single crystals*, J. Mech. Phys. Solids **47** (1999), 397–462.

[2] B. Dacorogna, *Direct methods in the calculus of variations*, Springer-Verlag, New York, 1989.

[3] S. Müller, *Variational models for microstructure and phase transitions*, in: Calculus of variations and geometric evolution problems (F. Bethuel et al., eds.), Springer Lecture Notes in Math. 1713, Springer-Verlag, 1999, pp. 85–210.

[4] G. Dolzmann, *Variational methods for crystalline microstructure - analysis and computation*, Lecture Notes in Mathematics, no. 1803, Springer-Verlag, 2003.

[5] S. Conti and M. Ortiz, *Dislocation microstructures and the effective behavior of single crystals*, Arch. Rat. Mech. Anal. **176** (2005), 103–147.

[6] C. Carstensen, K. Hackl, and A. Mielke, *Nonconvex potentials and microstructure in finite-strain plasticity*, Proc. Roy. Soc. London, Ser. A **458** (2002), 299–317.

[7] S. Conti and F. Theil, *Single-slip elastoplastic microstructures*, Arch. Rat. Mech. Anal. **178** (2005), 125–148.

[8] S. Bartels, C. Carstensen, K. Hackl, and U. Hoppe, *Effective relaxation for microstructure simulations: algorithms and applications*, Comp. Methods Appl. Mech. Engrg. **193** (2004), 5143–5175.

[9] C. Miehe, M. Lambrecht, and E. Gürses, *Analysis of material instabilities in inelastic solids by incremental energy minimization and relaxation methods: evolving deformation microstructures in finite plasticity*, J. Mech. Phys. Solids **52** (2004), 2725–2769.

[10] S. Bartels, C. Carstensen, S. Conti, K. Hackl, U. Hoppe, and A. Orlando, *Relaxation and the computation of effective energies and microstructures in solid mechanics*, preprint, to appear in Analysis, Modeling and Simulation of Multiscale Problems (A. Mielke, ed.), Springer, 2006.

[11] C. Carstensen, S. Conti, and A. Orlando, *Effective computation of single-slip elastoplastic microstructures in finite strains*, Proceedings of MMM 2006, this volume.

[12] S. Conti, *Microstructure and relaxation in single-crystal plasticity*, Oberwolfach Reports **2** (2005), 3000–3003.

[13] S. Müller and V. Šverák, *Convex integration with constraints and applications to phase transitions and partial differential equations*, J. Eur. Math. Soc. (JEMS) **1** (1999), 393–442.

[14] G. W. Hunt, M. A. Peletier, and M. A. Wadee, *The Maxwell stability criterion in pseudo-energy models of kink banding*, J. Struct. Geology **22** (2000), 669–681.

The Lattice Boltzmann Method: An emergent technique for the numerical simulation of complex fluids

Guy Courbebaisse[1], *Bastien Chopard*[2], *Jonas Latt*[2], *Michel Deville*[3], *Orestis Malaspinas*[3]

[1]*CREATIS INSA de Lyon, Bat. Blaise Pascal, 7 Av. Jean Capelle, 69621 Villeurbanne, France*
[2]*CUI, University of Geneva, 24, Rue du Général Dufour, 1211 Geneva 4, Switzerland*
[3]*EPFL STI ISE LIN, Station 9, 1015 Lausanne, Switzerland*

The Lattice Boltzmann Method is relatively recent and it allows the numerical simulation of complex physical phenomena in particular in the field of fluid mechanics. The modelling of systems or processes is carried out on a mesoscopic scale, in term of fictitious particles progressing in a discrete space time domain. This method is viewed as an approach using simple microscopic models to simulate macroscopic behaviour of fluid flows for example. The history of this method goes back to the theory of Lattice Gas Cellular Automata in the 1980ies.

The procedure leading the continuous equation to the formulation of the lattice Boltzmann method is exposed, and the derivation of the Navier-Stokes equation from the lattice Boltzmann equation is established. Today, in many different fields, modelling and numerical simulation in two and three dimensions are carried out with this method.

In the field of polymer injection moulding process, the numerical simulation of the filling phase gives realistic results with respect to industrial applications, taking in consideration two phases (Air and molten polymer).

As an illustration in fluid mechanics, we present numerical results for Newtonian and non Newtonian fluid flows for two simple geometries and for the filling of a plastic part.

Capillary Impregnation of Nanopores Studied with Fluid Particle Methods

Claudio Cupelli[1], Björn Henrich[2], Thomas Glatzel[1], Michael Moseler[2], Roland Zengerle[1], and Mark Santer[1,2]

[1]Laboratory for MEMS Applications, Department of Microsystems Engineering – IMTEK, University of Freiburg, Georges-Koehler-Allee 106, 79110 Freiburg, Germany, e-mail: cupelli@imtek.de
[2]Fraunhofer Institut für Werkstoffmechanik - IWM, Woehlerstrasse 9
79108 Freiburg, Germany, e-mail: san@iwm.fhg.de

ABSTRACT

We study the capillary impregnation of a nano-scale pore by Multibody Dissipative Particle Dynamics (MDPD) [4]. As an essential prerequisite for studying capillary phenomena, an adhesive wall model is introduced assuming a thermally roughened interface. It provides a constant and homogeneous temperature profile and avoids density oscillations. We demonstrate that the impregnation dynamics follows the classical Lucas-Washburn equation augmented by the effects of inertia and the dynamic contact angle. We show that a constitutive model for describing dynamic contact angles, e.g. the model of Cox [5], is suited for describing stationary conditions, while it is not adequate for describing transient dynamic processes as studied here.

1. Introduction to Multibody Dissipative Particle Dynamics

Multibody Dissipative Particle Dynamics (MDPD) is a particle based simulation method similar to Molecular Dynamics (MD), where particles move according to Newtons equation of motion with forces $\mathbf{F}_i$,

$$\mathbf{F}_i = \sum_j (\mathbf{F}_{ij}^C + \mathbf{F}_{ij}^D + \mathbf{F}_{ij}^R), \qquad (1)$$

resulting from the pair wise interaction, with neighboring particles in a cutoff range r_c, comprising a conservative, a random and a dissipative part [1]. If $\mathbf{r}_i$ denotes the particle position, the conservative force is acting in the central line between the particles i and j, where $\mathbf{r}_{ij} = \mathbf{r}_i - \mathbf{r}_j$, $r_{ij} = |\mathbf{r}_{ij}|$ and $\mathbf{e}_{ij} = \mathbf{r}_{ij} / r_{ij}$. In this work, the approach of Warren [4] is pursued, who adds a density dependent part directly to the force,

$$\mathbf{F}^C = A_{ij}\omega^C(r_{ij})\mathbf{e}_{ij} + B_{ij} \cdot (\overline{\rho}_i + \overline{\rho}_j)\omega_d{}^C(r_{ij})\mathbf{e}_{ij}, \qquad (2)$$

where $\overline{\rho}_i = \sum_{i \neq j} \omega_d{}^C(r_{ij})$ is the instantaneously weighted average local density and $\omega_d{}^C$ is a weight function on a smaller cutoff range r_d. The weight function $\omega^C(r) = (1 - r/r_C)$ vanishes for an inter-particle distance r_{ij} larger than a cutoff radius r_C. A temperature conserving thermostat is achieved by adjusting the strength of the random force $\mathbf{F}_{ij}^R = \sigma\omega^R(r_{ij})\xi_{ij}\mathbf{e}_{ij}$ and the viscous damping force $\mathbf{F}_{ij}^D = -\gamma\omega^D(r_{ij})(\mathbf{v}_{ij} \cdot \mathbf{e}_{ij})\mathbf{e}_{ij}$ via the fluctuation-dissipation theorem: $\sigma^2 = 2\gamma k_B T$, with the Boltzmann constant k_B and the temperature T of the system. Here σ

is the amplitude of the Gaussian shaped random variable ξ_{ij} and γ represents the strength of the viscous dissipation. With the conservative force given by equation (2), the equation of state (EOS) has a Van-der-Waals loop, which is necessary for generating free capillary surfaces.

2. Wall Model

An essential prerequisite for studying capillary phenomena is a realistic representation of the system boundaries, e.g. a no-slip condition at the walls. Possible strategies in MDPD to generate walls are either to use external potentials as walls or to generate walls by using particles. In this study we use the latter approach. In order to maintain the walls, the particles may either be: (i) fixed to their initial position or (ii) pinned by harmonic forces to their initial position, which results in a thermally roughened surface. The second approach clearly reduces high density oscillations, see figure 1, that should only be present if truly atomistic scales are to be modeled.

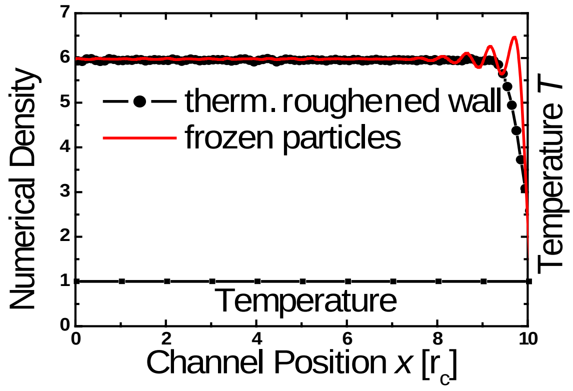

Figure 1: Density distribution in a slit of a width of $20r_c$ for different wall models: (i) solid line represents a wall with frozen particles, (ii) solid line with circles represents a thermally roughened wall.

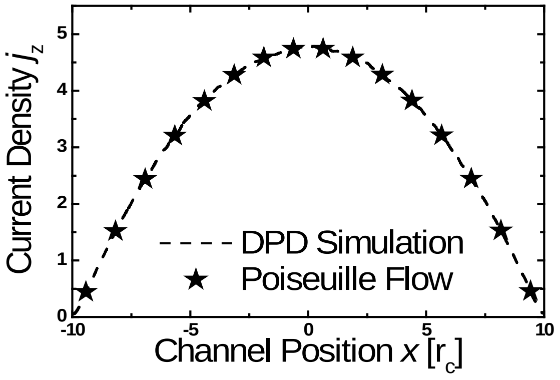

Figure 2: Flow in a slit of width of $20r_c$ obtained by MDPD simulation (dashed line) compared to a fit of a Poiseuille flow (stars).

In addition to a homogeneous temperature and density profile across the interface, the wall concept introduced here leads to a no-slip boundary condition with a perfect Poiseuille profile in the slit, see figure 2.

3. Impregnation Characteristics

Inertia and the dynamic contact angle play a significant role on the time scale of the simulation considered here. The dynamic behavior during capillary filling is studied and compared to the analytical solution for the problem balancing the momentum change dp_{fluid}/dt of the fluid, the pressure drop due to viscous losses $12\eta/b^2 \cdot z \cdot dz/dt$ and the driving capillary pressure $2\sigma/b \cdot \cos(\theta_d)$:

$$\frac{dp_{fluid}}{dt} = \frac{2\sigma}{b}\cos(\theta_d) - \frac{12\eta}{b^2} z \frac{dz}{dt} \qquad (3)$$

Here z denotes the filling heights, η the viscosity of the fluid, b the height of the slit and σ is the surface tension of the fluid. Equation (3) is an extension of the Lucas-Washburn equation, $0 = 2\sigma / b \cdot \cos(\theta_0) - 12\eta / b^2 \cdot z \cdot dz / dt$, where also inertia and the dynamic contact angle are accounted for.

In order to solve the problem by numerical integration, the value of the dynamic contact angle θ_d has to be known. The dynamic contact angle θ_d may be provided by different strategies, either: (i) a model or (ii) by extracting the dynamic contact angle during the MDPD-simulation of the filling process itself.

Case (i) means that there is a closed analytical description for the problem since θ_d is known and can directly be inserted into equation (3) to solve the problem. If this doesn't lead to a satisfactory result then a MDPD-simulation is needed in order to check the validity of equation (3).

At first, the dynamic contact angle behavior reproduced by the MDPD-simulation is extracted from a separate plug-flow MDPD-simulation, see figure 3, where the capillary number, $Ca = \eta / \sigma \cdot v$, is fixed for a time scale until an equilibrium of the dynamic contact angle θ_d is reached, representing a stationary situation. The result, see figure 3, shows that the behavior for a stationary condition can be described by the model of Cox [5] for dynamic contact angles.

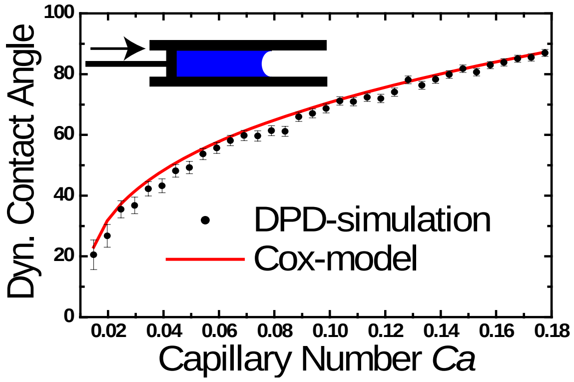

Figure 3: Dynamic contact angle behavior over the capillary number extracted from a series of stationary MDPD-simulations compared to the model of Cox [5].

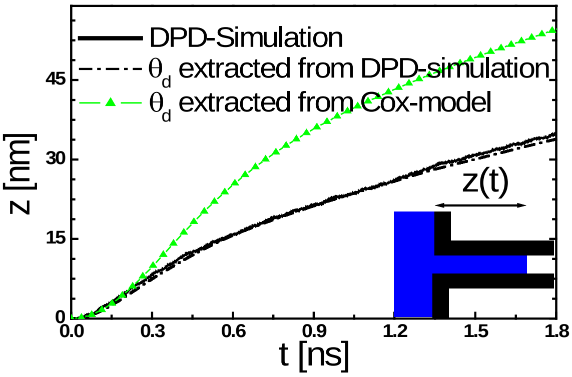

Figure 4: Filling dynamics obtained by MDPD-simulation compared to numerical integration of equation (3) for: (i) the model of Cox and (ii) the dynamic contact angle extracted from the MDPD-simulation.

The model of Cox is then inserted into equation (3) and compared to the dynamical capillary filling process resulting from the MDPD-simulation (see figure 4 triangles). From the pronounced deviation between equation (3) using the model of Cox compared to the MDPD-simulation two possible conclusions may be inferred: (i) either the extension of the Lucas-Washburn equation, i.e. equation (3), is not applicable or (ii) that the dynamic contact angle predicted by the model of Cox does not correspond to the dynamical situation during the filling process. Therefore, the dynamic contact angle during the capillary impregnation is also extracted from the MDPD-simulation online and is inserted into equation (3) in order to check equation (3) for consistency. The resulting curve perfectly agrees with the result obtained by the MDPD-simulation indicating that equation (3) is correct.

Conclusion & Outlook

This example shows that present constitutive laws for dynamic contact angles are not adequate for describing transient dynamic behavior. One reason for this is that in contrast to assumptions in existing theories the dynamic contact angle depends strongly on the flow field as a whole, which is strongly affected by the specific situation, e.g. the geometry or inertia, which has lately been shown also experimentally [6].

The result of our study indicates that transient dynamic capillary processes may not be described within present theories for dynamic contact angles but instead require a simulation of the system with MD or much more efficiently with MDPD.

References

[1] P. J. Hoogerbrugge and J. M. V. A. Koelman, "Simulating Microscopic Hydrodynamic Phenomena with Dissipative Particle Dynamics," Europhysics Letters, vol. 19, no. 3, pp. 155-160, June1992.

[2] P. Espanol, "Hydrodynamics from Dissipative Particle Dynamics," Physical Review e, vol. 52, no. 2, pp. 1734-1742, Aug.1995.

[4] P. B. Warren, "Vapor-liquid coexistence in many-body dissipative particle dynamics," Physical Review e, vol. 68, no. 6 Dec.2003.

[5] R.G. Cox, "Inertial and viscous effects on dynamic contact angles", Journal of Fluid Mechanics, vol. 357, pp. 249-278, 25 Feb.1998.

[6] R.G. Cox, "Experimental evidence of nonlocal hydrodynamic influence on the dynamic contact angle", Physics of Fluids, vol. 11, no. 8, pp. 1995-2007, Aug.1999.

Mi2cell: A generic tool for linking micro features into finite element solvers

Sumitesh Das

TATA STEEL, Automation Division (G-84), TATA STEEL, 831001 Jamshedpur, India

Integrating microstructural details and their relationships across time and length scales into structural, mechanical and electrical analyses is of paramount importance in designing materials and processes for superior performance and durability. It is necessary to design and develop tools that enable the transfer of relevant information from micro features at various length scales to the macro entity and vice-versa.

The paper reports the design and development of a micro-feature to cell converter Mi2Cell) software in an attempt to transfer the micro-macro information. The software uploads the micro information either in 2D digital micro data or EBSD data and translates these into appropriately scaled cellular automata (CA) cells. Each cell represents a material point that is representative of an underlying micro-feature e.g. a grain boundary, a dislocation rich or deplete region. Mi2Cell reads in the input deck of an overlying finite element and links the micro feature with the integration point of the element. The output from Mi2Cell is compatible with the user-defined material subroutine USDFLD of ABAQUS Implicit FE solver.

Based on the information grained from the micro-feature, Mi2Cell generates “self-similar” micro-features having consistency at the macro level but are locally distinct. At present, Mi2Cell generates the micro-features for single-phase grain based microstructures. Work is presently underway to extend Mi2Cell capability to generate “self-similar” dual and multi phase micro-features for analyses.

Adaptive Resolution Molecular Dynamics Simulation: Changing the Degrees of Freedom on the Fly

Luigi Delle Site

Max-Planck Institute for Polymer Research, Mainz, Germany

We present a new adaptive resolution technique for particle-based efficient multiscale molecular dynamics (MD) simulations. The presented approach is tailor-made for molecular systems where atomistic resolution is required only in spatially localized domains whereas a lower mesoscopic level of detail is sufficient for the rest of the system.

Our method allows an on-the-fy interchange between a given molecules atomic and coarse-grained level of description, enabling to reach large length and time scales while spatially retaining atomistic details of the system. The new approach is tested on a model system of a liquid of tetrahedral molecules. The simulation box is divided into two regions: one containing only atomistically resolved tetrahedral molecules, the other containing only one particle coarse-grained spherical molecules. The molecules can freely move between the two regions while changing their level of resolution accordingly. Both, the coarse grained as well as the atomistically resolved system have the same statistical properties at the same physical conditions.

References:

[1] Matej Praprotnik, Luigi Delle Site, and Kurt Kremer, J. Chem. Phys. 123, 224106(2005).

[2] Matej Praprotnik, Luigi Delle Site, and Kurt Kremer: Adaptive Resolution Scheme (AdResS) for Efficient Hybrid Atomistic/Mesoscale Molecular Dynamics Simulations of Dense Liquids. Phys.Rev. E (2006).

[3] Matej Praprotnik, Kurt Kremer and Luigi Delle Site: Statistical mechanics foundations of the spatially adaptive resolution method. Preprint.

Valence-dependent analytic bond-order potentials for transition metals

Ralf Drautz

University of Oxford, Department of Materials, Parks Road, OX1 3PH, Oxford, United Kingdom

We present a new analytic atom-based interatomic bond-order potential (BOP) for transition metals that depends explicitly on the valence [1]. The potential is derived from the tight-binding electronic structure and may be regarded as a systematic extension of the second-moment Finnis-Sinclair potential to include higher moments. This analytic BOP predicts not only the structural trend from hcp to bcc to hcp to fcc that is observed across the non-magnetic 4d and 5d transition metal series, but also the different magnetic behaviour of the bcc, fcc and hcp phases of the 3d transition metal iron. The potential describes alloy formation correctly, so that is should be suitable for the simulation of complex phases in intermetallic compounds.

[1] R. Drautz and D.G. Pettifor, Phys. Rev. B (submitted).

The Evolution of Excess Dislocation Density in Torsion

Claude FRESSENGEAS [1], *V. Taupin* [1], *S. Varadhan* [2], *A. J. Beaudoin* [2]

[1] *Laboratoire de Physique et Mecanique des Materiaux, University P. Verlaine - Metz / CNRS, Ile du Saulcy, 57045 Metz, France*

[2] *Department of Mechanical and Industrial Engineering, University of Illinois, 61801 Champaign, Urbana, United States of America*

The evolution of excess dislocation density in torsion is addressed by using a recent theory for the coupled dynamics of statistically distributed dislocations and excess dislocations [1, 2]. Excess dislocations are defined as a continuous manifestation of lattice incompatibility. Statistically distributed dislocations lead to compatible deformation and make no contribution to internal stresses. Both dislocation species contribute to plastic flow. Their dynamics are coupled in the sense that gradients in the compatible plastic distortion field generate excess dislocations. Further coupling occurs at large strains, when excess dislocations contribute to forest hardening.

Plastic distortion gradients are inherent to torsion testing. Our numerical simulations suggest that under a positive torque, positive excess screw dislocations nucleate in planes normal to the torsion axis, while negative excess screws parallel to the axis form in planes containing the axis. By adding their contribution to plastic flow to that of statistically distributed dislocations, excess dislocations induce shear stresses lower than predicted from conventional plasticity. However, for sufficiently small wire radii, transport of the excess dislocations toward the center becomes effective and pile-ups of screws form about the axis. The torque (scaled with respect to the cubed radius) needed for a certain rotation then increases, albeit remaining less than predictions from conventional plasticity. Size effects are therefore occurring. The simulated dislocation structures, the stress fields and their dynamics are illustrated in ice crystals oriented for basal slip and in copper, as motivated by the experimental studies given in [3] and [4], respectively.

[1] A. Acharya, A. Roy, J. Mech. Phys. Solids, in press

[2] S. Varadhan, A.J. Beaudoin, C. Fressengeas, Proceedings of Science (2006), submitted.

[3] M. Montagnat, J. Weiss, P. Duval, H. Brunjail, P. Bastié, J. Gil Sevillano, Phil. Mag., in press.

[4] N.A. Fleck, G.N. Muller, M.F. Ashby, J.W. Hutchinson, Acta Metall. Mater. (1994), 42, 475.

Variational models for plasticity by homogenization of discrete dislocations

Adriana Garroni[1], *Giovanni Leoni*[2]

[1]*Universita' di Roma „La Sapienza", Dipartimento di Matematica, piazzale Aldo Moro 2, 00185 Roma, Italy*
[2]*Department of Mathematical Sciences, Carnegie Melon University, Pittsburgh, Pennsylvania, 15213, USA*

We consider a 2D model for edge dislocations, where points represent dislocations and the crystal behaves elastically far from the core. We study, in a dilute regime, the limit as the number of points (dislocations) tends to infinity and we obtain a limit problem given by the elastic energy and a term depending on the Curl of the plastic deformation (the dislocations density).

A Combined Atomistic/Continuum Method For Thermoelastic Problems

Simon P.A. Gill and Kenny Jolley

Department of Engineering, University of Leicester,
University Road, Leicester, UK, LE1 7RH
spg3@le.ac.uk

ABSTRACT

A method for embedding a non-equilibrium atomistic simulation within a continuum model is proposed. This paper focuses on conservation of the flow of thermal energy between the two descriptions for the case of a one-dimensional chain. Firstly, the choice of an appropriate atomistic model is addressed. For a Lennard-Jones chain, it is found that adverse phonon scattering at the interface makes the temperature in the chain difficult to control effectively. Also, it is known that the conductivity of such a chain is divergent. The ϕ^4 potential is consequently adopted as an ideal model system to avoid these problems. Atomistic heat fluxes are calculated and conserved to reproduce steady state heat flow along a mixed atomistic/continuum chain.

1. Introduction

The boundary conditions for molecular dynamics (MD) simulations in the condensed phase are a compromise between correct representation of the far field and minimization of the system size due to computational constraints. In recent years, concurrent multiscale methods have been developed for crystalline solids in which the complex response of the far field is represented by a coarse-grained continuum region constructed from finite elements (see [1,2] for reviews). The requirements of the continuum far field depend on the nature of the simulation, generally either sampling or dynamics. If the purpose of simulation is sampling of near equilibrium or steady state quantities, then typically only slowly-changing thermodynamical or statistical quantities are of interest and inertial effects are small. Rapid changes occur in truly dynamic situations such as fast fracture.

Dynamical simulations are complicated by the reflection of high frequency phonons from the interface between the atomistic and continuum regions. This leads to energy trapping and localized heating [2]. Correct transmission of phonons across the interface [1-4] is only necessary if the far boundaries can be seen during the simulation period (e.g. MEMS) or there are two atomistic regions which need to interact dynamically via the continuum medium (e.g. two cracks). We assume here that absorption of phonons at the interface is a sufficient requirement. This type of approach [5,6] has allowed the elastic boundary conditions to be specified at a position remote from the atomistic region. However, the thermal boundary condition (constant temperature) is at the edge of the atomistic region. This could be highly restrictive on the evolution of thermal energy within the atomistic region. Liu [7] has recently demonstrated that MD simulations of nanoindentation are very sensitive to restricted thermostatic control. Keeping the boundary temperature constant also restricts simulations to be near to thermal equilibrium, whereas non-equilibrium conditions (e.g. temperature gradients) may be of interest.

It is the purpose of this work to investigate the possibility of using combined atomistic/continuum algorithms to allow MD simulations to be conducted with remote thermal and elastic boundary conditions. This paper focuses on the thermal model, which has not to date been the focus of much attention [1]. Two issues need to be addressed. Ensuring compatibility between the atomistic and continuum descriptions is discussed in section 2. Smooth transfer of information across the interface between the two models is the subject of section 3.

2. Non-Equilibrium Molecular Dynamics

Before proceeding further, it is necessary to determine the continuum thermal properties of our atomistic model: namely the thermal conductivity *k*. The conductivity can be determined from equilibrium simulations using linear response theories such as the Green-Kubo formula [8]. An alternative method is to use Non-Equilibrium Molecular Dynamics (NEMD). In this case, a steady state temperature gradient, ∇T, is established by thermostatting two different regions of the simulation at different temperatures. The heat flux, *j*, in the unthermostatted region between the thermostat is then calculated and the conductivity determined from Fourier's law for macroscopic heat flow

$$j = -k\nabla T\ . \tag{1}$$

The NEMD approach is directly relevant to the class of problems which we intend to solve, and therefore it is adopted here. The situation described above is not as straightforward as it may appear. Details of the atomistic simulation are given below, along with a discussion of potential difficulties.

2.1 The atomistic model

In this paper we restrict our interest to heat conduction in insulators via phonon interaction (i.e. conduction by electrons is neglected). Also, for the benefit of model development, we consider a one-dimensional chain of atoms. The temporal evolution of the system is then described by a simple classical Hamiltonian

$$H = \sum_{i=1}^{N}\left[\frac{p_i^2}{2m_i} + U(x_i) + V(x_{i+1} - x_i)\right] \tag{2}$$

where $p_i = m_i\dot{x}_i$, m_i and x_i are the momentum, mass and displacement (from its equilibrium position) of the *i*th atom and *N* is the number of atoms in the chain. The potential function $V(r)$ is due to interaction between atoms. The potential $U(x)$ is known as an on-site potential. Its relevance will be seen in sub-section 2.3. It represents interaction between the atomic chain and an external substrate. The dynamics of the system described by (2) are

$$m_i\ddot{x}_i = -\frac{\partial(U+V)}{\partial x_i}\ . \tag{3}$$

2.2 Thermostats and phonon scattering

To establish a temperature gradient in our NEMD simulation, it is necessary to inject kinetic energy into one end of the chain and to remove it from the other end. This is achieved by the use of thermostatting algorithms. Two well-known examples are the Langevin thermostat and the Nosé-Hoover thermostat.

The Langevin thermostat is a stochastic thermostat which adds a random force to the particle motion along with an appropriate damping term such that

$$m_i \ddot{x}_i = -\frac{\partial (U+V)}{\partial x_i} - \gamma m_i \dot{x}_i + R f_L \tag{4}$$

where γ is a damping coefficient, $0 \le R \le 1$ is a uniformly distributed random variable and $f_L = \sqrt{\frac{6\gamma m_i T_c}{\Delta t}}$ is the magnitude of the stochastic force for a target temperature T_c and a time step Δt. The advantage of this thermostat is that it is easy to implement and the target temperature can be specified for each atom, i.e. a non-uniform temperature distribution can be specified. One variant, stadium damping, has been shown to be an effective means of phonon absorption [5].

The Nosé-Hoover thermostat is a deterministic thermostat which maintains the average temperature of an atomic ensemble at a target value. This is widely used for constant temperature dynamical simulations, but is less effective when the ensemble has a variation in thermal conditions over its boundaries such as in NEMD. This is because the average temperature is maintained, but any temperature distribution which satisfies this average is possible. One solution is to apply the thermostat only to atomic ensembles within which no net heat flow is expected to occur [9]. In one-dimension, this corresponds to thermostatting a single atom. Although this does not strictly conform to the requirements for sampling the canonical ensemble, it is widely used in low-dimensional NEMD. The motion of a thermostatted particle is described by

$$\begin{aligned} m_i \ddot{x}_i &= -\frac{\partial (U+V)}{\partial x_i} - \xi m_i \dot{x}_i \\ Q\dot{\xi} &= \frac{m_i \dot{x}_i^2}{k_B T_c} - 1 \end{aligned} \tag{5}$$

where k_B is Boltzmann's constant and Q is a thermal mass.

We assume for the rest of this paper that Boltzmann's constant and the atomic spacing, mass and spring stiffness (in the harmonic limit) are unity. The two thermostats above are applied to a 100 atom Lennard-Jones chain such that $U(x) = 0$ and $V(r) = \frac{1}{72}\left(\frac{1}{r^{12}} - \frac{2}{r^6}\right)$. Only nearest neighbour interactions are used. The damping coefficient, $\gamma = \frac{1}{2}\omega$, is half the (harmonic) oscillation frequency, $\omega = \sqrt{2}$. The time step is 1/50th of the periodic time, $\tau = 2\pi/\omega$. The extremities of the chain are fixed ($\ddot{x}_0 = \ddot{x}_{N+1} = 0$) and the thermostats applied to the end atoms (i=1 and i=N). The non-dimensionalised target temperatures are T_1=0.3 and T_N=0.2. Simulations are allowed to reach a steady state over a time of $10^5\tau$ and then the average temperature $\langle T \rangle = \langle \tfrac{1}{2} m_i \dot{x}_i^2 \rangle$ determined over a similar subsequent period, where $\langle . \rangle$ denotes the time ensemble average. The results are shown in Fig. 1. It is clear that the results are not good. There is a large temperature discontinuity at the ends, such that the temperature gradient observed in the simulation is not the applied temperature gradient. In the case of the Langevin thermostats, practically no temperature gradient develops. This effect has been widely observed and is mainly explained by phonon scattering at the interface [8]. It is difficult to avoid and exists in 1D, 2D and 3D. The net energy flux between particles (see Eqn. (9) later on) is due to long-term correlations between their motions. Any thermostat will artificially alter the particle motion and corrupt this correlation. The Nosé-Hoover thermostat is better than the Langevin thermostat as deterministic methods naturally exhibit longer correlation times than stochastic methods. Free ends, rather than fixed ones, can reduce this scattering effect [8].

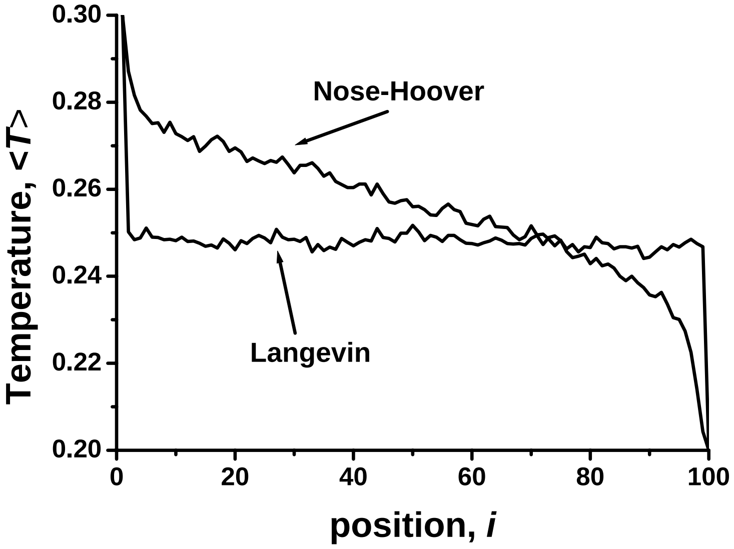

Figure 1: Temperature profile for a 100 atom Lennard-Jones chain with fixed ends using (a) stochastic Langevin thermostats and (b) deterministic Nosé-Hoover thermostats, applied to each end. The discontinuity in the temperature profile at each end is due to phonon scattering.

2.3 Divergence of the thermal conductivity

It is expected that an atomic system will obey Fourier's law (1) such that the thermal conductivity, *k*, will be constant in the macroscopic limit, i.e. although there are expected to be system size effects [10], *k* will converge as the system size increases. This is not always found to be the case in low-dimensional systems. A lengthy review of this subject is provided by Lepri et al. [8]. To briefly summarise, it is predicted (and normally found) that for momentum conserving potentials ($U(x)=0$), for a system of characteristic dimensional size *N*,

$$\begin{array}{ll} k \propto N^{2/5} & \text{in 1D} \\ k \propto \ln N & \text{in 2D} \\ k \propto \text{constant} & \text{in 3D.} \end{array} \tag{6}$$

Hence, a 1D chain will possess a divergent thermal conductivity for a momentum conserving potential. This is not desirable. Working with a 1D chain is desirable from a model development point of view, but it introduces problems which will not be an issue in 3D. Hence we choose to utilize an on-site potential, $U(x)$, to break momentum conservation. The simplest is the ϕ^4 potential model. The form used here is a simple harmonic interaction potential with an anharmonic on-site potential such that

$$\begin{aligned} U(x) &= \tfrac{1}{4}\beta x^4 \\ V(r) &= \tfrac{1}{2}(r-1)^2 \end{aligned} \tag{7}$$

where we take $\beta = 2$. The use of a harmonic interaction potential has the advantage that the thermal expansion coefficient is zero. Therefore there is no coupling between the thermal field and the quasi-static elastic field, which simplifies the problem. Normally, a harmonic interaction potential cannot be used for thermal simulations as the conductivity is infinite [8]. This is because thermal energy transfer occurs via phonon interaction. However, in this case, the on-site potential generates the anharmonic response required for phonon interaction.

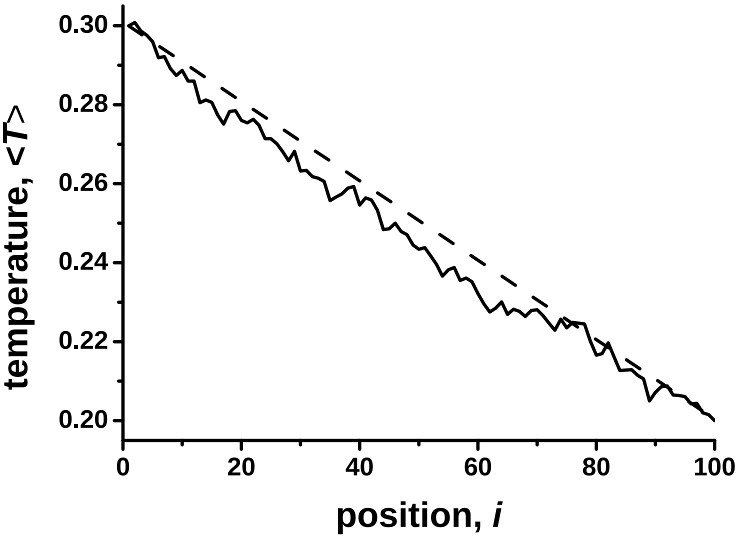

Figure 2: Temperature profile for a 100 atom ϕ^4 chain with fixed ends using two Nosé-Hoover thermostats. This on-site potential model reduces phonon scattering and has a convergent thermal conductivity. The dashed straight line is for reference.

The temperature profile for the ϕ^4 model for the Nosé-Hoover thermostats is shown in Fig. 2, under identical conditions to those specified for Fig.1. It is noted that the on-site potential has significantly reduced the temperature discontinuity at the ends due to scattering. A similarly good result is also obtained for the Langevin thermostat. The profile is slightly non-linear, presumably because the conductivity changes with temperature. This effect will be neglected for the purposes of simplicity here. The thermal conductivity can be calculated from this simulation given a knowledge of the heat flux. This can be calculated in two ways. Firstly, the energy injected into the hot end (which should be equal to the energy removed from the cold end on average) is the rate of work done by the Nosé-Hoover thermostat

$$j_i = -\xi m_i \dot{x}_i^2 . \tag{8}$$

Secondly, the heat flux communicated between atoms *i* and *i+1* is given by

$$j_i = -\tfrac{1}{2}(\dot{x}_{i+1} + \dot{x}_i) f_i \tag{9}$$

where f_i is the force between atoms *i* and *i+1* due to the interaction potential. It can be confirmed that this is constant (averaged over time) at all points in the lattice and that (8) and (9) give equivalent values. Equating the flux with Eqn. (1) gives the thermal conductivity. This is shown as a function of chain length in Fig. 3 for a fixed temperature difference of 0.1 as in Fig. 2. This confirms that convergence is achieved.

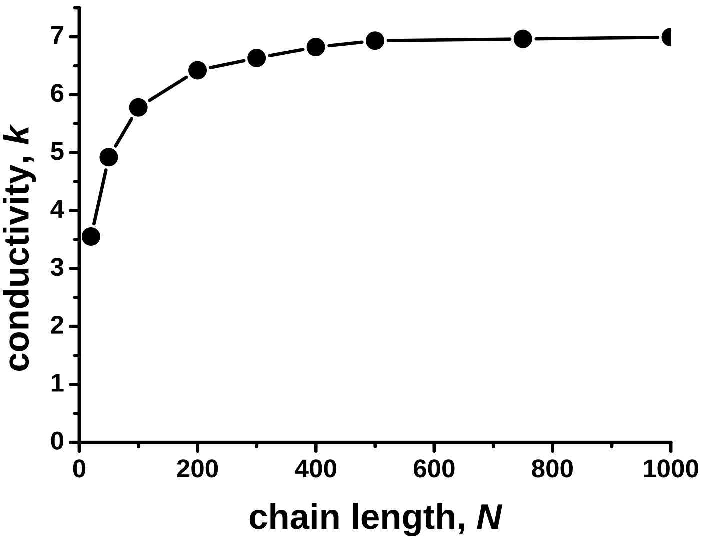

Figure 3: The thermal conductivity of the ϕ^4 chain as a function of chain length *N*. As the chain length increases the conductivity converges to a finite value.

3. A Combined Atomistic/Continuum Model

Having proposed a suitable atomistic model and derived a compatible macroscopic model in section 2, it is the purpose of this section to embed the NEMD simulation within a continuum one. A continuum chain consisting of *M* nodes is added to each end of the atomistic chain. The nodes are unit distance apart and fixed in space. The temperature variable at each node, T_i, represents the time-averaged kinetic energy of an equivalent atom at that location, where $i = -M + 1,...,0$ in the first chain and $i = N + 1,..., N + M$ in the second. There is no coarse-graining in the continuum chain here, although this process is trivial. The evolution of the atomistic region has been described in section 2. The only difference is that the target temperatures of the two ends of the atomistic chain, T_1 and T_N, are now variables to be determined. Note that all these temperatures are macroscopic variables, temperatures derived from atomistic kinetic averages are denoted by $\langle T_i \rangle$, where $i = 1,..., N$. The evolution of the system must satisfy flux conservation

$$k_B \dot{T}_i = j_{i+1} - j_i . \tag{10}$$

where j_i is the heat flux from atom *i* to atom *i+1*. The above holds at all points in the simulation where, from (1), (8) and (9), one can write

$$j_i = \begin{cases} -k(T_{i+1} - T_i) & \text{for } i = -M+1,\ldots,-1 \\ -\xi_1 \dot{x}_1^2 & \text{for } i = 0 \\ -\tfrac{1}{2}(\dot{x}_{i+1} + \dot{x}_i) f_i & \text{for } i = 1,\ldots,N-1 \\ +\xi_N \dot{x}_N^2 & \text{for } i = N \\ -k(T_{i+1} - T_i) & \text{for } i = N+1,\ldots,N+M-1 \end{cases} \tag{11}$$

We use the actual heat flux into the atomistic simulation, defined by (8), rather than the macroscopic heat flux (1), as the two are only identical over long time scales and the target temperature is required to respond rapidly. However, the target temperatures, T_1 and T_N, evolve rapidly under the above scheme due to inevitably large rapid fluctuations in the atomistic fluxes (9). As the target temperatures themselves are used to control the rapidly fluctuating thermostat variables (5), this renders the system unstable. One simple correction to this is to use time averaged atomistic fluxes $\langle j_i \rangle$ rather than instantaneous ones. Note that there are two definitions of the temperature for the thermostatted atoms, e.g. T_1 and $\langle T_1 \rangle$, a comparision of which could also be used to enhance the stability of the algorithm if required. In the case of steady state heat flow considered here, the flux averaging is sufficient.

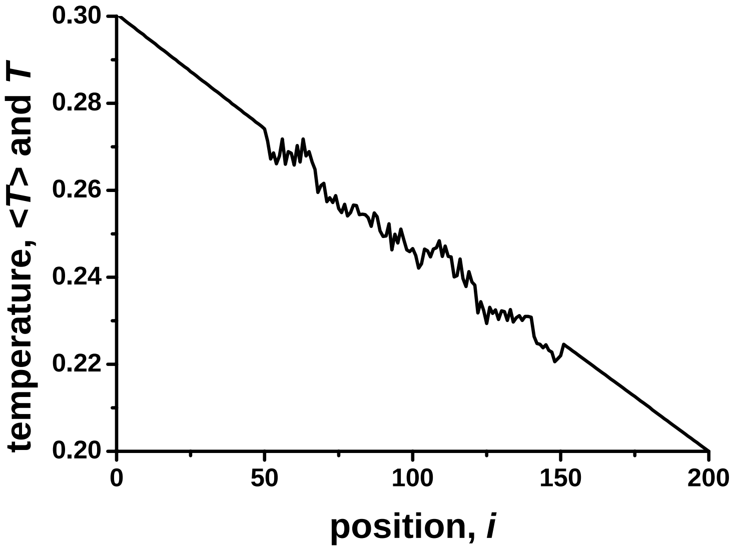

Figure 4: The temperature profile along a combined atomistic/continuum chain of 200 atoms/nodes. The first and last 50 nodes are in the continuum region. The central 100 atoms are in the atomistic region.

The temperatures at the ends of the continuum chain are fixed to be $T_{-M+1} = 0.3$ and $T_{N+M} = 0.2$. We take *M*=50 and *N*=100. The atomistic region is initially thermalised using an appropriate random Gaussian distribution of velocities. The resulting temperature distribution is shown in Fig. 4. The two target thermostat temperatures oscillate around the expected average values for a linear profile. The average macroscopic conductivity for a 100 atom chain, *k*=5.78, was used. However, the attractiveness of this algorithm is that it is relatively insensitive to this value. This is because the most influential fluxes, which regulate the flow of heat in to and out of the atomistic region, are derived from the atomistic region themselves and do not rely on the value of k. This is very important, as the actual measured conductivity varies with temperature and time.

Acknowledgements

K Jolley gratefully acknowledges the support of EPSRC grant no. EP/P501547/1.

References

1. S. P. Xiao and T. Belytschko, ‘A bridging domain method for coupling continua with molecular dynamics’, Comput. Methods Appl. Mech. Engrg. **193,** 1645 (2004).
2. W. K. Liu, E. G. Karpov, S. Zhang and H. S. Park, An introduction to computational nanomechanics and materials’, Comput. Methods Appl. Mech. Engrg. **193,** 1529 (2004).
3. J. Q. Broughton, F. F. Abrahams, N. Bernstein and E. Kaxiras, ‘Concurrent coupling of length scales : Methodology and application’, Phys. Rev. B **60**, 2391 (1999);
4. R. E. Rudd and J.Q. Broughton, Phys. Stat. Sol. B, ‘Concurrent coupling of length scales in solid state systems’, **217,** 5893 (2000).
5. S.Qu, V. Shastry, W.A. Curtin and R.E. Miller, ‘A finite temperature dynamic coupled atomistic/discrete dislocation method’, Modelling Simul. Mater. Sci. **13** 1101 (2005).
6. S.P.A. Gill, Z. Jia, B. Leimkuhler and A.C.F. Cocks, ‘Rapid thermal equilibration in coarse-grained molecular dynamics’, Phys. Rev. B. **73**, 184304 (2006).
7. W. K. Liu, E. G. Karpov and H. S. Park, personal communication.
8. S. Lepri, R. Livi and A. Politi, ‘Thermal conduction in classical low-dimensional lattices’, Physics Reports **377,** 1 (2003).
9. Z. Huang and Z. Tang, ‘Evaluation of momentum conservation influence in non-equilibrium molecular dynamics methods to compute thermal conductivity’, Physica B **373** 291-296 (2006).
10. G.Chen, D. Borca-Tasciuc and R.G. Yang, ‘Nanoscale heat transfer’, Encyclopedia of Nanoscience and Nanotechnology (American Scientific publishers, 2004).

Simulation of Aggregating Beads in Microfluidics on High Performance Computers With a Fluid Particle Method

Thomas Glatzel[1], Claudio Cupelli[1], Uwe Kuester[3], Roland Zengerle[1], and Mark Santer[1,2]

[1]Laboratory for MEMS Applications, Department of Microsystems Engineering –
IMTEK, University of Freiburg, Georges-Koehler-Allee 106, 79110 Freiburg, Germany.
[2]Fraunhofer Institut für Werkstoffmechanik - IWM, Woehlerstrasse 9
79108 Freiburg, Germany. e-mail: mark.santer@iwm.fraunhofer.de
[3]High Performance Computing Center - HLRS – University of Stuttgart,
Nobelstrasse 19, 70569 Stuttgart, Germany.

ABSTRACT

We present computer simulations of the dynamics of beads in three dimensional micro flows studied with a Fluid Particle (FP) approach [1]. Our code has been parallelised employing dynamic load balancing and domain decomposition, allowing for the simulation of large enough systems in order to bridge the gap from mesoscopic scales to an effective description of complex and rheological fluids that are of relevance in micro- and nanofluidics. All constituents, channel walls, suspended objects etc. are made of FP, allowing for a very efficient implementation of the simulation code on parallel computers. The simulation method employed represents hydrodynamics in the continuum by discrete elements, so called Fluid Particles (FP) [2]. Rigid body motion of arbitrarily shaped extended objects is efficiently described by quaternion dynamics [3, 4], and arbitrary shaped geometries are generated via external CAD tools and imported into the simulation. As an application, we study the aggregation of hundreds of polystyrene (PS) beads in a flat assay structure and compare to a corresponding experiments [5]. The simulation has been tested on systems ranging from a single processor workstation up to PC-based clusters such as Dual-Core Opteron and high performance computers (HPC) (NEC Xeon EM64T Cluster).

1. Introduction to Fluid Particle Methods and Quaternions

In the simplest form of the Fluid Particle Method the force $\mathbf{F}_i$ acting on a particle is the sum of pairwise conservative, dissipative and random forces $\mathbf{F}_i = \sum\left(\mathbf{F}_{ij}^C + \mathbf{F}_{ij}^D + \mathbf{F}_{ij}^R\right)$ between particles in a certain cutoff radius r_C by solving Newtonian equations of motion with a Velocity-Verlet algorithm [1, 2]. If $\mathbf{r}_i$ denotes the particle position, the conservative force $\mathbf{F}_{ij}^C = A_{ij}\omega^C(r_{ij})\mathbf{e}_{ij}$ is a soft repulsion acting in the central line between particle i and j where $\mathbf{r}_{ij} = \mathbf{r}_i - \mathbf{r}_j$, $r_{ij} = \left|\mathbf{r}_{ij}\right|$ and $\mathbf{e}_{ij} = \mathbf{r}_{ij} / r_{ij}$. The weight function $\omega^C(r) = \left(1 - r / r_C\right)$ vanishes for an interparticle distance r larger than a cutoff radius r_C usually set to the unit of length in all simulations. The combination of the dissipative and the random force acting as a thermostat in the simulation if the amplitudes σ of the Gaussian shaped random variable ξ_{ij} and the viscous dissipation γ satisfy a fluctuation-dissipation theorem: $\sigma^2 = 2\gamma k_B T$ with the Boltzmann constant k_B and the temperature T of the system. With the usual choice for the weight functions $(\omega^R)^2 = \omega^C$ [6] the dissipative force is given as $\mathbf{F}_{ij}^D = -\gamma\omega^D(r_{ij})\left(\mathbf{v}_{ij} \cdot \mathbf{e}_{ij}\right)\mathbf{e}_{ij}$ and the random force as $\mathbf{F}_{ij}^R = \sigma\omega^R(r_{ij})\xi_{ij}\mathbf{r}_{ij}$.

Extended objects are modelled by “freezing” single particles into one arbitrarily shaped object. The dynamics of the objects as a whole is determined by center of mass motion and that of the body axes. In particular, the rotational motion of the quaternion approach is applied where four parameters (quaternions) $\mathbf{q} \equiv (q_1, q_2, q_3, q_4)$ describe the orientation of the object [6]. Similar to the matrix of rotation with the three Euler-angles $\mathbf{R} \equiv (\theta, \phi, \psi)$ a rotational matrix $\mathbf{A}(\mathbf{q})$ depending on the quaternion can then be defined to transform any vector from the laboratory frame $\mathbf{v}_{lf}$ into the quaternion description $\mathbf{V}_q = \mathbf{A}(\mathbf{q})\mathbf{v}_{lf}$ and with the transposed of the rotational matrix $\mathbf{A}^T$ back to the laboratory frame. In contrast to using Euler-angles, the quaternion approach leads to a singularity-free dynamics and avoids the calculation of trigonometric functions. According to the integration scheme of the FP, a Velocity-Verlet algorithm proposed by Omelyan [4] is used.

2. Performance, Parallelisation and Code Structure

The strategy for spanning multiple length- and timescales in a simulation is to run them on larger PC cluster and supercomputers with 100’s to 1000’s of processors. Our simulation code has been parallelised with Message-Passing Interface (MPI) employing a domain decomposition (see Fig. 1 a)). The performance can significantly be enhanced by a dynamic load balancing by weighting the actual workload on each processor. It ensures that particles are distributed evenly among all processors according to the predicted workload (see Fig. 1 b)). The scaling on the NEC Xeon EM64T Cluster was tested with a simple fluid containing 10^6 FP and a bead suspension with additional 2100 beads giving a 5 % volume concentration (v/v) (see Fig. 2 a). Each bead consists of 19 FP with the same density compared to the surrounding fluid and is propagated by the quaternion algorithm. A smaller simulation with 4.5 10^5 FP was performed on a small Dual-Core Opteron Cluster with 1050 beads also leading to a 5 % (v/v) (see Fig. 2 b)). Both cases show for increasing number of processors at constant number of FP a super linear speed-up, indicating that field indexing and memory access effects are playing a negative role on the performance on single processor systems.

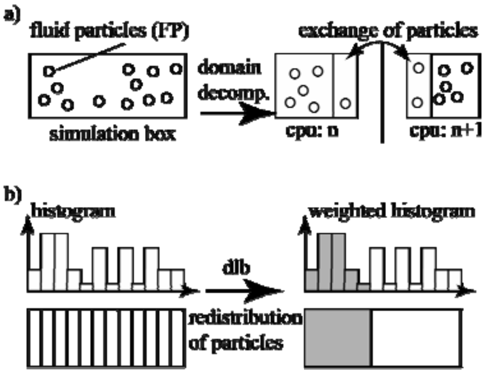

Figure 1: Parallelisation and performance (a) domain decomposition with MPI (b) dynamic loadbalancing (dlb) distribute the particles according to the predicted workload on the CPUs.

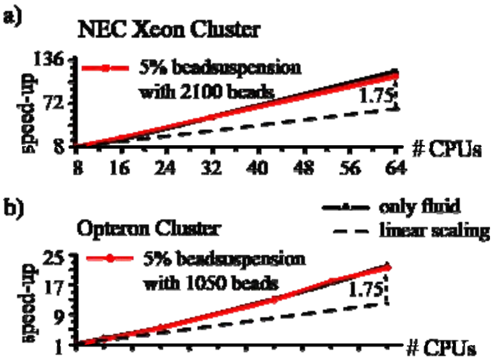

Figure 2: Speed-up of the simulation code with a fluid and a bead suspension on (a) NEC Xeon EM64T cluster with max. 400 Xeon CPUs @ 3.2GHz (b) Dual-Core Opteron cluster (6 CPUs @ 2.2GHz).

3. Aggregation of Bead

The aggregation of polystyrene micro-beads with a diameter of 150 µm is simulated and experimentally validated in a milled microfluidic structure (see Fig. 3). In the experiments as well as in the simulations beads are initially put in a collecting chamber (not shown here) and are flowing through the inlet channel into the aggregation chamber. Each simulation for a predefined number of aggregating beads takes about 10 hours for ~2.5 10^5 FP on an Opteron Cluster calculated with 8 dual core CPUs. The rhomboidal aggregation part of the chamber can hold a maximum of 360 hexagonally accumulated beads with 177 FP per bead (see Fig. 3). Capture of beads at walls and corners induces imperfections in the layering that are also present in the simulations (circle in Fig. 3) in particular the disturbance of the hexagonal order at round corners. The Peclet number for the simulated structure is calculated to $\mathrm{Pe} = \rho \bar{v} L / D_B \approx 5200 >> 1$ such that the residual stochastic motion is negligible (mean fluid velocity $\bar{v} = 0.17$, length of the aggregation chamber $L = 97$) with a diffusion constant of the beads according to the Stokes-Einstein relation of $D_B = 0.019$. All microfluidic geometries are generated with commercial CAD tools, subsequently meshed and then imported into the simulation where the mesh nodes are translated into particle position.

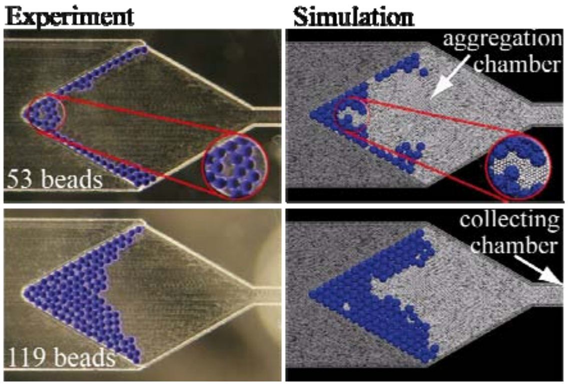

Figure 3: Aggregation of 53 and 119 polystyrene micro-beads (experiments left, simulations right).

Conclusion

We successfully presented the simulation of complex fluids in confined geometries at HPC with an extendable simulation code. The simulations with Peclet numbers greater than one are a good hydrodynamic representation of the system where convection dominates over diffusion showing that the simulation represents a systems at large time and length scales. With a change in parameterisation of the simulation the Peclet number can easily be reduced and then representing nano-scaled systems at small time and length scales.

Acknowledgements

The support of the Landesstiftung Baden-Württemberg (HPC-Project) is gratefully acknowledged.

References

[1] P. J. Hoogerbrugge and J. M. V. A. Koelman, *Simulating Microscopic Hydrodynamic Phenomena with Dissipative Particle Dynamics*, Europhysics Letters, vol. 19, no. 3, pp. 155-160, (1992).

[2] P. B. Warren, *Vapor-liquid coexistence in many-body dissipative particle dynamics*, Physical Review e, vol. 68, no. 6, (2003).

[3] D. J. Evans, *Representation of Orientation Space*, Molecular Physics, vol. 34, no. 2, pp. 317-325, 1977, D. J. Evans and S. Murad, *Singularity Free Algorithm for Molecular-Dynamics Simulation of Rigid Polyatomics*, Molecular Physics, vol. 34, no. 2, pp. 327-331, (1977).

[4] I. P. Omelyan, *Algorithm for numerical integration of the rigid-body equations of motion*, Physical Review e, vol. 58, no. 1, pp. 1169-1172, (1998).

[5] M. Grumann, M. Dobmeier, P. Schippers, T. Brenner, C. Kuhn, M. Fritsche, R. Zengerle, and J. Ducrée, *Aggregation of bead-monolayers in flat microfluidic chambers simulation by the model of porous media*, Lab on A Chip, vol. 4, no. 3, pp. 209-213, (2004).

[6] P. Espanol and P. B. Warren, *Statistical-Mechanics of Dissipative Particle Dynamics*, Europhysics Letters, vol. 30, no. 4, pp. 191-196, (1995).

Relaxed Potentials and Microstructure Evolution

Klaus Hackl[1]

[1]**Institute of Mechanics, Ruhr University of Bochum, 44780 Bochum, Germany,**
E-mail: klaus.hackl@rub.de

ABSTRACT

We consider microstructures which are not inherent to the material but occur as a result of deformation or other physical processes. Examples are martensitic twin-structures or dislocation walls in single crystals and microcrack-fields in solids. An interesting feature of all those microstructures is, that they tend to form similar spatial patterns, hinting at a universal underlying mechanism. For purely elastic materials this mechanism has been identified as minimization of global energy. For non-quasiconvex potentials the minimizers are not anymore continuous deformation fields, but small-scale fluctuations related to probability distributions of deformation gradients, so-called Young-measures. These small scale fluctuations correspond exactly to the observed material microstructures. The particular features of those, like orientation or volume-ratios, can now be calculated via so-called relaxed potentials. We develop a variational framework which allows to extend these concepts to inelastic materials. Central to this framework will be a Lagrange functional consisting of the sum of elastic power and dissipation due to change of internal state of the material. We will be able to obtain time-evolution equations for the probability-distributions mentioned above. Possible applications are to crystal plasticity, damage mechanics and phase-transformations.

1 Introduction

We investigate inelastic materials described by so-called internal or history- variables. Examples include elastoplastic but also damaged materials or those undergoing phase-transformations. By considering associated potentials in a time-incremental setting it is possible to model the onset of the formation of microstructures but not their subsequent evolution, [1, 2, 3, 4, 5]. Here, some general ideas will be presented on how this problem could be treated.

2 Minimum Principles

In an isothermal setting the state of a general inelastic material will be defined by its deformation gradient $\boldsymbol{F} = \nabla\,\boldsymbol{\phi}$ an a collection of internal variables: $\boldsymbol{K}$. Denoting the specific Helmholtz free energy by $\Psi(\boldsymbol{F}, \boldsymbol{K})$ we introduce thermodynamically conjugate stresses by $\boldsymbol{P} = \frac{\partial\Psi}{\partial\boldsymbol{F}}$, $\boldsymbol{Q} = -\frac{\partial\Psi}{\partial\boldsymbol{K}}$. The evolution of $\boldsymbol{K}$ is then governed either by a so-called inelastic potential $J(\boldsymbol{K}, \boldsymbol{Q})$ or its Legendre-transform, the dissipation functional: $\Delta(\boldsymbol{K}, \dot{\boldsymbol{K}}) = \sup\big\{\dot{\boldsymbol{K}} : \boldsymbol{Q} - J(\boldsymbol{K}, \boldsymbol{Q})\,\big|\,\boldsymbol{Q}\big\}$. The evolution equations are then given in the two equivalent forms

$$\dot{\boldsymbol{K}} \in \frac{\partial J}{\partial \boldsymbol{Q}}, \qquad \boldsymbol{Q} \in \frac{\partial \Delta}{\partial \dot{\boldsymbol{K}}}. \tag{1}$$

The entire evolution problen can now be described in terms of two minimum principles, where we follow ideas presented in [6, 7, 5]. Considering the Gibbs free energy of the entire body $\mathcal{I}(t, \boldsymbol{\phi}, \boldsymbol{K}) = \int_\Omega \Psi(\nabla\boldsymbol{\phi}, \boldsymbol{K})\,\mathrm{d}V - \ell(t, \boldsymbol{\phi})$ the deformation is given by the principle of minimum potential energy:

$$\boldsymbol{\phi} = \arg\min \left\{ \mathcal{I}(t, \boldsymbol{\phi}, \boldsymbol{K}) \;\middle|\; \boldsymbol{\phi} = \boldsymbol{\phi}_0 \text{ on } \Gamma_\varphi \right\}. \tag{2}$$

Here Ω is the material body, Γ_φ a subset of its boundary and $\ell(t, \boldsymbol{\phi})$ the potential of external forces. On the other hand introducing the Lagrange functional $\mathcal{L}(\boldsymbol{\phi}, \boldsymbol{K}, \dot{\boldsymbol{K}}) = \dfrac{d}{dt}\,\Psi(\nabla\boldsymbol{\phi}, \boldsymbol{K}) + \Delta(\boldsymbol{K}, \dot{\boldsymbol{K}})$ we can write the evolution equation (1) in the form

$$\dot{\boldsymbol{K}} = \arg\min \left\{ \mathcal{L}(\boldsymbol{\phi}, \boldsymbol{K}, \dot{\boldsymbol{K}}) \;\middle|\; \dot{\boldsymbol{K}} \right\}. \tag{3}$$

For rate-independent materials the principle (3) enables us to account for instantanious change of the value of $\boldsymbol{K}$, because it can be integrated to yield the balance law

$$\Psi(\nabla\boldsymbol{\phi}, \boldsymbol{K}_1) - \Psi(\nabla\boldsymbol{\phi}, \boldsymbol{K}_0) = -D(\boldsymbol{K}_0, \boldsymbol{K}_1), \tag{4}$$

where

$$D(\boldsymbol{K}_0, \boldsymbol{K}_1) = \inf \left\{ \int_0^1 \Delta(\boldsymbol{K}(s), \dot{\boldsymbol{K}}(s))\,\mathrm{d}s \;\middle|\; \boldsymbol{K}(0) = \boldsymbol{K}_0, \boldsymbol{K}(1) = \boldsymbol{K}_1 \right\} \tag{5}$$

is called dissipation-distance, [7]. When applied to a finite time-increment $[t_n, t_{n+1}]$ equation (4) gives rise to an approximate formulation, where $\boldsymbol{\phi}_{n+1}$ and $\boldsymbol{K}_{n+1}$ at time t_{n+1} are determined for given loading at time t_{n+1} and value of the internal variables $\boldsymbol{K}_n$ at time t_n via the following principle, [6, 7]:

$$\{\boldsymbol{\phi}_{n+1}, \boldsymbol{K}_{n+1}\} = \arg\min \left\{ \int_\Omega \{\Psi(\nabla\boldsymbol{\phi}, \boldsymbol{K}) + D(\boldsymbol{K}_n, \boldsymbol{K})\}\,\mathrm{d}V - \ell(t_{n+1}, \boldsymbol{\phi}) \;\middle|\; \boldsymbol{\phi}, \boldsymbol{K} \right\}. \tag{6}$$

3 Young-Measures

Carrying out the minimization with respect to $\boldsymbol{K}$ in (6) beforehand gives the so-called condensed energy $\Psi^{\mathrm{cond}}_{\boldsymbol{K}_n}(\boldsymbol{F}) = \inf \left\{ \Psi(\boldsymbol{F}, \boldsymbol{K}) + D(\boldsymbol{K}_n, \boldsymbol{K}) \;\middle|\; \boldsymbol{K} \right\}$ which has been used in the literature to calulate the onset of microstructures, [1, 2, 3, 4, 5]. This approach, however, is not suitable to describe the evolution of microstructures, because then the internal variables are already microstructured at the beginning of the time-increment as a result of a relaxation process in the preceeding time-increment. Or they are microstructured through the whole course of continuous evolution. Hence, they have to be given in the form of so-called Young–measures. We are going to give some concepts now, how such a formulation might be derived.

Young-measures are probability–distributions $\lambda_{\boldsymbol{F}} \geq 0$ given for example for the deformation-gradient, i.e. on $\mathsf{GL}(d)$, and dependent on the material point. Thus they have the following properties: $\int \lambda_{\boldsymbol{F}}\,\mathrm{d}\boldsymbol{F} = 1$, $\int \lambda_{\bar{\boldsymbol{F}}}\,\bar{\boldsymbol{F}}\,\mathrm{d}\bar{\boldsymbol{F}} = \boldsymbol{F}$. Moreover in the case of the deformation-gradient, the probability-distribution has to be compatible, i.e. realizable by a deformation field $\boldsymbol{\phi}$. This means that $\frac{1}{\Omega_{\mathrm{rep}}}\int_{\Omega_{\mathrm{rep}}}\Psi(\nabla\boldsymbol{\phi})\,\mathrm{d}V = \int_{\mathsf{GL}(d)}\lambda_{\bar{\boldsymbol{F}}}\Psi(\bar{\boldsymbol{F}})\,\mathrm{d}\bar{\boldsymbol{F}}$ has to hold for all quasiconvex potentials Ψ. In this case we call $\lambda_{\boldsymbol{F}} \in \mathsf{GYM}$ a gradient Young-measure.

It is now, at least in principle, possible to define a relaxed energy and dissipation functional via cross-quasiconvexication as

$$\begin{aligned}\Psi^{\mathrm{rel}}(\boldsymbol{F},\lambda_{\boldsymbol{K}}) = \inf\Big\{ &\int \Lambda_{\bar{\boldsymbol{F}},\bar{\boldsymbol{K}}}\Psi(\bar{\boldsymbol{F}},\bar{\boldsymbol{K}})\,\mathrm{d}\bar{\boldsymbol{K}}\,\mathrm{d}\bar{\boldsymbol{F}} \;\Big|\; \int \Lambda_{\bar{\boldsymbol{F}},\bar{\boldsymbol{K}}}\,\mathrm{d}\bar{\boldsymbol{K}}\,\mathrm{d}\bar{\boldsymbol{F}} = 1,\\ &\int \Lambda_{\bar{\boldsymbol{F}},\bar{\boldsymbol{K}}}\,\mathrm{d}\bar{\boldsymbol{K}} \in \mathsf{GYM}, \int \Lambda_{\bar{\boldsymbol{F}},\boldsymbol{K}}\,\mathrm{d}\bar{\boldsymbol{F}} = \lambda_{\boldsymbol{K}}, \int \Lambda_{\bar{\boldsymbol{F}},\bar{\boldsymbol{K}}}\bar{\boldsymbol{F}}\,\mathrm{d}\bar{\boldsymbol{K}}\,\mathrm{d}\bar{\boldsymbol{F}} = \boldsymbol{F}\Big\}, \end{aligned} \tag{7}$$

$$\begin{aligned}\Delta^*(\dot{\lambda}_{\boldsymbol{K}}) = \inf\Big\{ &\int \Lambda_{\boldsymbol{K}_0,\boldsymbol{K}_1}D(\boldsymbol{K}_0,\boldsymbol{K}_1)\,\mathrm{d}\boldsymbol{K}_0\,\mathrm{d}\boldsymbol{K}_1 \;\Big|\\ &\int \Lambda_{\boldsymbol{K}_0,\boldsymbol{K}_1}\,\mathrm{d}\boldsymbol{K}_0\,\mathrm{d}\boldsymbol{K}_1 = 1, \int \Lambda_{\boldsymbol{K}_0,\boldsymbol{K}_1}\,\mathrm{d}\boldsymbol{K}_0 = \dot{\lambda}_{\boldsymbol{K}}, \int \Lambda_{\boldsymbol{K}_0,\boldsymbol{K}_1}\,\mathrm{d}\boldsymbol{K}_1 = -\dot{\lambda}_{\boldsymbol{K}}\Big\}. \end{aligned} \tag{8}$$

Related concepts have already been introduced in somewhat different settings in [3].

4 Evolution Equations

With these definitions we recover the original principles (2) and (3), with the only difference that the internal variables $\boldsymbol{K}$ have been replaced by the Young-measures $\lambda_{\boldsymbol{K}}$. However, we have to take care of the facts that $\lambda_{\boldsymbol{K}} \geq 0$ and $\int \lambda_{\boldsymbol{K}}\,\mathrm{d}\boldsymbol{K} = 1$. Introducing this constraints via Langrange- and Kuhn-Tucker-multipliers, respectively, the Lagrange functional in (3) assumes the form

$$\mathcal{L}(\boldsymbol{\phi},\lambda_{\boldsymbol{K}},\dot{\lambda}_{\boldsymbol{K}}) = \frac{d}{dt}\,\Psi^{\mathrm{rel}}(\nabla\boldsymbol{\phi},\lambda_{\boldsymbol{K}}) + \Delta^*(\dot{\lambda}_{\boldsymbol{K}}) + \alpha\int \dot{\lambda}_{\boldsymbol{K}}\,\mathrm{d}\boldsymbol{K} - \int \beta_{\boldsymbol{K}}\dot{\lambda}_{\boldsymbol{K}}\,\mathrm{d}\boldsymbol{K}, \tag{9}$$

and we get the Kuhn-Tucker conditions

$$\dot{\lambda}_{\boldsymbol{K}} \geq 0, \quad \beta_{\boldsymbol{K}} \geq 0, \quad \dot{\lambda}_{\boldsymbol{K}}\beta_{\boldsymbol{K}} = 0. \tag{10}$$

One main advantage of the present formulation is the fact, that it is possible to arrive at evolution equations for $\lambda_{\boldsymbol{K}}$. Thus we can avoid the solution of global minimization problems, as was required when calculating the onset of microstructions via the condensed energy, [1]. For this purpose we define thermodynamically conjugate forces: $q_{\boldsymbol{K}} = -\frac{\partial\Psi^{\mathrm{rel}}}{\partial\lambda_{\boldsymbol{K}}}$. Because of the two constraints mentioned above the evolution problem inherits an active set structure and a deviatoric structure. Therefore we introduce the active set $\mathcal{A} = \big\{\, \boldsymbol{K} \;\big|\; \lambda_{\boldsymbol{K}} > 0 \,\big\}$ and the active deviator $\mathrm{dev}_{\mathcal{A}}\, x_{\boldsymbol{K}} = x_{\boldsymbol{K}} - \big(\int_{\mathcal{A}} x_{\boldsymbol{K}}\,\mathrm{d}\boldsymbol{K}\big)\,\mathbf{1}$ as well as the restriction: $x_{\mathcal{A}} = (x_{\boldsymbol{K}})_{\boldsymbol{K}\in\mathcal{A}}$. We can once again define an inelastic potential via Legendre-tranform by

$$J^*(q_{\boldsymbol{K}}) = \inf\Big\{ \int \dot{\lambda}_{\boldsymbol{K}}q_{\boldsymbol{K}}\,\mathrm{d}\boldsymbol{K} - \Delta^*(\dot{\lambda}_{\boldsymbol{K}}) \;\Big|\; \dot{\lambda}_{\boldsymbol{K}} \Big\} = \chi(\Phi(q_{\boldsymbol{K}})), \tag{11}$$

which because of the rate-independence of the problem can be written in terms of the characteristic function χ of a yield-function Φ. With this notation we obtain the desired evolution equation

$$\dot{\lambda}_{\mathcal{A}} \in \mathrm{dev}_{\mathcal{A}}\, \frac{\partial\Phi}{\partial q_{\boldsymbol{K}}}\bigg|_{\mathcal{A}} \tag{12}$$

along with the consistency condition

$$\frac{\partial\Delta^*}{\partial\dot{\lambda}_{\boldsymbol{K}}} - \operatorname{dev}_{\mathcal{A}} q_{\boldsymbol{K}} \geq 0 \quad \text{for} \quad \boldsymbol{K} \notin \mathcal{A}. \tag{13}$$

Here the inequality (13) plays the role of a switch determining when an inactive constraint becomes active again.

5 Polycrystalline Shape-Memory-Alloys

We will now apply the theory developed before to polycrystalline shape-memory-alloys, Further details concerning the model derived can be found in [8]. Our aim is to describe the behaviour of polycrystalline shape–memory–alloys by considering the orientation–distribution of the various martensite–variants. We will assume that within the polycrystal all desired orientations of transformation–strain are equally available for the material in order to minimize energy. This way we will be able to predict the internal reorientation of martensite. In order to capture hysteresis effects we will assume that change in the orientation–distribution is accompanied by dissipation.

The formulation presented allows to model all relevant features of shape–memory–alloys such as pseudoelasticity and the shape–memory effect in an effective way. Moreover the orientation–distribution of martensite–variants within the polycrystal is obtained which is an important information that can be used to validate the model. We will close this report giving different results of numerical simulations .

A spatially varying energetic description of microstructure formation in shape–memory alloys was first given in [9] and extended to include inelasticity and dissipative effects in [6]. A thermodynamical framework in the spirit of the present paper was given in [10].

6 Orientation Distribution and Relaxed Energy

Our model is based on the fundamental assumption, that looking at a sufficiently large representative volume element within a polycrystalline shape–memory–alloy, there can be found crystallites of arbitrary orientation. This fact allows the polycrystalline material to accomodate any macroscopic deformation by producing any suitable orientation–distribution of martensite–variants. Since we are dealing with transformation–strains of more than 10% we have to work with a materially frame–indifferent constitutive model which we will achieve by a formulation within a Lagrangian framework. In order to capture moderately large strains as required here, we will use the material Hencky–tensor $\boldsymbol{H} = \log \boldsymbol{U}$ as fundamental strain–measure. Here $\boldsymbol{U} = (\boldsymbol{F}^{\mathrm{T}}\boldsymbol{F})^{1/2}$ denotes the material (right) stretch–tensor and $\boldsymbol{F}$ the deformation-gradient.

Let now $\boldsymbol{U}_*$ be the Bain–stretch–tensor, i.e. the transformation–stretch in principal coordinates and $\boldsymbol{H}_* = \log \boldsymbol{U}_*$ the corresponding Hencky–tensor. Let the principal stretches be u_1, u_2, u_3 with Hencky–strains $h_i = \log u_i$, then $\boldsymbol{U}_*$ and $\boldsymbol{H}_*$ respectively are diagonal matricies with entries u_i and h_i.

We assume that our material has N different orientations $\boldsymbol{R}_i \in \mathrm{SO}_3$ of martensite–variants available, where SO_3 denotes the special orthogonal group consisting of all rotation tensors. Of course in the limit N should become infinite. Here, however, we will assume N to be large but finite for two reasons. The mathematical exposition to follow becomes more concise this way and any numerical implementation has to resort to a finite N anyway. But this procedure does not constitute a fundamental limitation of the approach. Now an orientation–distribution is given by volume ratios λ_i corresponding to orientations $\boldsymbol{R}_i$. It has to hold

$$\lambda_i \geq 0, \qquad \sum_{i=1}^{N} \lambda_i = 1. \tag{14}$$

The transformation–strain corresponding to orientation $\boldsymbol{R}_i$ is then given by

$$\boldsymbol{K}_i = \boldsymbol{R}_i^{\mathrm{T}} \boldsymbol{H}_* \boldsymbol{R}_i. \tag{15}$$

In addition we will denote by $\boldsymbol{K}_0 = \boldsymbol{0}$ the zero transformation–strain of the austenitic phase. We will use an elastic energy which is linear and isotropic with respect to the Hencky–strains. Let $\boldsymbol{H}_i = \log \boldsymbol{U}_i$ be the microscopic Hencky–strain exhibited by crystallites in orientation $\boldsymbol{R}_i$, then the specific energy of such crystallites is given by

$$\Psi(\boldsymbol{H}_i, \boldsymbol{K}_i) = \frac{1}{2}(\boldsymbol{H}_i - \boldsymbol{K}_i) : \mathcal{A} : (\boldsymbol{H}_i - \boldsymbol{K}_i) + c_i, \tag{16}$$

where $\mathcal{A}$ denotes the fourth–order tensor of elastic stiffnesses, given by $\mathcal{A}_{ijkl} = \Lambda \delta_{ij}\delta_{kl} + 2\mu\delta_{ik}\delta_{jl}$, and ":" means contraction with respect to two indices. The chemical energy is given by c_i, i.e. we have $c_i = c_{\mathrm{A}}$ for austenite and $c_i = c_{\mathrm{M}}$ for martensite. Isotropy of the energy is of course not given in a strict sense because there is a correspondence between crystal orientation and orientation of the transformation–strain. But we will once again assume that there are enough crystallites available close to a given orientation to effectively average out any anisotropy which might occur.

The volume average of the various Hencky–strains is supposed to give the macroscopically observed Hencky–strain $\boldsymbol{H} = \log \boldsymbol{U}$, resulting in

$$\sum_{i=1}^{N} \lambda_i \boldsymbol{H}_i = \boldsymbol{H}. \tag{17}$$

For a given orientation–distribution $\boldsymbol{\lambda} = (\lambda_i)$ we postulate the total energy to be minimized by the material with respect to the different Hencky–strains. This leads to a so–called relaxed energy defined by

$$\Psi^{\mathrm{rel}}(\boldsymbol{H}, \boldsymbol{\lambda}) = \inf \Big\{ \sum_{i=1}^{N} \lambda_i \Psi(\boldsymbol{H}_i, \boldsymbol{K}_i) \,\Big|\, \boldsymbol{H}_i, \sum_{i=1}^{N} \lambda_i \boldsymbol{H}_i = \boldsymbol{H} \Big\}. \tag{18}$$

This procedure corresponds to relaxation by convexification, which actually is a very crude way to relax potentials. For more sophisticated methods and their mechanical interpretation see [11, 12]. Models in a similiar spirit that the one presented here can also be found in [13, 14]. The minimization in 18 can be carried out in a straightforward way and yields

$$\boldsymbol{H}_i = \boldsymbol{H} + \boldsymbol{K}_i - \sum_{j=1}^{N} \lambda_j \boldsymbol{K}_j, \tag{19}$$

and

$$\Psi^{\mathrm{rel}}(\boldsymbol{H}, \boldsymbol{\lambda}) = \frac{1}{2}(\boldsymbol{H} - \boldsymbol{K}_{\mathsf{eff}}) : \mathcal{A} : (\boldsymbol{H}_i - \boldsymbol{K}_{\mathsf{eff}}) + c_{\mathsf{eff}}, \tag{20}$$

where

$$\boldsymbol{K}_{\mathsf{eff}} = \sum_{i=1}^{N} \lambda_i \boldsymbol{K}_i, \quad c_{\mathsf{eff}} = \sum_{i=1}^{N} \lambda_i c_i, \tag{21}$$

denotes effective transformation–strain and chemical energy.

7 Time Evolution

In order to close our model we would have to calculate the relaxed dissipation functional.$\boldsymbol{\lambda}$. Instead, we will directly choose it to be given as

$$\Delta^*(\dot{\boldsymbol{\lambda}}) = r|\dot{\boldsymbol{\lambda}}|, \tag{22}$$

where "$|\cdot|$" denotes the usual Euclidian norm of a vector. This choise is quite plausible given the fact that Δ^* should be isotropic in $\dot{\boldsymbol{\lambda}}$. The thermodynamically conjugate force to $\dot{\boldsymbol{\lambda}}$ is now given by

$$q_i = -\frac{\partial \Psi^{\text{rel}}}{\partial \lambda_i} = \boldsymbol{K}_i : \mathcal{A} : (\boldsymbol{H} - \sum_{j=1}^{N} \lambda_j \boldsymbol{K}_j) - c_i. \tag{23}$$

Then introducing the "yield–function" $\Phi(\boldsymbol{q}) = |\ \mathrm{dev}_{\mathcal{A}}\, \boldsymbol{q}_{\mathcal{A}}| - r$ we have

$$J(\boldsymbol{q}) = \left\{ \begin{array}{lll} 0 & \text{for} & \Phi(\boldsymbol{q}) < 0 \\ \infty & \text{else} & \end{array} \right. . \tag{24}$$

With these notations the evolution law 12 along with the constraints 14 can be expressed in the form

$$\dot{\boldsymbol{\lambda}}_{\mathcal{A}} = \rho\ \mathrm{dev}_{\mathcal{A}}\ \boldsymbol{q}_{\mathcal{A}}, \tag{25}$$

along the Kuhn–Tucker condition

$$\rho \geq 0, \quad \Phi \leq 0, \quad \rho\, \Phi = 0, \tag{26}$$

and the consistency condition

$$(\mathrm{dev}_{\mathcal{A}}\, \boldsymbol{q})_i \leq 0 \quad \text{for} \quad i \notin \mathcal{A}. \tag{27}$$

The evolution equation 25 along with the conditions 26 and 27 can be integrated in a stable manner using algorithms developed in the context of finite–elastoplasticity. We do this employing an operator–split algorithm as introduced in [15].

8 Examples

As numerical example we investigate a shear–test, i.e. we apply a deformation gradient of the form $\boldsymbol{F} = \begin{pmatrix} 1 & \gamma_{12} & 0 \\ 0 & 1 & 0 \\ 0 & 0 & 1 \end{pmatrix}$.

In figure 1 hysteresis due to the shape–memory–effect is shown. This means we have $c_{\mathrm{M}} < c_{\mathrm{A}}$ and we start with equally distributed martensite. We display Cauchy shear–stress σ_{12} as a function of γ_{12} for cyclic loading. For the points indicated the orientation–distribution λ_i for $i = 1, \ldots, N$ (i.e. for martensite only) is plotted as a function of φ_i. There is no austenite present at any time. We see that reorientation of martensite takes place in a highly complex way.

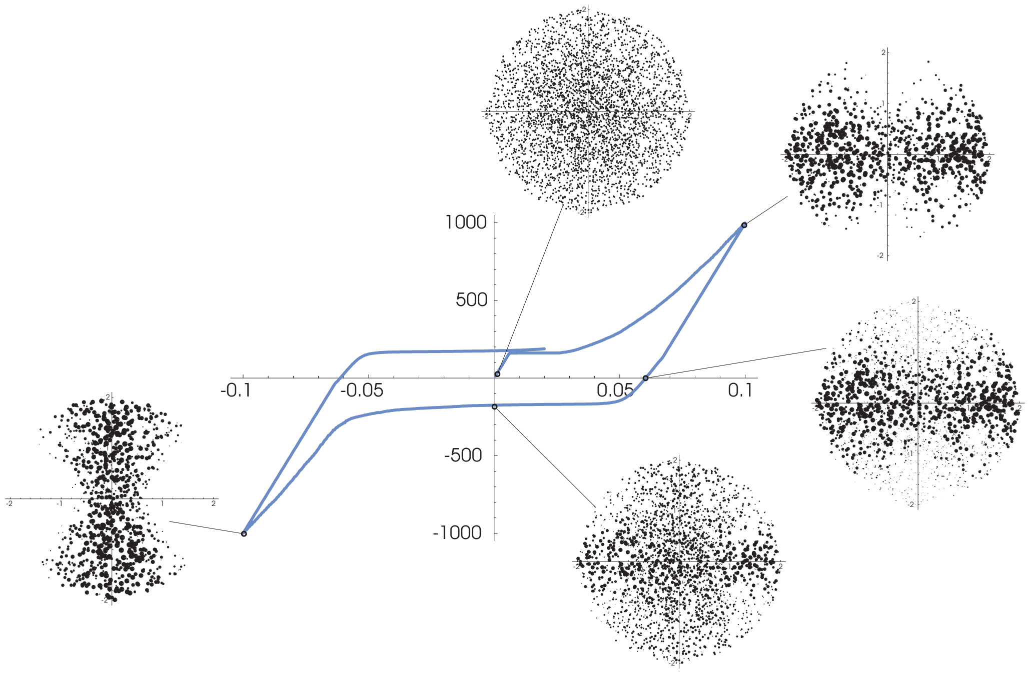

Figure 1: Pseudoplastic hysteresis

In figure 2 we model pseudoelastic behaviour. Now we have $c_A < c_M$. We start with pure austenite. The same quantities as in figure 1 are depicted. Stress–driven phase–transformation between austenite and martensite as well as reorientation of martensite takes place now. Contrary to the shape–memory–effect the orientation of martensite stays very localised.

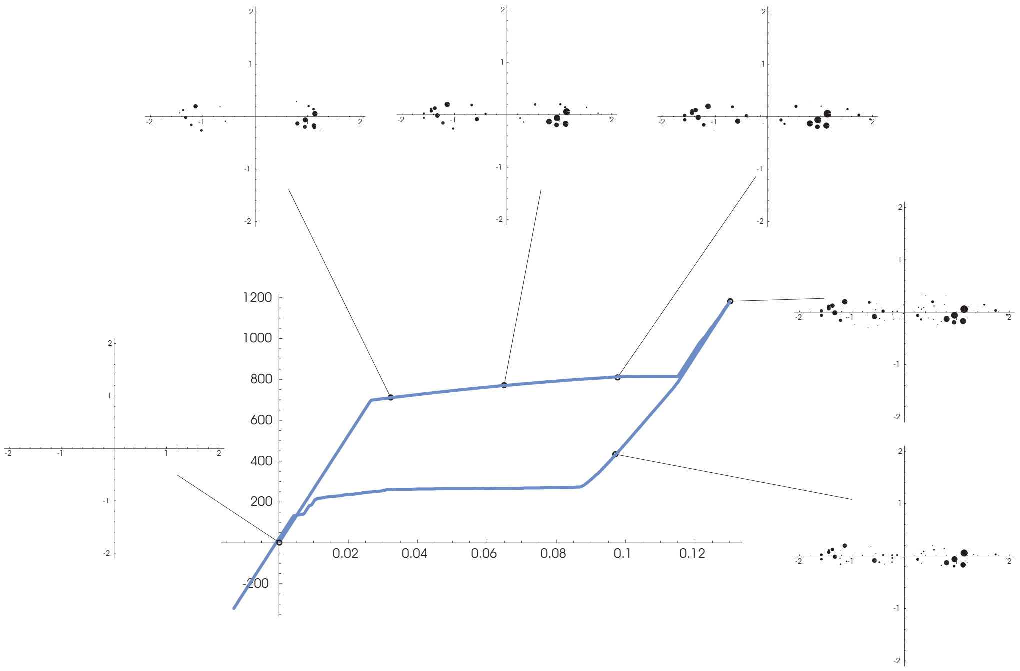

Figure 2: Pseudoelastic behaviour

9 Conclusion

We have shown how the evolution of microstructures can be described efficiently by employing relaxation of nonconvex potentials. The approach is universally applicable to any kind of material exhibiting formation of microstructures. Relaxation leads by definition to well-posed problems with regular solutions. Finite element implementations return mesh–independent results. Finally the approach opens up a new perspective on continuum mechanics. In the future one main goal will be the derivation of better relaxed energies and dissipation-functionals. Also experimatal verification of the models will be an important issue.

References

[1] Bartels S., Carstensen C., Hackl K. and Hoppe U., Effective relaxation for microstructures simulations: algorithms and applications. *Comp. Meth. Appl. Meth. Eng.*, **193, No. 48-51**, (2004), 5143–5175.

[2] Conti S. and Theil F., Single-Slip Elastoplastic Microstructures. *Arch. Rat. Mech. Anal.*, **178**, (2005), 125–148.

[3] Mielke A., Deriving new evolution equations for microstructures via relaxation of variational incremental problems. *Comp. Meth. Appl. Meth. Eng.*, **193**, (2004), 5095–5127.

[4] Lambrecht M., Miehe C. and Dettmar J., Energy Relaxation of Non-Convex Incremental Stress Potentials in a Strain-Softening Elastic-Plastic Bar. *Int. J. Solids Struct.*, **40**, (2003), 1369–1391.

[5] Ortiz M. and Repetto E.A., Nonconvex energy minimisation and dislocation in ductile single crystals. *J. Mech. Phys. Solids*, **47**, (1999), 397–462.

[6] Carstensen C., Hackl K. and Mielke A., Nonconvex potentials and microstructures in finite-strain plasticity. *Proc. R. Soc. Lond. A*, **458, 2018**, (2002), 299–317.

[7] Mielke A., Finite elastoplasticity, Lie groups and geodesics on SL(d). In *Geometry, Dynamics, and Mechanics* eds. Newton P., Weinstein A., Holmes P.), Springer–Verlag, (2002), 61–90.

[8] Hackl K., Schmidt-Baldassari M. and Zhang W., A micromechanical model for polycrystalline shape-memory alloys. *Materials Science and Engineering A*, **378**, (2003), 503–506.

[9] Ball J.M. and James R.D., Fine phase mixtures as minimizer of energy. *Arch. Rational Mech. Analysis*, **100**, (1987), 13–52.

[10] Huo Y. and Müller I., Nonequilibrium Thermodynamics of Pseudoelasticity. *Continuum Mech. Thermodyn.*, **5**, (1993), 163–204.

[11] Hackl K. and Hoppe U., On the Calculation of Microstructures for Inelastic Materials Using Relaxed Energies. In: *IUTAM Symposium on Computational Mechanics of Solid Materials at Large Strains* (eds. Miehe C.), Kluwer, (2003), 77–86.

[12] Roubíček T., Relaxation in Optimization Theory and Variational Calculus, De Gruyter, (1997).

[13] Carstensen C. and Plecháč P., Numerical analysis of a relaxed variational model of hysteresis in two-phase solids. *M2AN Math. Model. Numer. Anal.*, **35**, (2001), 865–878.

[14] Mielke A., Theil F. and Levitas V.I., A variational formulation of rateindependent phase transformations using an extremum principle. *Arch. Rat. Mech. Anal.*, **162**, (2002), 137–177.

[15] Hackl K. and Schmidt–Baldassari M., Time integration algorithms for evolution equations in finite strain plasticity. In: *Trends in Computational Structural Mechanics* (eds. Wall W.A., Bletzinger K.U., Schweizerhof K.), CIMNE, Barcelona, (2001), 128–139.

Backward error analysis of multiscale symplectic integrators and propagators.

Christopher R. Sweet[1], Jesús A. Izaguirre[2]
Department of Computer Science and Engineering
Notre Dame, IN 46556, USA.
[1] csweet1@nd.edu [2] izaguirr@nd.edu

Abstract

Symplectic integrators are used in molecular dynamics simulations for their excellent long term behavior, due to the existence of the associated shadow Hamiltonian. Improvements in the efficiency of multiscale simulations can be obtained by the introduction of symplectic multiple timestep methods such as Verlet-I/r-RESPA, but these schemes generally require switches to separate the forces efficiently. The authors derive the shadow Hamiltonian for this method, using backward error analysis, and show that it is dependent on the smoothness of these switches.

1 Introduction

In this paper we consider both the backward error analysis for Verlet-I/r-RESPA and the effect of the addition of switching functions to split the potential energy. It had been previously noted [1] that the lack of smoothness in a C^1 continuous piecewise potential had a "deleterious effect on the conservation of interpolated shadow Hamiltonians". We expand upon this result and extend it to switched potentials and the backward error analysis of the Verlet-I/r-RESPA integrator.

2 Shadow Hamiltonian for the Verlet-I integrator

Given that a shadow Hamiltonian (for which the numerical results are the exact solution), $\hat{H}$, exists it can be calculated using either the truncated or interpolated methods. The truncated method, which can be found in [2], is

$$\hat{H} = H + \delta t \hat{H}^{(1)} + \delta t^2 \hat{H}^{(2)} + \cdots, \tag{1}$$

where H is the original Hamiltonian and $\hat{H}^{(i)}$ are the additional terms of the modified Hamiltonian which are calculated by the backward error analysis [3] for timestep δt. In general the series does not converge for non-linear systems and is truncated at some point. The Verlet-I multiple timestep method, for a total time-step of $r\delta t$ where r is the ratio between the fast and slow steps, has the 4^{th} order truncated shadow Hamiltonian

$$\begin{aligned}\hat{H}_{[4T]} \;=\; & H + \frac{\delta t^2}{24}\Big[2\left(\mathbf{U}_f'\right)^{\mathrm{T}}\mathbf{M}^{-1}\mathbf{U}_f' - r^2\left(\mathbf{U}_s'\right)^{\mathrm{T}}\mathbf{M}^{-1}\mathbf{U}_s' - 2r^2\left(\mathbf{U}_f'\right)^{\mathrm{T}}\mathbf{M}^{-1}\mathbf{U}_s' \\ & - \mathbf{p}^{\mathrm{T}}\mathbf{M}^{-1}\mathbf{U}_f''\,\mathbf{M}^{-1}\mathbf{p} + 2r^2\mathbf{p}^{\mathrm{T}}\mathbf{M}^{-1}\mathbf{U}_s''\,\mathbf{M}^{-1}\mathbf{p}\Big] + \mathcal{O}(\delta t^4),\end{aligned} \tag{2}$$

where $\mathbf{q}$ are the positions, $\mathbf{p}$ the momenta, and $\mathbf{M}$ the matrix of body masses. Potential energies $U_s(\mathbf{q})$ gives rise to the 'slow' forces, with derivative $\mathbf{U}'_s$ and Hessian $\mathbf{U}''_s$, and $U_f(\mathbf{q})$ to the 'fast' forces, with derivative $\mathbf{U}'_f$ and Hessian $\mathbf{U}''_f$. The original Hamiltonian being $H = \frac{1}{2}\mathbf{p}^{\mathrm{T}}\mathbf{M}^{-1}\mathbf{p} + U_s + U_f$. We can see from this result that the continuity of the potential energy terms U_s and U_f, and hence the existence of derivatives, will provide an upper bound to the order of the shadow Hamiltonian.

In [4] an alternative scheme was proposed whereby a homogeneous extension of the original Hamiltonian, $\tilde{H}$, is considered. Given the extended homogeneous Hamiltonian system

$$\dot{y}_h(t) \;=\; \tilde{J}\tilde{H}_{y_h}\left(y_h(t)\right),$$

for some $\tilde{J}$ and extended phase-space variables y_h. We can then define

$$A_{i,j} \;=\; \frac{\nabla^i y_h(t)^{\mathrm{T}}\tilde{J}\nabla^j y_h(t)}{2\delta t},$$

here the backward difference operator, for some function $\omega(t)$, is defined as $\nabla^0\omega(t) = \omega(t)$, $\nabla^k\omega(t) = \nabla^{k-1}\omega(t) - \nabla^{k-1}\omega(t-h)$. It is then possible to derive k^{th} order approximations for $\hat{H}$ in terms of the $A_{i,j}$ using Newton's interpolation. We then have, for example, $\hat{H}_{[4]} = A_{1,0} - \frac{1}{2}A_{2,0} + \frac{2}{3}A_{2,1}$, where $\hat{H}_{[k]}$ is the k^{th} order approximation of $\hat{H}$.

3 Switching

Switches are required to split the force between short and long ranges so that a multiple time-step integrator can be used. In order to retain the Hamiltonian the switch must be applied to the energy. Commonly used switches for Lennard-Jones and Coulombic forces have C^1 continuity (NAMD and ProtoMol) which yield a vector field which is C^0. The following scheme, which can provide switches of arbitrary smoothness, was used for testing

$$Y^n(a_{ij}) \;=\; \begin{cases} 1 & \text{if } a_{ij} \le r_o, \\ \sum_{k=0}^{2n+1} \gamma_k \left(\frac{a_{ij}-r_c}{r_o-r_c}\right)^k & \text{if } r_o \le a_{ij} < r_c, \\ 0 & \text{if } a_{ij} > r_c. \end{cases}$$

Here r_o is the switch-on value and r_c the cutoff. The coefficients γ_k for a switch which has smoothness C^n can be determined from the conditions $Y^n(r_o) = 1$, $Y^n(r_c) = 0$, and that all derivatives up to d^nY^n/da_{ij}^n must be zero when equated at r_c and r_o. The coefficients for switches C^2, C^3, C^4 and C^6 are shown in Tab. 1.

n	coefficients γ_i										
	3	4	5	6	7	8	9	10	11	12	13
2	10	-15	6								
3	0	35	-84	70	-20						
4	0	0	126	-420	540	-315	70				
6	0	0	0	0	1716	-9009	20020	-24024	16380	-6006	924

Table 1: Coefficients for a C^n switches. Note $\gamma_1 = \gamma_2 = 0$ for all switches C^2 and above.

4 Experiments

To illustrate the effect of the switches on approximating the shadow Hamiltonian a model of 216 water molecules using periodic boundary conditions (PBC) was used with the Verlet-I integrator utilizing a step ratio $r = 3$. The results can be seen in Fig. 1 when calculating the shadow Hamiltonian using a 12^{th} order interpolated scheme.

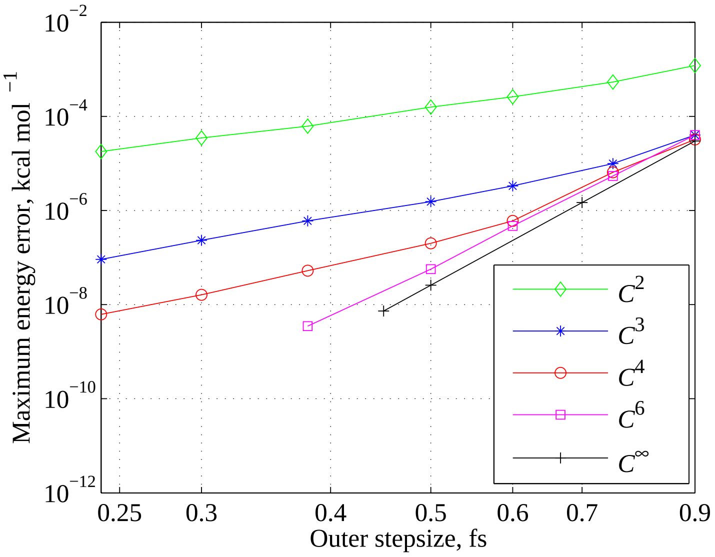

Figure 1: $\hat{H}_{[12]}$ interpolated Shadow Hamiltonian for the Verlet-I method, 216 water molecules with PBC model, for C^2, C^3, C^4 and C^6 switches.

5 Conclusion

As expected from the expansion of the truncated shadow Hamiltonian in Eqn. (2), we have shown that the existence of derivatives of the potential energy terms determines the order of the calculated shadow Hamiltonian, see Fig 1.

References

[1] R. D. Engle, R. D. Skeel, M. Drees, Monitoring energy drift with shadow Hamiltonians
J. Comput. Phys., 206 (2), 432-452, 2005.

[2] Yoshida, H., Recent progress in the theory and applications of symplectic integrators, *Celest. Mech.* **56**, pp 27-43, 1993

[3] B. Leinkuhler, S. Reich, Simulating molecular dynamics,
Cambridge University Press, UK, ISBN 0-521-77290-7, 2004.

[4] R. D. Skeel, D. J. Hardy, Practical construction of modified Hamiltonians
J. Sci. Comput., 23 (4), 1172-1188, 2001.

Phase transformation in bacteriophage T4 tail sheath

Richard James

University of Minnesota, 110 Union St. SE, 55455 Minneapolis, United States of America

We describe an unusual phase transformation that occurs in the tail sheath of the virus bacteriophage T4. This transformation aids the invasion of the host. We then discuss new multiscale methods that can be used to study this transformation. The simplifications afforded by these methods are intimately related to the special symmetries of tail sheath, but they have broad application to structures which, like T4 tail sheath, are composed of identical molecules for which corresponding atoms in each molecule „see“ the same atomic environment up to rotation and translation.

Differentiable mesoscopic fields in molecular dynamics simulation: construction, dynamics, and coupling of length scales

A. Streit, R. E. Zillich, P. Baumann, P. Klein

Fraunhofer Institut für Techno- und Wirtschaftsmathematik
Competence Center High Performance Computing und Visualisierung
Fraunhofer-Platz 1, D-67663 Kaiserslautern
peter.klein@itwm.fraunhofer.de

ABSTRACT

Based on previous work of one of the authors, we define “coarse grained” local observables for temperature and stress, which are thermodynamically consistent and continuously differentiable with respect to “coarse grained” coordinates. This allows for the construction of dynamical equations, where these observables are used as space-localized extensions of Hamilton's equations of motion. Since these new equations are designed to sample the free enthalpy ensemble, strong dynamical effects on e.g. the stress are not captured in the sense of mesoscopic transport equations. Therefore, additionally, we present a method to derive coarse scale equations from an atomistic model, together with the coupling of a coarse scale and an atomistic region, directly from an exact Hamiltonian. Reflectionless boundary conditions are used to avoid reflection of waves with small wave length at the interface and interpolation functions from coarse to fine scale are chosen in such a way that the dispersion relations on the coarse scale are correct. Unlike other coupling methods, this approach allows approximations directly in the Hamiltonian, leading to energy conserving approximated evolution equations, while keeping the correct transition between the two scales. We also present a generalization of this coarse-fine scale coupling to finite temperature.

1. Local observables and extended system methods

We derive one-particle observables for Hamiltonian dynamics in the microcanonical ensemble, where the Hamiltonian is given by

$$H_{NVE} = \sum_{i=1}^{N} \frac{\mathbf{p}_i^2}{2m_i} + \Phi\left(\{\mathbf{q}_i\}\right) + \sum_{i=1}^{N} \Phi_{ext}\left(\mathbf{q}_i\right).$$

Using the localization kernel g, defined by

$$g_\alpha(q^\alpha) := \frac{1}{\delta^\alpha}\cos^2\left(\frac{\pi}{2}\frac{q^\alpha}{\delta^\alpha}\right)\Theta\left(\left(\delta^\alpha\right)^2 - \left(q^\alpha\right)^2\right),\ \Theta(\varsigma) := \begin{cases} 1 \ : & \varsigma \geq 0 \\ 0 \ : & \varsigma < 0 \end{cases},$$

$$g(\mathbf{q}) := \prod_{\alpha=1}^{3} g_\alpha(q^\alpha),$$

we obtain

$$n(\mathbf{r}) := \sum_i m_i g(\mathbf{q}_i - \mathbf{r}), \quad \mathbf{p}(\mathbf{r}) := \sum_i \mathbf{p}_i g(\mathbf{q}_i - \mathbf{r}),$$

$$\mathbf{f}_{ext}(\mathbf{r}) := -\sum_i \nabla_{\mathbf{q}_i} \Phi_{ext}(\mathbf{q}_i) g(\mathbf{q}_i - \mathbf{r}), \quad t(\mathbf{r}) := \frac{1}{2}\sum_i \frac{\mathbf{p}_i \otimes \mathbf{p}_i}{m_i} g(\mathbf{q}_i - \mathbf{r}),$$

and note that the macroscopic continuity equation $m\, dn/dt = div\, \mathbf{p}$ is fulfilled if we use Hamilton’s equations of motion for the underlying particle dynamics. This motivates us to construct a stress tensor consistent with the macroscopic continuity equation for the linear momentum density, $\dot{\mathbf{p}}(\mathbf{r},t) = \nabla_{\mathbf{r}} \cdot \boldsymbol{\sigma}(\mathbf{r},t) + \mathbf{f}_{ext}(\mathbf{r},t),$ for arbitrary but sufficiently smooth potential functions.

In order to do that, we embed the configuration space in a larger space of ordered differences and use an analytical continuation of the potential function. In the extended space, we apply the known construction of stress tensors for pair potentials, and project the result back into physical space. Using this approach, we obtain a stress tensor consistent with the macroscopic continuity equation for the linear momentum density.

In the spirit of extended system methods, we now couple the temperature and stress observables as boundary conditions to the Hamiltonian dynamics:

$$\dot{q}_i^\alpha = \frac{p_i^\alpha}{m_i} + \frac{\pi_b^\alpha}{l^\alpha - \Delta^\alpha} \; a_\alpha(q_i^\alpha), \alpha = 1,2,3, i = 1,\dots,N,$$

$$\dot{p}_i^\alpha = F_i^\alpha - \frac{\xi_p^\alpha}{N} p_i^\alpha b_\alpha(q_i^\alpha) - \frac{\pi_b^\alpha}{l^\alpha - \Delta^\alpha} p_i^\alpha b_\alpha(q_i^\alpha), \alpha = 1,2,3, i = 1,\dots,N,$$

$$\dot{\xi}_p^\alpha = \frac{1}{Q_p N}\sum_{i=1}^N \left(\frac{\left(p_i^\alpha\right)^2}{m_i} - k_B T \right) b_\alpha(q_i^\alpha), \alpha = 1,2,3,$$

$$\dot{\eta} = \eta \sum_{\alpha=1}^3 \left(\frac{1}{N}\sum_{i=1}^N \xi_p^\alpha b_\alpha(q_i^\alpha) + \xi_{\pi_b}^\alpha \right), \dot{l}^\alpha = \frac{\pi_b^\alpha}{2}, \alpha = 1,2,3,$$

$$\dot{\pi}_b^\alpha = \frac{1}{\gamma}(\Pi_{b,l^\alpha}^{\alpha\alpha} - P)\frac{4l^1l^2l^3}{l^\alpha} - \xi_{\pi_b}^\alpha \pi_b^\alpha, \alpha = 1,2,3, \dot{\xi}_{\pi_b}^\alpha = \frac{1}{Q_{\pi_b}}\left(\gamma\left(\pi_b^\alpha\right)^2 - k_B T\right), \alpha = 1,2,3,$$

where *b* has the same form as *g*, and is centered at the boundary, *a* is the integral of *b*, and the boundary pressure is given by

$$\boldsymbol{\Pi}_{b,l^\alpha} := -\boldsymbol{\sigma}_{b,l^\alpha}, \; \boldsymbol{\sigma}_{b,l^\alpha} := \frac{\delta^\beta \delta^\gamma}{4 l^\beta l^\gamma} \sum_{k^\beta=1}^{n^\beta} \sum_{k^\gamma=1}^{n^\gamma} \boldsymbol{\sigma}\left(\mathbf{r}_{n^\alpha \mathbf{e}_\alpha + k^\beta \mathbf{e}_\beta + k^\gamma \mathbf{e}_\gamma}\right).$$

These dynamical equations conserve the energy function in

$$H_{NPT} = \frac{1}{2}\sum_{i=1}^N \sum_{\alpha=1}^3 \frac{(p_i^\alpha)^2}{m_i} + \Phi\left(\{\mathbf{q}_i\}\right) + \frac{Q_p}{2}\sum_{\alpha=1}^3 \left(\xi_p^\alpha\right)^2 + k_B T \ln \eta + \frac{\gamma}{2}\sum_{\alpha=1}^3 \left(\pi_b^\alpha\right)^2 + \frac{Q_{\pi_b}}{2}\sum_{\alpha=1}^3 \left(\xi_{\pi_b}^\alpha\right)^2 + 8Pl^1l^2l^3.$$

A symplectic interpretation of this dynamics then allows for the construction of numerical integration schemes with high stability, i.e. without energy drifts. Slight modifications of this dynamics will allow for the study of micro-crack dynamics for instance, where the cracks are fully within the inner region of a simulation cell and external stresses are implemented within the boundary conditions.

2. Coupling of atomistic and coarse scale region

In order to capture strong dynamical effects we have derived equations coupling an atomistic region and a coarse grained region directly from the underlying Hamiltonian, assumed to be harmonic in the coarse grained region, by splitting the displacements into a coarse, u_c, and a fine scale part, u_f [1], similar to the displacement splitting in [2]. They are defined as linear interpolation from coarse and fine scale variables, *d* and *b*, to the atomic equilibrium positions, $u = u_c + u_f = Nd + Bb$, with *N* and *B* the corresponding interpolation matrices. The coarse scale displacements, *d*, are defined on a regular coarse grid over the equilibrium positions of the atoms, the fine scale displacements, *b*, at their equilibrium positions in between the grid points, and the interpolation matrices satisfy $N^T B = 0$.

For coupling an atomistic and a coarse scale region, we split the fine scale displacements in two parts, b_1 and b_2, the first corresponding to the fine scale variables in the atomistic, the second in the coarse scale region. Again we require $B_1^T B_2 = 0$ for the corresponding interpolation matrices. For harmonic interactions, we insert the displacement splitting in the Hamiltonian, and derive the evolution equations

$$N^T M N\ddot{d} = N^T K(Nd + B_1 b_1 + B_2 b_2), \tag{1.1}$$

$$B_1^T M B_1 \ddot{b}_1 = B_1^T K(Nd + B_1 b_1 + B_2 b_2), \tag{1.2}$$

$$b_2(t) = \int_0^t \theta(\tau) B_2^T K(Nd + B_1 b_1)(t-\tau)\, d\tau + R(t), \tag{1.3}$$

Eqn.(1.3) provides a boundary condition for Eqns.(1.1) and (1.2) and is derived from a similar equation by Laplace transformation. These equations can also be derived from the Mori-Zwanzig projection operator formalism [3].

Calculation of the boundary condition from all fine scale variables b_2 is computationally expensive since it amounts to solving the whole atomistic system. But the derivation allows for approximations directly in the Hamiltonian, leading to energy conserving approximate evolution equations together with a reflectionless boundary condition. Numerical experiments showed that using only those variables near the interface is already enough to avoid reflections at the interface. However, if we neglect part of the variables b_2, the wave speed in the coarse scale region changes. The reason is a change in the dispersion relation. We avoid this by choosing the interpolation from coarse to fine scale in such a way, that the difference between atomistic and coarse scale dispersion relation is reduced. At the same time, the support of the interpolation function of each node should be local in order to get a sparse coarse scale mass matrix, $N^T M N$. We get very good agreement of the dispersion relations for interpolation functions with only a slightly larger support than for linear interpolation between the nodes. A possible approximation in the Hamiltonian is to use the boundary condition only for Eqn. (1.2) and neglect it in (1.1). In Fig. 1 we show an example for this approximation. We used fine scale variables b_2 only near the interface and the memory integral was computed over the last 200 time steps.

The residual forces $R(t)$ in Eqn.(1.3) formally depend on the initial conditions of the fine scale variables in the coarse scale region and, for non-zero temperature simulations, effectively constitute a heat bath, as discussed in the following section.

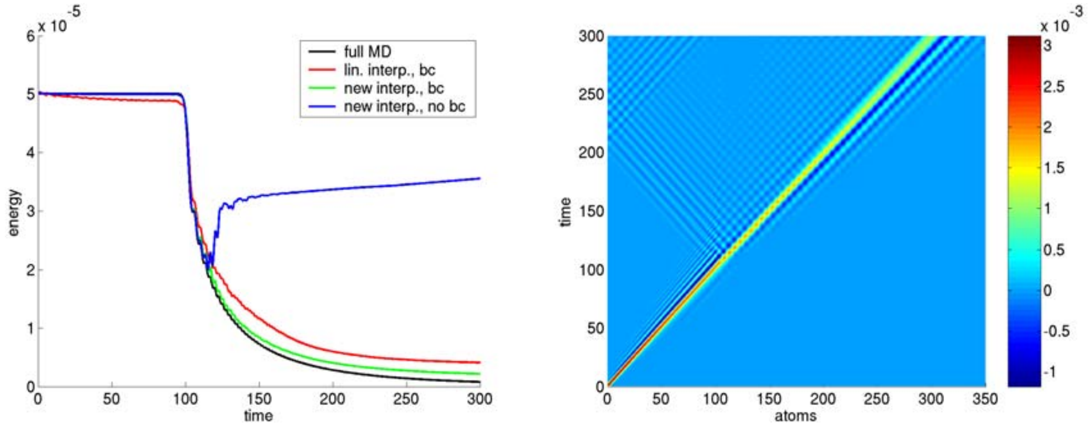

Figure1. One dimensional chain of 350 atoms. Atomistic region of 100 atoms on the left, coupled to a coarse scale region on the right of the domain. Left: energy in the atomistic region for different interpolations, with and without boundary condition (bc), right: local stress for new interpolation in whole domain.

3. Non-equilibrium NVT simulations

We have derived and implemented a method [4] based on the Mori-Zwanzig projection operator formalism similar to Ref.[3] to embed a finite temperature MD simulation (NVT) of a crystaline, electrically insulating solid in a macroscopic continuum. This provides a reflectionless boundary condition, but neglects the coarse grained degrees of freedom outside the atomistic region, *i.e.* we only take into account Eqns.(1.2) and (1.3) while $d = 0$ in the limit of infinite coarse graining. The temperature dependent residual forces (“random forces”) $R(t)$ acting on the boundary atoms are sampled in pseudorandom fashion such that they satisfy the fluctuation-dissipation theorem $\gamma(t-t') = < R(t)R(t') > / k_B T$ where $\gamma(t-t')$ is the memory kernel that results from inserting Eqn.(1.3) in Eqn.(1.2), and the brackets denote averaging over the canonical ensemble. Sampling $R(t)$ is straightforward using the normal mode decomposition of the crystal. However, even if the normal modes are not known, knowledge of the memory kernel $\gamma(t-t')$ (which can also be obtained by other means than the above procedure or normal mode decomposition, *e.g.* by MD simulation) is sufficient to generate an approximate random force time series that fulfills the fluctutation-dissipation theorem. The method is suitable when the assumption of a homogeneous temperature distribution is not applicable, *i.e.* for non-equilibium molecular dynamics simulations of transport phenomena such as thermal conduction, or of phenomena which are local in space and/or time such as surface processes. The accuracy of the reflectionless boundary condition and of temperature control is validated for solid argon, even close to the melting transition. We will generalize the method to multiscale MD simulations of atomic and coarse grained degrees of freedom at finite temperature.

References

[1] A. Streit, P. Klein, Coupling the continuum with molecular dynamics using a projection operator approach, submitted to J. Comp. Phys.
[2] G. J. Wagner, W. K. Liu, Coupling of atomistic and continuum simulations using a bridging scales decomposition, J. Comp. Phys. 190 (2003), pp.249-274
[3] S. A. Adelman, J. D. Doll, Generalized Langevin equation approach for atom/solid-surface scattering: General formulation for classical scattering off harmonic solids, J. Chem. Phys. 64(1976), pp. 2375
[4] R. E. Zillich, Non-reflecting boundary conditions for finite temperature molecular dynamics, submitted to Comp. Phys. Comm.

On some microscopic stochastic models of materials and their macroscopic limits

Claude LeBris

Ecole Nationale des Ponts et Chaussees, 6 & 8 avenue Blaise Pascal, Cite Descartes, Champs-sur-Marne,
77455 Marne La Vallee Cedex 2, France

We introduce some notion of stochastic lattices that may be used for the modelling of materials at the microscopic scale. We define the corresponding energies and investigate their macroscopic limits, with a view to defining macroscopic densities of mechanical energies. We also establish the link between such questions and stochastic homogenization theory. This is a joint work with Xavier Blanc (Univ. Paris 6) and Pierre-Louis Lions (College de France).

Partial thermostatting and multiple time-scale simulation of coarse-grained MD

Ben Leimkuhler

University of Leicester, Department of Mathematics, University of Leicester, LE2 1XH Leicester, United Kingdom

Coarse-grained molecular dynamics models create fundamental challenges for numerical simulation, including (1) barriers to effective thermalization among the various degrees of freedom and (2) difficulties for stable numerical integration of the equations of motion formulated on multiple time scales. In this talk, I will discuss both of these challenges, describing dynamical thermostatting methods that promise enhanced and targeted thermalization and also focussing on their use within a multiple timescale simulation framework.

Self organized strain textures

Pol Lloveras

Universitat de Barcelona, Departament ECM, Facultat de Física, Av. Diagonal 647, 08028 Barcelona, Spain

We use a 2D Ginzburg-Landau free-energy expansion to study the strain patterns observed in some martensitic materials both above and below the structural transition. Additionally to the standard order parameter (deviatoric strain) expansion, we include the non local anisotropic long range potential coming from the compatibility condition between the different components of the strain tensor. The existence of spatially correlated quenched disorder is also taken into account. It couples to the order parameter through the harmonic term and has an effect on the local transition temperature.

Purely relaxational simulations of the model show the formation of directional twin variants of the martensite below the transition temperature and self-organized strain textures (tweed) in the austenite phase. A coexistence between tweed and twins is also observed in a narrow temperature range, according to the first order character of the transition. Similar studies on magnetic models have revealed that short wavelength modulations of the magnetization (magnetic tweed) observed above the Curie temperature never coexist with the ferromagnetic dipolar phase, according to the second order character of the phase transition. The different phases observed in the simulations are characterized by means of the distribution of the order parameter and the volume fraction of transformed regions (martensite phase).

We have also studied the role of the long range anisotropic interactions on the stabilization of the structures observed. Physically, the relative weight of this term is related to the elastic anisotropy of the material. The result obtained is that the directionality of tweed and twins as well as their characteristic length scales decrease as the weight of this term is reduced. Therefore a large elastic anisotropy is a necessary condition for a material in order to show highly anisotropic elastic strain patterns.

From Electrons To Finite Elements: A Concurrent Multiscale Approach

Gang Lu[1], *Ellad B. Tadmor*[2]

[1]*Department of Physics & Astronomy, California State University Northridge, 18111 Nordhoff Street Department of Physics, 91330-8268 Northridge, USA*

[2]*Department of Aerospace Engineering and Mechanics, University of Minnesota, 55455 Minneapolis, USA*

We have recently developed a multiscale modeling approach that concurrently couples quantum mechanical calculations for electrons, to empirical atomistic calculations for classical atoms, and to continuum mechanical calculations for finite elements, in a unified description [1]. In specific, the electronic structure calculations are performed with the plane-wave pseudopotential method based on the density-functional theory (DFT), the classical atomistic simulations with the embedded-atom method (EAM), and the continuum calculations with the Cauchy-Born rule in the local Quasicontinuum (QC) formulation [2]. The multiscale method is implemented in the context of the QC framework with the additional capability to include DFT calculations for a selection of non-local QC atoms. A novel coupling scheme has been developed to combine the DFT and EAM calculations [3] in a seamless fashion to deal with non-local QC atoms, whereas the local QC atoms are treated in the usual way by the informed finite element calculations.

We apply this method to study crack propagation in Al. A mode I loading is applied to a (111)[110] crack. The atomistic mechanisms of dislocation nucleation from the crack tip, and crack propagation are investigated. In particular, the critical stress intensity factor is determined and compared to EAM-based QC results. The electronic states at the crack tip during the fracture process are examined in detail, and the relevant energetics are computed.

Reference:

[1] G. Lu, E.B. Tadmor, and E. Kaxiras, Phys. Rev. B 73, 024108 (2006).

[2] E.B. Tadmor, M. Ortiz, and R. Phillips, Philos. Mag. A 73, 1529 (1996).

[3] N. Choly, G. Lu, W. E and E. Kaxiras, Phys. Rev. B 71, 094101 (2005).

Vertical and Horizontal Communication across Scales in Materials Simulations: Strain Localization in Al

Jaime Marian

Lawrence Livermore National Laboratory, 7000 East Avenue, L-367, 94551 Livermore, United States of America

The fields of high-pressure physics and mechanics have received considerable attention in recent years as a result of a newly-sparked interest in detonation-driven and spallation failure experiments and the development of new plastic and hydrodynamic theories. Nevertheless, these theories still rely excessively on a number of material parameters (typically more than a dozen) that are obtained ad hoc or by way of semi-empirical estimations. A complete description of explosion-driven processes with a minimum amount of empiricism requires the consideration of multiple materials deformation mechanisms operating at multiple scales. The inherent multiscale character of spall, for example, requires that models developed to capture the relevant physical phenomena be constructed in such a way that multiple scales can be treated concurrently and/or sequentially. With the advent of supercomputers, these horizontal and vertical-communication methodologies have become more and more plausible so that one is now able to self-consistently construct the physics of spall from the inside out and from the bottom up, from vacancy aggregation all the way to spall fragmentation. In this work we present finite-element simulations of ring expansion and cylindrical-plate spallation that use a continuum porous plasticity model as constitutive law which, in turn, has been fitted using mixed atomistic/mesoscale simulations. These atomistic/mesoscale simulations make use of parameter-less interatomic potentials and are employed to characterize void growth and coalescence. Void embryos are obtained by recourse to first-principles-fitted Monte Carlo calculations. The particular case of Al will be presented.

Multiscale models for ion beam deposition

Michael Moseler

Fraunhofer Institute for Mechanics of Materials IWM, Wöhlerstr. 11, 79108 Freiburg, Germany

The interaction of low energy ion beams with solid surfaces has become an important tool for the growth of thin films and the modification of interface topographies. Single deposition events can be studied by a concurrent coupling of quantum, classical atomistic and continuum mechanics regions provided the different phonon dispersion relations are treated properly [1]. The surface modification by a random hail of ions can be described by a consecutive coupling of quantum or classical molecular dynamics results and continuum growth equations for the surface topography. These strategies are exemplified for carbon nanomaterials and nanoparticle impacts. Recently, the ultrasmoothness of ion-beam grown diamond-like carbon coatings has been explained by a serial quantum/atomistic/continuum multiscale model [2]. At the atomic scale, carbon ion impacts induce downhill currents in the top layer of a growing film. At the continuum scale, these currents cause a rapid smoothing of initially rough substrates via erosion of hills into neighboring hollows. The predicted surface evolution is in excellent agreement with atomic force microscopy measurements. This mechanism is general as shown by similar simulations for amorphous silicon [2] and films grown by energetic cluster impact [3].

[1] M.Moseler, J.Nordiek, H.Haberland, Reduction of the reflected pressure wave in the molecular-dynamics simulation of energetic particle-solid collisions, Phys. Rev. B 56, 15439 (1997)

[2] M. Moseler, P. Gumbsch, C. Casiraghi, A. Ferrari, J. Robertson, The ultrasmoothness of diamond-like carbon, Science, 309, 2005, 1545-1548.

[3] M.Moseler, O.Rattunde, J.Nordiek, H.Haberland, On the origin of surface smoothing by energetic cluster impact: molecular dynamics simulation and mesoscopic modeling, Nucl. Inst. & Methods B 164, 522 (2000)

Nonlinear Dynamics of Transformation Induced Plasticity in Shape Memory Alloys (Experimental and Theoretical Study)

Oleg Naimark[1], *Vladimir Leont'ev*[1], *Sergey Uvarov*[1]

[1]*Institute of Continuous Media Mechanics of Russian Academy of SCiences, 1 Acad.Korolev str., 614013 Perm, Russia*

Statistical thermodynamics of martensitic transformation allowed the development of phenomenology of transformation induced plasticity (TRIP) in the form of generalization of the Ginzburg-Landau phenomenology [1]. This variant of phenomenology reflects characteristic non-linearity of transformation and the linkage of thermodynamic driving force for martensitic variants growth with mechanisms of plastic accommodation at the boundary between austenite and martensite phases. It was shown that the generation and growth of martensitic variants play both the role of driving force and structural heterogeneity (similar to the grains) for dislocation structures providing the accommodation of two phases in the form of TRIP. These features provide the properties of super-elasticity and shape memory as the interaction of two transformations: phase (martensitic) transformation and structural-scaling transformation in the dislocation ensembles. Three order parameters are responsible for thermodynamics and kinetics of mentioned transitions: transformation strain – deformation induced by the growth of martensitic variants, the defect density tensor – deformation induced by dislocation ensembles at the interphase boundary and the structural-scaling parameter related to the scale distribution of above parameters. Statistical description revealed the specific sense of structural-scaling parameter that has the nature of the "effective temperature" for mesoscopic (dislocation) structures. The analysis of kinetic equations for order parameters allowed us to establish two types of collective modes related to the transformation and defect induced strains that have the features of the self-similar auto- solitare waves corresponding to the multiscale (controlled by the kinetics of structural-scaling parameter) orientation transitions in ensembles of martensitic variants and dislocation ensembles. These results were supported by the experiments on the study of kinetics of transverse free oscillation damping of the Ti-Ni alloy string and the recording of force induced longitudinal finite amplitude disturbances in mentioned preloaded string under the pass of critical stress for temperature providing the superelasticity. It was shown that the generation of collective modes lead to the anomalous damping in the case of free oscillation and dramatic decrease of the symmetry of system supported by the dimension (correlation) analysis of the stress portraits (the Poincare cross-section) recoded by piezo-ceramic gage. The hysteresis properties related to both type of transformations were studied experimentally in dynamic experiment realized in the split bar (Hopkinson) test for the strain rate range 102 – 104 s-1 that allowed the deeper penetration in the metastability area.

1. O.B.Naimark, L.V.Filimonova, V.A.Barannikov, V.A.Leont'ev and S.V.Uvarov. Non- linear dynamics of reversible plasticity in shape memory alloys, Physical Mesomechanics, 4, 5(2001), pp.13-27.

Effective computation of single-slip elastoplastic microstructures in finite strains

Carsten Carstensen[‡], **Sergio Conti**[†] and **Antonio Orlando**[‡]
[‡] **Institut für Mathematik, Humboldt-Universität zu Berlin, Germany**
[†] **Fachbereich Mathematik, Universität Duisburg-Essen, Germany**

ABSTRACT

The modeling of the elastoplastic behaviour of single crystals with infinite latent hardening leads to a nonconvex energy density, whose minimization produces fine structures. The computation of the quasiconvex envelope of the energy density involves the solution of a global nonconvex optimization problem. Previous work based on a brute-force global optimization algorithm faced huge numerical difficulties due to the presence of clusters of local minima around the global one. We present a different approach which exploits the structure of the problem both to achieve a fundamental understanding on the optimal microstructure and, in parallel, to design an efficient numerical relaxation scheme.

1. Model Problem

We consider single-crystal plasticity in $2D$ with only one active slip system defined by s and n, the slip direction on the slip plane and the normal to the slip plane, respectively. We assume linear hardening law with the internal variable $p \in \mathbb{R}$ and hardening modulo h, and the multiplicative decomposition of the deformation gradient $F = F_e F_p$ with $F_p = I + \gamma s \otimes n$, where $\gamma \in \mathbb{R}$ is the plastic slip. We focus only on the first time step of a time-discrete scheme, and set equal to zero the initial values of the internal variables (γ, p). Within the framework of rate-independent processes, the incremental problem can be cast equivalently into a variational formulation expressed only in terms of the deformation gradient F and can therefore be analysed by the methods of the calculus of variations [1]. The free energy density $W(F_e, p)$ and the dissipation potential $J(\gamma, p)$ define the constitutive behaviour of the single crystal, with $W(F_e, p)$ being the sum of an elastic $W_e(F_e)$ and a plastic contribution $W_p(p)$. Given the material constants μ, κ, if $\det F_e > 0$

$$W_e(F_e) = \frac{\kappa}{4}((\det F_e)^2 - 1) - \frac{\kappa + 2\mu}{2} \log(\det F_e) + \frac{\mu}{2}(|F_e|^2 - 2)\,, \tag{1}$$

otherwise $W_e(F_e) = \infty$, whereas $W_p(p) = \frac{h}{2}p^2$. As for the dissipation potential, we set $J(\gamma, p) = \tau_{cr}|\gamma|$ if $|\gamma| + p \leq 0$, with τ_{cr} the critical shear stress, otherwise $J(\gamma, p) = \infty$. This model has been considered also in [2,3,4]. Minimizing out locally the internal variables (γ, p) one obtains the condensed energy

$$W_{\text{cond}}(F) = U(F) + \frac{\mu}{2}(|F|^2 - 2) - \frac{1}{2}\frac{(max(0, \mu|Cs \cdot n| - \tau_{cr}))^2}{\mu Cs \cdot s + h}\,, \tag{2}$$

with $C = F^T F$. The energy density (2) is not rank-one convex and, hence, not quasiconvex. As a result, one may expect non attainment of minimizers for the corresponding functional, and developments of oscillations in the gradients of low-energy deformations.

For the case under consideration, the occurrence of such microstructures has been indeed shown in [2] by a direct finite element simulation using representative volume elements under periodic boundary conditions. The macroscopic material behaviour can be, however, understood by minimizing out locally the possible microstructures and defining the quasiconvex envelope of W_{cond}. Unfortunately, a closed form for quasiconvex envelopes of condensed energies of the kind of W_{cond} is known only in few simplified cases [5,6,7] and therefore, one usually resorts to an approximation to the rank-one convex envelope $W^{rc}_{\mathrm{cond}}(F)$ based on laminates. Current approaches to the computation of $W^{rc}_{\mathrm{cond}}(F)$ resort to brute-force global optimization techniques [2] or their variants where the computational effort is reduced by fixing some laminate related parameters on the basis of conjectures motivated by physical considerations [4,8].

2. Mixed analytical-numerical relaxation

We consider first an elastically rigid problem with $F_e = Q$ for $Q \in SO(2)$, and only the contribution from the plastic free energy is considered, i.e., dissipation is neglected, as described in [5]. The condensed energy for this case is then given by

$$W'(F) = \begin{cases} \frac{h}{2}\gamma^2 & \text{if } F = Q(I + \gamma s \otimes m) \quad Q \in SO(2)\,, \\ \infty & \text{else}\,, \end{cases} \tag{3}$$

with the quasiconvex envelope obtained in [5] as

$$W'_{qc}(F) = \begin{cases} \frac{h}{2}(|Fm|^2 - 1) & \text{if } \det F = 1 \text{ and } |Fs| \leq 1\,, \\ \infty & \text{else}\,. \end{cases} \tag{4}$$

The quasiconvex, rank-one convex, and polyconvex envelope are equal. In particular, the optimal energy is given by a first-order laminate, which is supported on two matrices which have plastic deformation γ of the same magnitude and opposite sign (for details see [5]).

Inspired by results based on the global optimization [2], we then construct a more refined model by assuming the microstructure to have the form of a laminate of second order, which is supported either on rigid-plastic deformations or on purely elastic ones. In this case, assuming volume-preserving deformations, the relaxation is reduced to a global minimization of a function of only one variable which defines the orientation of the laminate. Using this solution and the splitting of F_p from the analytic relaxation of $W'_{qc}(F)$ in [5] we obtain an approximate second order laminate. The latter is then used as a starting point for the local minimization of the full energy density, including dissipation, and removing the kinematic constraint.

3. Optimality check

In order to check whether the local minimum found in the previous section yields the relaxed energy, in this section we consider the case of F being supported on the first order laminate with phases

$$F_0 = F - (1-\lambda)\rho a \otimes b, \quad F_1 = F + \lambda \rho a \otimes b\,,$$

and relaxed energy equal to $R^{(1)}W_{\mathrm{cond}}(F)$. Let PW_{cond} denote the polyconvex envelope of W_{cond}, we recall

$$PW_{\mathrm{cond}}(F) = \sup\left\{\ell(F) : \begin{array}{c}\text{for all polyaffine } \ell \text{ with}\\ \ell(A) \leq W_r(A) \text{ for all } A \in \mathbb{R}^{2\times 2}\end{array}\right\} \tag{5}$$

where the generic polyaffine function in $\mathbb{R}^{2\times 2}$ has the following expression

$$\ell(A) = \alpha + H\colon A + \beta \det A\,. \tag{6}$$

Assuming that there holds

$$R^{(1)}W_{\mathrm{cond}}(F) = PW_{\mathrm{cond}}(F) \tag{7}$$

this leads to the following system of 10 equations in 6 unknowns

$$\begin{array}{ll}\alpha + H\colon F_0 + \beta\det F_0 = W_{\mathrm{cond}}(F_0)\,, & \alpha + H\colon F_1 + \beta\det F_1 = W_{\mathrm{cond}}(F_1)\,,\\ H + \beta\operatorname{cof}F_0 = \frac{DW_{\mathrm{cond}}}{DA}\Big|_{F_0}\,, & H + \beta\operatorname{cof}F_1 = \frac{DW_{\mathrm{cond}}}{DA}\Big|_{F_1}\,,\end{array} \tag{8}$$

which is, however, determinated if condition (7) is met. Once this linear system is solved, we check then that the following condition is met

$$\min_{A\in\mathbb{R}^{2\times 2}}\{W_{\mathrm{cond}}(A) - PW_{\mathrm{cond}}(A)\} \geq \mathit{eps}$$

which ensures that the polyaffine function that coincides with the unrelaxed energy on the support of the laminate is below the condensed energy, up to a very small error $\mathit{eps} \geq 0$.

4. Numerical example

In this section we report on the numerical relaxation of W_{cond} following the procedure described in the previous sections for pure shear strain $F = I + \xi r \otimes r^{\perp}$ with $r = (1, 0)$, $r^{\perp} = (0, 1)$ and for the material constants $\mu = 1.0 \cdot 10^4$MPa, $\kappa = 1.5 \cdot 10^4$MPa, $h = 1.0 \cdot 10^3$MPa and $\tau_{cr} = 10$MPa. Figure 1(a) depicts the condensed energy W_{cond} (see eq. (2)) together with W_e (see eq (1)), W'_{qc} (see eq (4)) and the value of the energy over the approximate second order laminate (which we denote by $f^{**}(0)$). We observe a very good quantitative agreement for the values of the relaxed energy with those in [2] which had required a significantly higher numerical effort. Also, approximations of the polyconvex hull $W^{pc}_{\delta,r}(F)$, realized with the procedure described in [2] and in this paper are compared. Figure 1(b) depicts the value of the volume fractions λ and λ_1 whereas $\lambda_0 = 1$. Initially, the material is in a homogeneous elastic state. Then an elastic state and a mixture of two opposite–slip plastic states appears. The volume fraction of the elastic phase starts at 100% and then decreases continuously until it vanishes at a shear $\xi = 0.13$. Both plastic phases then progress with slowly varying volume fractions until the homogeneous phase F is stable.

Acknowledgements

This work has been supported by the DFG Priority Program 1095 ‘Analysis, Modeling and Simulation of Multiscale Problems’ under projects Ca 151/13 and Co 304/1.

References

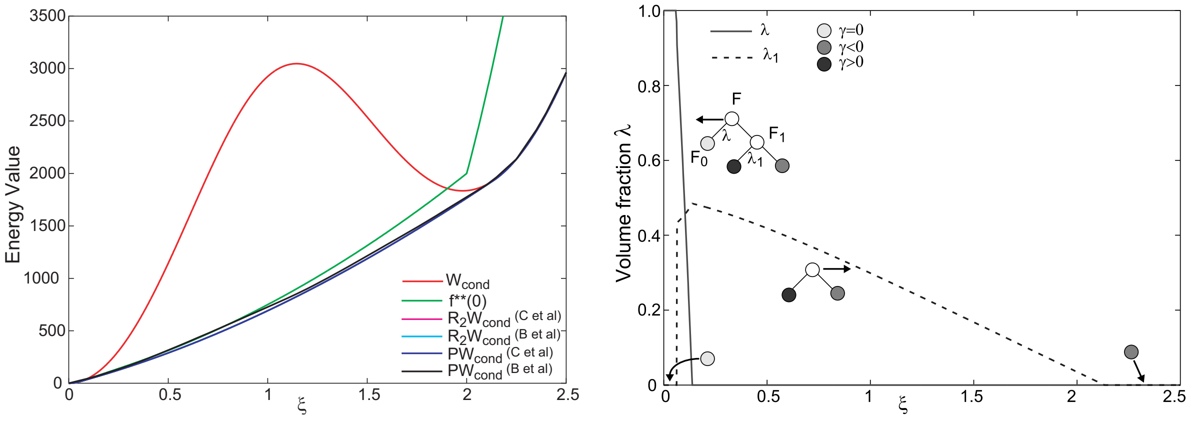

(a) (b)

Figure 1. (a) Bounds to the quasiconvex envelope of the condensed energy for zero dissipation together with polyconvex and second-order laminate envelope for the condensed energy density in single-slip plasticity. (b) Volume fractions λ and λ_1 for different values of ξ.

[1] M. Ortiz, E.A. Repetto, Nonconvex energy minimization and dislocation structures in ductile single crystals. J. Mech. Phys. Solids, **47**, 397–462 (1999).

[2] S. Bartels, C. Carstensen, K. Hackl, U. Hoppe, Effective relaxation for microstructure simulations: algorithms and applications. Comput. Methods Appl. Mech. Engrg., **193**, 5143–5175 (2004).

[3] C. Carstensen, K. Hackl, A. Mielke, A variational formulation of incremental problems in finite elasto–plasticity. Proc. R. Soc. Lond. A, **458**, 299–317 (2002).

[4] C. Miehe, M. Lambrecht, E. Gürses, Analysis of material instabilities in inelastic solids by incremental energy minimization and relaxation methods: evolving deformation microstructures in finite plasticity. J. Mech. Phy. Solids, **52**, 2725–2769 (2004).

[5] S. Conti, Relaxation of single-slip single-crystal plasticity with linear hardening, In this proceedings.

[6] S. Conti, M. Ortiz, Dislocation microstructures and the effective behavior of single crystals. Arch. Rational Mech. Anal., **176**, 103–147 (2005).

[7] S. Conti, F. Theil, Single-slip elastoplastic microstructures, Arch. Rational Mech. Anal., **178**, 125-148 (2005).

[8] M. Ortiz, E.A. Repetto, L. Stainier, A theory of subgrain dislocation structures. J. Mech. Phys. Solids, **48**, 2077–2114 (2000).

Long Time Scale Simulations of Atomic Structure and Dynamics at Defects in Metals

A. Pedersen [1], G. Henkelman [2], J. Schiøtz [3], H. Jónsson [1]

[1]Faculty of Science VR-II and Science Institute, Univ. of Iceland
[2]Department of Chemistry and Biochemistry, University of Texas
[3]Department of Physics, Technical University of Denmark

Computer simulations of chemicals and materials on the atomic scale have proved to be useful in many scientific disciplines. They can provide insight and help interpret experimental results and in some cases even provide useful predictions of properties of new chemicals or materials. A serious limitation of such simulations, however, is the short time interval that can be simulated by standard approaches - on the order of nanoseconds. We make use of a recently developed algorithm that can be used to simulate time evolution of solids over longer time, on the order of milliseconds or more.

The Algorithms

The Kinetic Monte Carlo (KMC) algorithm has often been used to simulate long time scale evolution, but in its usual form it requires a predefined table of the events that are allowed to take place in the system. Those types of simulations can, therefore, only give rather limited information about the system. Transitions that had not been anticipated already before the simulation cannot occur. Also, in order to make a table of possible events, an assignment of the atoms to lattice points both before and after each transition is needed, making simulations of irregular structures such as defects and amorphous solids not possible.

A recently developed adaptive-KMC (AKMC) method [1] extends the algorithm in such a way that a reference lattice is not needed and the mechanism of possible transitions is found during the simulation by locating first order saddle points on the potential energy surface. For each state of the system that comes up in the simulation, an unbiased search is made for low lying saddle points on the potential energy rim surrounding the initial state minimum. The rate of each transition is determined by assuming that Harmonic Transition State Theory is applicable, thereby requiring that the system is a solid at low enough temperature. The rate of each transition can be expressed as $k = \nu \exp[-\Delta E / k_B T]$, where the prefactor ν relates to the frequency of vibrational modes at the initial state as well as at the saddle point and ΔE is the energy difference between the reactant state and the saddle point.

The saddle points are found by numerous, independent searches that start with a random displacement from the initial state minimum energy structure. Prebased on an efficient algorithm for finding the lowest eigenvalue of the Hessian matrix and reversing the component of the atomic force vector along this direction. The AKMC method has been implemented in such a way that numerous saddle point searches are carried out simultaneously by distributing the computational effort over a number of computers (see http://eon.cm.utexas.edu).

Results

The simulation described here corresponds to a grain boundary separating two crystalline domains in copper. A total of 1309 atoms corresponding to 22 atomic layers and subject to periodic boundary conditions in the grain boundary plane were included. The temperature was set to 135 K. The simulation ran over a period of 10 days on 150 computers on average. The simulated time series represents a time interval of 0.1 ms. To obtain the same result with a classical dynamics algorithm (MD) on a 2 GHz PowerPC would require about 15 years of CPU time. A potential function of the EMT form was used to describe the interatomic interactions [3].

Simulations have been carried out starting from two different initial structures. In the first case a narrow grain boundary was constructed by bringing grains with unreconstructed, flat surfaces into contact. In the second case, an amorphous region was placed in between the two grains. The final structure in both cases was very similar. The region of atoms that do not have a local FCC coordination corresponds to about three layers. This thin grain boundary layer is quite consistent with reported experimental measurements on copper grain boundaries [4].

In two independent simulations a distinct annealing event led to the formation of an atom with a local HCP coordination. This is possibly related to an experimentally observed tendency for twisted grain boundaries in gold to contain a domain of HCP coordinated atoms [5].

A remarkable feature of the simulations is the large abundance of transitions where multiple atoms undergo a concerted displacement. Figure 1 shows a histogram of the number of saddle points found where *n* atoms had been displaced by more than 0.5 Å from the adjacent initial state configuration. It would be impossible to construct a complete table of such events in a regular KMC simulation.

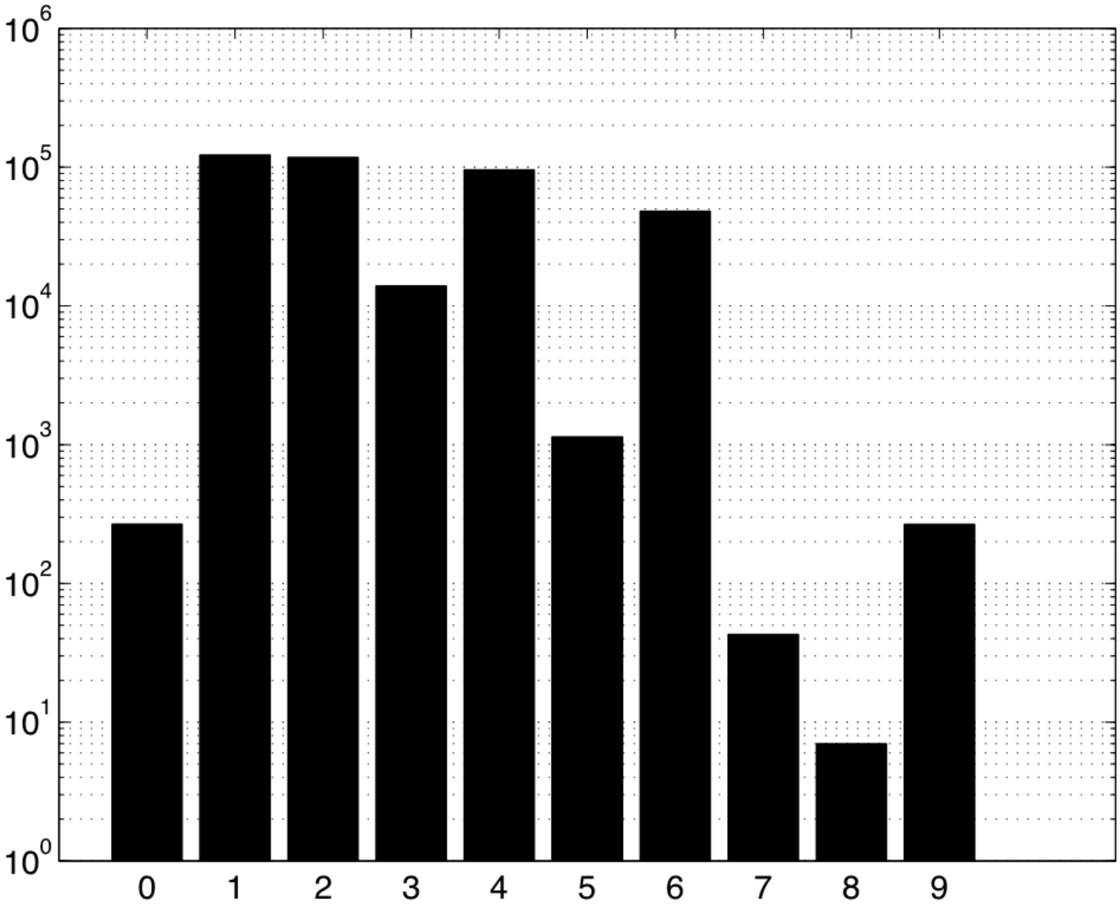

Figure 1, Histogram showing how many atoms where displaced by more than 0.5 Å in going from an initial state to an adjacent saddle point during an AKMC simulation of a Cu grain boundary. The dynamics are dominated by concerted multiatom displacements.

References

(1) G. Henkelman and H. Jónsson, J. Phys. Chem. 115, 9657 (2001).

(2) G. Henkelman and H. Jónsson, J. Phys. Chem. 111, 7010 (1999).

(3) K.W. Jacobsen, P. Stoltze and J.K. Nørskov. Surf. Sci. 366, 394 (1996).

(4) Y. Champion and M.J. Hÿtch, Eur. Phys. 4, 161 (1998).

(5) G. Lucadamo and D.L. Medlin, Science. 300, 1272 (2003).

This work was supported by the Icelandic Research Council (RANNIS).

MULTISCALE MODELING AND SIMULATION OF FLUID FLOWS IN INELASTIC MEDIA

Peter Popov

Institute for Scientific Computation, Texas A&M University, 608N Blocker Bldg., 77843-3404 College Station, United States of America

In this work the problem of upscaling fluid flow in deformable porous media is studied. At the microscale, the physics of flow in deformable porous media is described by the fluid-structure interaction (FSI) problem. Currently, the well-established macroscopic models for poroelasticity can only be applied to linear elastic solids. Furthermore, macroscopic parameters such as average fluid pressure and solid displacements are subject to stringent limitations. In this work numerical upscaling methods based on the stationary FSI problem for deformable nonlinear solid and Stokes flow are developed. The strains in the solid are assumed small but no restrictions are applied on the magnitude of the displacements. The FSI problem is solved numerically by an iterative procedure, which sequentially solves fluid and solid sub-problems. A specific geometry - a long channel with elastic walls - is then considered and an asymptotic solution is derived. The numerical results are shown to coincide with the asymptotics. Further, the asymptotic results is used to obtain an upscaled, Nonlinear Darcy-type equation for the averaged pressure. This result is used to justify a more general 3D hybrid multiscale Finite Element model for flow in a general 3D porous solid subject to large pore-level displacements. Numerical results are presented and extensions to nonlinear histeretic solids are discussed.

Multiscale Modelling of Microstructural Evolution during Dynamic Recrystallisation coupling FEM and CA

Ming Qian, Zheng Xiao Guo

Materials Department, Queen Mary University of London, Mile End Road, London, E1 4NS, United Kingdom

Abstract

Dynamic recrystallization (DRX) is a common phenomenon associated with high temperature plastic deformation of metallic materials of a relatively low-to-medium stacking fault energy. The DRX occurs only when the stress or dislocation density reaches a critical value. Cellular Automata (CA) method is popularly used to simulate the growth of recrystallized grains (R-grains) upon a set of finely meshed grids during the deformation processing. Especially in two-phase materials (e.g., Ti6Al4V), DRX nucleation occurs when the dislocation density accumulation is over the critical value. In order to determine accurately the positions of nucleation of R-grains, a Finite Element (FE) method was combined with the CA simulation. The main task is to couple these two methods on different scale levels. The element length of the FE is around $1-2\times10^{-5}\mu m$, which is almost 10 times of the CA grids ($2\times10^{-6}\mu m$). The idea of coupling can be divided into two parts. First is to directly project the distribution of stress values from FE onto CA grids using a smoothing function supplied by the FE package to meet the requirement of the CA calculation, and then replace the recrystallization part of the strain values of FE element by a value calculated by CA. The current analysis concentrates on the testing of the coupling methods. Even with the limited computing time, the preliminary results show encouraging agreement with experimental findings. The approaches show good promise for such multiscale modelling effort.

Keywords: Dynamic recrystallization, Finite Element method, Cellular Automata method

1 Introduction

Dynamic recrystallization (DRX) occurs during high temperature deformation of some metallic materials. The main phenomena consists nucleation and grain growth, which takes place where the critical deformation condition is reached [1]. In materials with low to medium stacking fault energy, the dislocation density can be accumulated to a high enough level to triger the DRX, because the recovery processes are slow. The grain boundary driving force is from the difference between new grains and the matrix. The growth ceases when the dislocation density reaches equilibrium [2].

High precision prediction is required in manufacture of metal forming processing. Many researches have been done to simulate the DRX effects on metallic softening by using FEM[3, 4, 5]. But almost every simulation uses constitutive equations to represent the microstructure effect on strain-stress curves, which based on the assumption that the softening caused by DRX takes effect immediately when the deformation condition changes.

These simulation ignored the dynamic mechanism of grain growth. In order to consider the dyniamic microstructure evolution effect, a new coupling method is invited in this paper.

Cellualr Automata (CA) is wildly used method on microstructure simulation in materials science area. The microstructure changes of either recrystalliztion and dynamic recrystallization have also been studied by many researchers [6, 7, 8, 9]. CA has been proved to be a very promising method to simulate the grain structure changes. If CA can be coupled with FEM to supply more microstructure evolution information, a coupling method will become very practically useful for manufacture processing design.

2 Model of Coupling Simulation

The hot deformation of metal can be considered as a combination effect of hardening and softening processing occuring at same time. In this model, the hardening part is simulated by using Finite Element Method, and the softening processing is done by using Cellular Automata Method. The detail of FEM model, CA model and how to couple will be expressed in the following separate sections.

2.1 FEM model

The role of FEM package in this simulation is to predict strain stress distribution caused by the work-hardening effect on two phases materials. But in order to consider the work-softening effect, which is DRX simulated by using CA in this case, the total strain rate is described as

$$\dot{\varepsilon} = \dot{\varepsilon}^e + \dot{\varepsilon}^p + \dot{\varepsilon}^c \tag{1}$$

where $\dot{\varepsilon}$ is the total strain rate, and $\dot{\varepsilon}^e$, $\dot{\varepsilon}^p$ and $\dot{\varepsilon}^c$ represent the elastic part, plastic part and softening part caused by DRX, respectively. As it is conventionally believed that the hot work hardening is rate dependent, we also use a rate dependent model to describe the plastic strain rate changes as

$$\dot{\varepsilon}^p_{eff} = \dot{\varepsilon}_{eff} \cdot \left[1 - \left(\frac{1}{\sigma_{eff}/E + 1}\right)^m\right] \tag{2}$$

where $\dot{\varepsilon}^p_{eff}$ is the effective plastic strain rate, and $\dot{\varepsilon}_{eff}$, σ_{eff}, E are effective strain rate, effective stress and Elastic modulus, respectively. m is a rate dependent variable, which differs from 20 to 100 according to different materials. In this simulation, it is set to be 50. And now the plastic strain rate tensor $\dot{\varepsilon}_{ij}$ can be given from

$$\dot{\varepsilon}^p_{ij} = \frac{3\dot{\varepsilon}^p_{eff}}{2\sigma_{eff}}\sigma'_{ij} \tag{3}$$

where σ'_{ij} is the deviatoric stress tensor.

The DRX part of strain rate tensor $\dot{\varepsilon}^c_{ij}$ controls the changing of softening strain caused by DRX. In order to avoid the suddent change of the strain, it is set to be a time dependent function:

$$\dot{\varepsilon}^c_{ij}(t) = \frac{\varepsilon^e_{ij}(t_0)}{\Delta t} \sec h^2 \left(\frac{t - t_0}{\Delta t} \right) \tag{4}$$

where $\varepsilon^e_{ij}(t_0)$ represents the elastic strain tensor at certain time t_0, and δt is the time length of one strain softening processing step. In this case, t_0, the point of nucleation time for each DRX-grain, differs from points to points. The reason of using function $sech^2(x)$ is that the integration of this function equals 1. So the total effect of softening amplitude will be no more than the elastic part of strain at the point of nucleation time.

2.2 CA model

As dislocation density is considered to play a very important role in the nucleation and grain growth of DRX, it is set to be a key variable in CA simulation to evalue the microstructure evolution. This CA model has been developed and validated by Ding [7] and Qian [6]. It is worthy to remind the key part of the model. The flow stress is assumed to be proportional to the square root of dislocation density [10] as:

$$\sigma = \alpha \mu b \sqrt{\rho} \tag{5}$$

The critical dislocation ρ_c trigers the onset of DRX nucleation. It can be derived from the energy difference and deformation conditions by [11]:

$$\rho_c = \left(\frac{20 \gamma_i \dot{\varepsilon}}{3 b l M \tau^2} \right)^{1/3} \tag{6}$$

where γ_i, the grain boundary energy, b, Burger's vector, l, the dislocation mean free path, M, the grain boundary mobility, and τ, the dislocation line energy, are independent to the time t. The nucleation rate $\dot{n}$ is set to be a probability of the number of "ready for nucleation" grain boundary cell.

The driving force of DRX grain, F_i is a function of the difference of dislocation density between DRX grain and matrix, $\delta \rho_i$:

$$F_i = 4\pi r_i^2 \tau \Delta\rho - 8\pi r_i \gamma_i \tag{7}$$

And the boundary growing velocity can be calculated from:

$$V_i = M F_i (4\pi r_i^2) \tag{8}$$

where M is the boundary mobility.

2.3 Coupling FEM and CA

The goal of coupling of FEM and CA is to simulate the microstructure evolution more accurately, especially at nucleation stage. It is designed to use FEM simulation to locate where the cells are "mature" enough to process the nucleation. And as long as FEM locates the cells, CA takes over the job of simulate how nucleation sites are selected and grains grow. As some of the nucleation and grain growth procedures can not be expressed by continuous functions, the CA package is running explicitly. The data transferring between FEM and CA are mainly stain tensor, stress tensor and time. All the necessary data for FEM to start simulation from CA are shown in Equ.4, that is the strain tensor at nucleation time and the time of nucleation. Equ.4 controls $\dot{\varepsilon}^c_{ij}$, and finally the stress reduction will take place where $\dot{\varepsilon}^e_{ij}$ represents the stress in Equ.1.

Each simulation of deformation is divided into small straining steps. After each straining step simulated in FEM, stress and strain tensor is projected onto a finer CA grid. CA cells perform the nucleation condition judging and possibly grain growth afterwards. And then according to the CA results of straining, the necessary change of $\varepsilon^e_{ij}(t_0)$ and t_0 in FEM is updated. When the FEM initial condition is updated, a further straining will be applied. This is the procedure of one coupling loop. The straining step is 0.01, and the deformation condition is assumed to be isothermal and equilibrium for each single simulation.

3 Results and Discussion

Fig.2 is one set of the typical CA simulated DRX microstructure evolution configurations. The specimen contains 20 grains at initial state, and 5 of them are α phase and rest are β phase. The DRX nucleation is only allowed to take place on $\beta-\beta$ or $\alpha-\beta$ phase boundaries.

Fig.3 shows the strain stress curves at different strain rate under $1123K$. The occurrence of DRX is earlier at lower strain rate. But the stress softening effect is larger for higher strain rate. In the view of microstructure evolution, this has an explanation, that is: at lower strain rate, the grains grow earlier and faster, and after a certain time the grain boundaries are all occupied by DRX grains and no further DRX softening can take place. The elastic strain ε^e at the time of nucleation occurrence is lower. According to Eqn.4, the $\dot{\varepsilon}^c_{ij}$ is smaller if the $\varepsilon^e(t)$ is smaller.

Fig.**??** shows the strain stress curves at strain rate 0.02_{-1} under different temperatures. The similar phenomenon is found as strain rate effects. Higher temperature triggers DRX more easily. But the reduction of stress is lower at higher temperature. And after DRX grain ceases growing, the work-hardening becomes the dominating contribution to the stress increasing. But DRX delays the hardening processes.

4 Conclusion

The coupled FEM and CA method is capable to simulate both microstructure evolution and strain-stress behaviour of Dynamic Recrystalliztion. Temperature and strain rate effects on nucleation critical condition is well simulated. Without considering metallic work-softening, DRX is the major softening mechanism of plastic deformation in some metals. DRX reduces the stress by delaying the work-hardening processes, but can't stop hardening after DRX ceases.

References

[1] F. J. Humphreys, M. Hatherly, *Recrystallization and Related Annealing Phenomena*, Pergamon, Oxford, p.369

[2] T. Sakai, J. J. Jonas, *Acta Metall.*, **32**(1984), 189

[3] M. Wang, X. Li, F. Du, Y. Zheng, *Materials Science and Engineering A*, **379**(2004), 133-140

[4] M. Goerdeler, M. Crumbach, M. Schneider, G. Gottstein, L. Neumann, H. Aretz, R. Kopp, *Materials Science and Engineering A*, **387**(2004), 266-271

[5] N. Bontcheva, G. Petzov, *Computational Materials Science*, **28**(2003), 563-573

[6] M. Qian, Z.X. Guo, *Materials Science and Engineering A*, **365**(2004), 180-185

[7] R. Ding, Z.X. Guo *Materials Science and Engineering A*, **365**(2004), 172-179

[8] D. Raabe, *Computational Materials Science* **19**(2000), 13-26

[9] R.L. Goetz, V. Seetharaman, *Scripta Materialia*, **38**(1998), 405-413

[10] H. Mecking, U. F. Kocks, *Acta Metall.*, **29**(1981), 1865

[11] W. Roberts, B. Ahlblom, *Acta metall.*, **26**(1978), 801

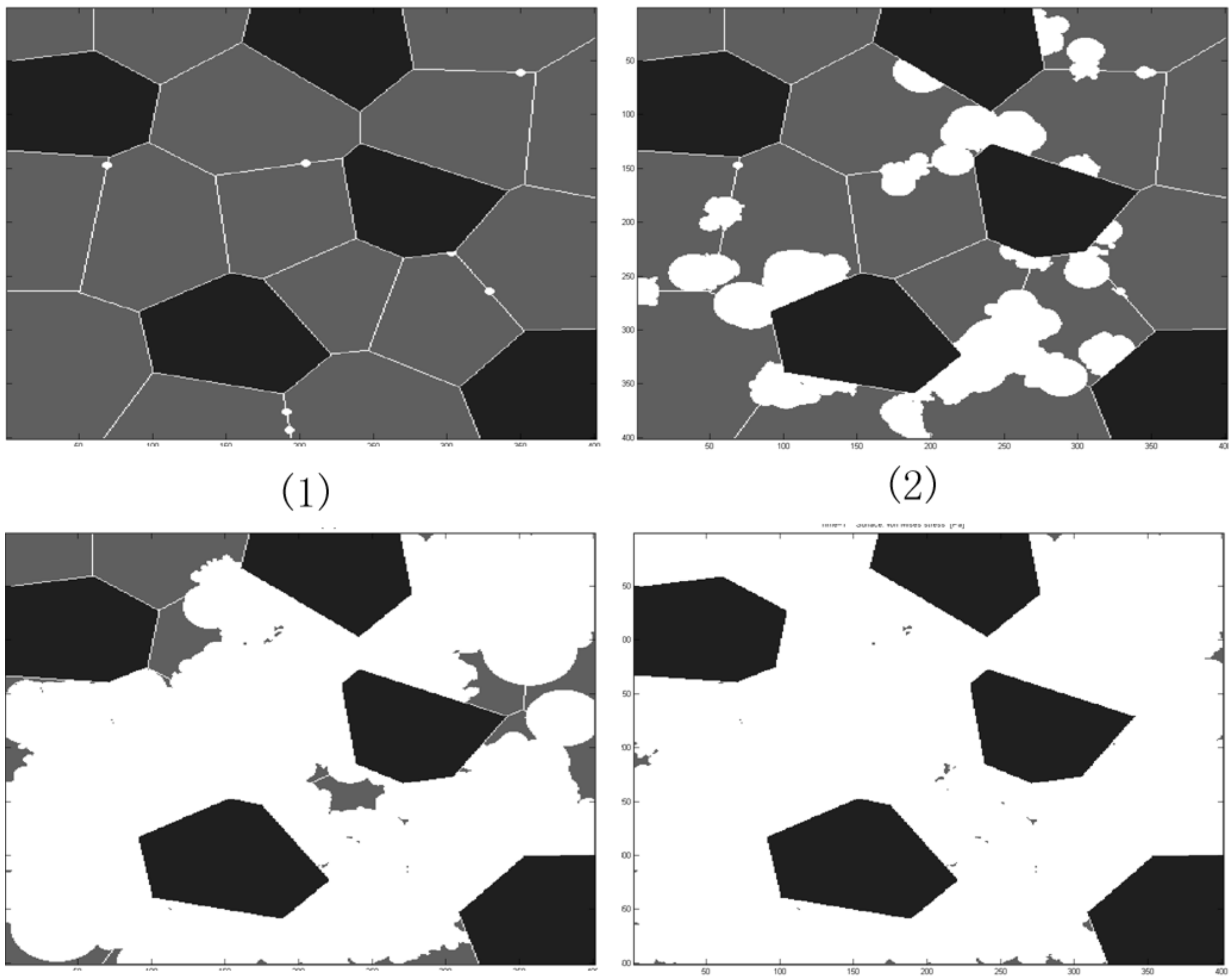

(1)

(2)

(3)

(4)

Figure 1: Microstructure evolution under strain rate 0.02^{-1} and temperature $1123K$ at strain 0.01, 0.05, 0.1 and 0.15 (black - α phase; gray - β phase; white - DRX grain).

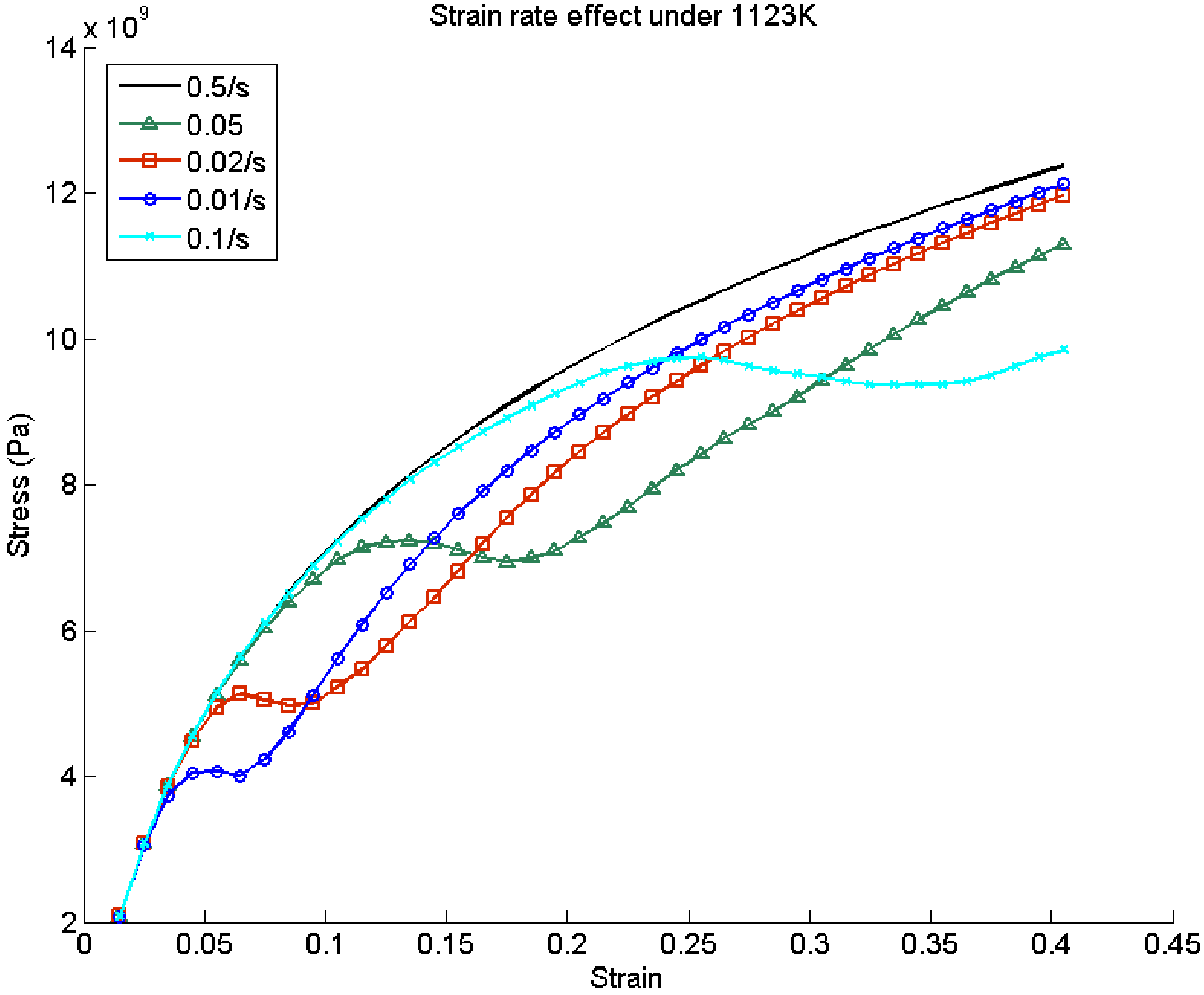

Figure 2: Strain stress curves under $1123K$ at strain rate 0.01^{-1}, 0.02^{-1}, 0.05^{-1}, 0.1^{-1} and 0.5^{-1}.

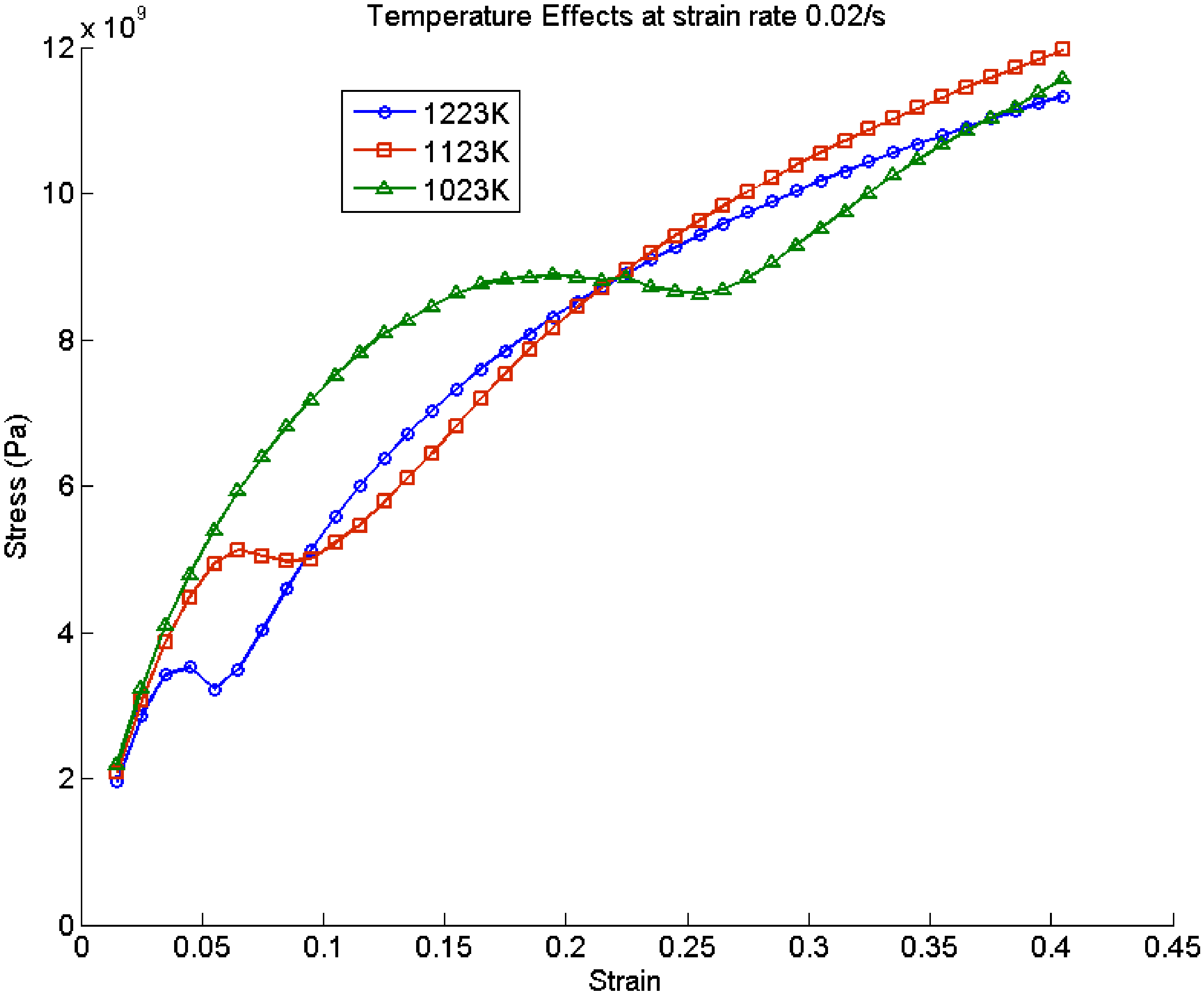

Figure 3: Strain stress curves at strain rate 0.02^{-1} under temperature $1023K$, $1123K$ and $1223K$.

Trends in the energetics of non-magnetic bcc transition metals

Ting Qin [1], Ralf Drautz [2], David Pettifor [2]

[1]Mansfield College, Mansfield College, OX1 3TF, Oxford, United Kingdom
[2]Department of Materials, Mansfield College, OX1 3TF, Oxford, United Kingdom

We present an ab initio study of the bcc transition metals V, Nb, Ta, Cr, Mo and W. For each element, we calculated the energy and elastic constants with respect to fifty structures types, including most of the metallic structure types existing in nature as well as some common non-metallic structure types plus interstitial and vacancy data. We find a surprisingly simple empirical relation between the calculated cohesive energy and the product of the bulk modulus with the cube root of the atomic volume. We demonstrate that a simple nearest-neighbour second-moment model is unable to explain this trend and discuss the requirements in order that an interatomic potential can reproduce the empirical relation. In particular, the relation clearly illustrates that the local density and generalized gradient approximation for exchange and correlation behave differently. This means that the common practice of fitting interatomic potentials to literature data that include LDA as well as GGA calculations should be reconsidered as the resulting potentials are unable to reproduce the trend found from our ab initio calculations.

A Multiscale Model Of The Si CVD Process

Authors: Maurizio Rondanini[1], Alessandro Barbato[2], Carlo Cavallotti[3]

Affiliations: Dipartimento di Chimica, Materiali e Ingegneria Chimica "Giulio Natta", Politecnico di Milano, via Mancinelli 7 20131 Milano, Italy, [1]maurizio.rondanini@polimi.it; [2]alessandro.barbato@polimi.it; [3]carlo.cavallotti@polimi.it

ABSTRACT

Chemical Vapor Deposition (CVD) is a chemical process widely adopted in the semiconductor industry for the deposition of thin films of various materials, among which silicon. Quality and morphology of the deposited films depend on reactor fluid dynamics, surface chemistry and both gas phase and surface diffusive phenomena. Many models can describe these events singularly at their typical length scale, but a significant task is still to be able to link all of them in a unique predictive model. In this framework, we present a multiscale approach meant to describe the film morphological evolution at different time and length scales. Fluid dynamics and overall mass and energy balance are solved with the finite elements method in 2 dimensions while the morphological evolution of the film is investigated with 3D kinetic Monte Carlo. The two models are linked together by imposing continuity of gas phase concentration and fluxes at the boundary that is common to the domain of both models. In order to obtain a stable convergent scheme, information about the sensitivity of the microscale are incorporated into the reactor scale calculations by computing the Jacobian contribution at the reactor-surface boundary. This method allows self-consistent computations of gas-phase species concentration and fluxes between the different domains.

We have then focused our attention on the role played by diffusive phenomena in the growth morphology of the film. Our KMC simulations show in fact how an essential role in the microscale is played by the amount of gaseous reactant fluxes hitting the surface and by the diffusive dynamics of adsorbed species. In particular the quantity of atomic hydrogen adsorbed and the interactions between Si ad-dimers appear to play a significant part in the morphological transition from an order terrace step flow growth to a disordered 3 dimensional growth regime.

1. Introduction

The chemical vapor deposition (CVD) of silicon thin solid films is at the basis of the microelectronic industry, as it is a crucial stage for the manufacturing of many electronic devices. The comprehension of the main features characterizing its growth is fundamental in order to improve the quality of the deposited film, but it is complicated by chemical and physical events occurring at length scales differing for even some orders of magnitudes.

In this framework the development of a model able to predict film properties (growth rate, morphological evolution of the surface,…) as a function of operative conditions (temperature, pressure, reactants flux and chemical composition,…) can give an important contribution to the advance of the silicon deposition technology.

2. Multiscale Model

The multiscale approach here described is meant to investigate the influence that gas phase and surface reactions have on the morphological and compositional evolution of thin solid films deposited by chemical vapour deposition (CVD). Atomic scale energetic and kinetic parameters, when not available from the literature, were estimated by means of quantum chemistry computations. The local gas-phase composition, fluid dynamics and thermal fields were calculated by integration of mass, energy and momentum equations at the reactor scale using kinetic and thermodynamic data determined with quantum chemistry. The morphology of the film is finally investigated using 3D Kinetic Monte Carlo simulations, whose inputs are the gas-phase fluxes calculated at the reactor scale and the kinetic parameters determined at the atomic scale.

1.1 Macroscale: reactor modeling

At this scale the approach consists in the evaluation of flow and temperature fields and reactants distribution within the reactor through classical conservation equations of the chemical reaction engineering (i.e., continuity, momentum and energy conservation equations together with the mass conservation for the gas phase species). An important result of the simulation is the growth rate profile on the wafer and the gas temperature 2D field within the reactor. Two points are very important to obtain reliable macroscale simulations: the adopted parameters (rates of involved chemical reactions, thermodynamic and transport features of the gaseous mixture) and the detailed description of the reactor geometry. Mass, energy and momentum conservation equations are solved employing a two-dimensional Finite Element Method (FEM).

1.2 Microscale: surface morphological evolution

For this scale of the system we choose to investigate the morphological evolution of the thin solid films with 3D Kinetic Monte Carlo, that has the advantage over other models to require as inputs kinetic constants or diffusion parameters that can be directly calculated by means of quantum chemistry. Our implementation of Kinetic Monte Carlo (KMC) follows the theory outlined by Fichthorn and Weinberg [1], with direct tracking of real-time and a rejection-free choice of the random transition. The starting conditions of the KMC simulation are the surface structure at time 0, the surface temperature and the fluxes of gas-phase species towards the surface. The output of a KMC simulation gives the detailed surface morphology of the film after the deposition of a certain amount of layers.
It is thus possible to determine the growth regime of the film, be it 3D, terrace step flow or 2D.

1.3 Linking of different models

The first step of a calculation consists in the simulation at the reactor scale, in order to obtain a starting point for the microscale. The next step involves KMC calculations run separately for a predetermined number of points of the growth surface. It is important to point out that each one of these points corresponds to a point of the FEM mesh. Calculated adsorption flux are then passed back to the reactor scale and from this point FEM and KMC models are solved iteratively until convergence is achieved. To improve convergence, the contribution of the KMC boundary condition to the FEM Jacobian was evaluated numerically, as proposed by Nemirovskaya [2]. Finally computed gas phase fluxes are is averaged on several nodes to decrease the statistical error. This method can be made particularly efficient if KMC computations are run in parallel, thus reducing the computational burden of n times, where n represents the number of mesh points that constitute the interface between macroscopic and microscopic scale.

The two models are coupled imposing the continuity of the gas fluxes at the interface between the reactor and the portion of the susceptor on which the Monte Carlo Kinetic (KMC) computation is performed. Thus the KMC model appears as a Neumann boundary condition to the fluid dynamic reactor model.

3. Simulations

In order to show how our models work and which information can be obtained from simulations, some significant results taken from various investigated cases will be reported further below in this section.

3.1 Reactor scale

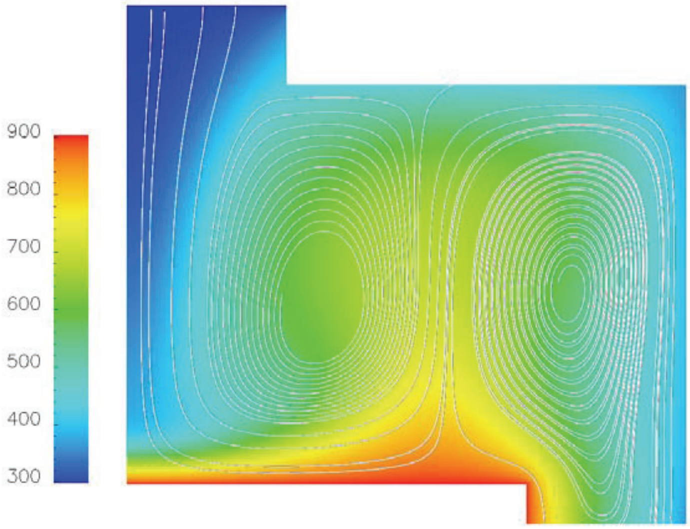

Figure 1. Simulation of a vertical axysymmetrical reactor showing flux lines. Background colours represent the temperature field.

In Fig.1 is displayed a calculation for a vertical axysymmetrical reactor in which gaseous precursors are fed from above and the susceptor (i.e.: the surface on which silicon is deposited) is located at the lower side of the reactor. For this geometry our simulations allow to examine the particular fluid dynamical behaviour of the gas current, which creates a double vortex probably because of convective phenomena due to the high temperature of the substrate. The temperature field itself can be seen for this case with the help of background colours that are related to the scale (expressed in Kelvin) placed at the left of the picture. This kind of simulations is often used to set up the geometry of the reactor to obtain the best fluid-dynamical configuration.

3.2 Microscale

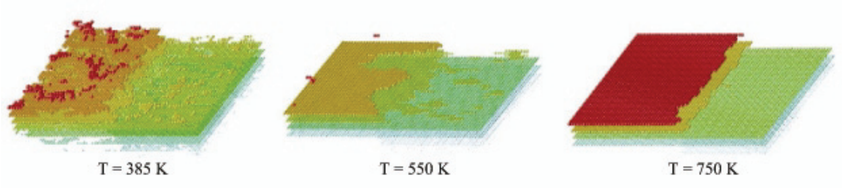

Figure 2. Calculated Si surface morphology for a SiH_4 gas phase flux of 1 ML/s after the deposition of 4 ML at different temperatures.

In Fig. 2 are reported calculations for the deposition of Si in the absence of hydrogen at different surface temperatures performed with the KMC model. These simulations allow to examine the morphological evolution of the surface with particular attention to the growth regime. These data are particularly functional to determine the quality of the Si film growth.

3.3 Coupled system

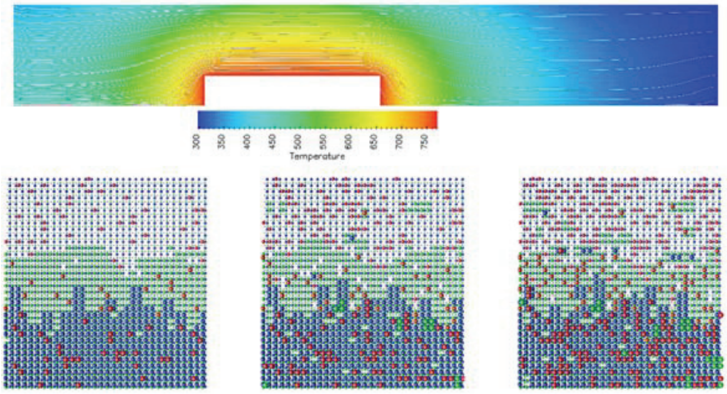

Figure 3. Reactor scheme(above) and 3 images of the temporal evolution of the Si surface (green and blue spheres) with hydrogen adsorbed (red spheres).

In Fig.3 we report calculations performed with coupled macroscale and microscale models. Below the sketch of the horizontal reactor, the 3 images represent a top view of the surface where red spots stand for hydrogen adatoms, while blue and green spheres correspond to Si atoms belonging to even and odd planes. These images reproduce the temporal evolution of the growth surface, giving useful information particularly about the transition from an order terrace step flow growth regime to a disordered three-dimensional growth regime. This morphological transition seems significantly influenced by the amount of the H atoms adsorbed on the surface.

References

[1] K.A. Fichthorn, W.H. Weinberg, J. Chem. Phys. **95**, (1991) 1090
[2] M. Nemirovskaya, PhD Thesis, *Multiscale modeling strategies for chemical vapor deposition*, MIT, 2002.

Relaxation of Semiconductor Nanostructures using Molecular Dynamics with Analytic Bond Order Potentials

Kurt Scheerschmidt and Volker Kuhlmann

Max Planck Institute of Microstructure Physics, Weinberg 2, D-06120 Halle, Germany
Email: *schee@mpi-halle.de*

Summary. Molecular dynamics simulations using empirical potentials have been performed to describe atomic interactions during the relaxation of nanostructures. To include the quantum mechanical nature of atomic bonding a tight-binding based bond order potential is developed applying analytically the most important momenta up to 6th order. The applicability of the bond order potential and resulting enhancements in structural predictions are analyzed recalculating quantum dot relaxations and interface defects arising during bonding of two wafers with twist rotation misalignment.

1 Introduction

Molecular dynamics (MD) simulations have been performed to study atomic processes related to the reordering at interfaces and relaxation of nanostructures [1]. To enhance MD, we use the bond order potential (BOP) based on the tight binding (TB) model, as it preserves the essential quantum mechanical nature of atomic bonding, yet abandons the electronic degree of freedom. Just like *ab initio* methods, TB calculations require complete diagonalisation of the Hamiltonian, which scales as $\mathcal{O}(N^3)$ and restricts simulations to a few thousand atoms. The analytic BOP, however, achieves $\mathcal{O}(N)$ scaling by diagonalizing the orthogonal TB-Hamiltonian approximately and is recognized as a fast and accurate model for atomic interaction [2, 3]. It allows to explore the dynamics of systems on macroscopic time and length scales on the atomic level that are beyond the realm of *ab initio* calculations. Thus enhanced empirical TB based potentials make a sufficiently large number of particles and relaxation times up to μs accessible by MD including the electronic structure and the nature of the covalent bonds indirectly. The ability of the BOP based MD is demonstrated here by comparing relaxations of quantum dots and interface structures with those using Tersoff potentials.

2 Analytic bond order potentials up to 6th moments

The approximations to develop analytic BOP potentials from DFT may be summarized by the following steps (for details cf. [2, 3] and for the extensions cf. [4]): construct the TB matrix elements by Slater-Koster two-centre integrals including s- and p- orbitals, transform the matrix to the bond representation, replace the diagonalization by Lanczos recursion, obtain the momenta from the continued fraction representation of the Green function up to order n for an analytic BOPn potential. The total cohesive potential energy U_{coh} has three contributions: pair repulsion, promotion energy U_{prom}, and bond energy as excess of the band energy over the individual atomic interactions $U_{bond} = 2\sum_{i\alpha,j\beta}\Theta_{j\beta,i\alpha}H_{i\alpha,j\beta}$. In the BOP representation the matrix elements $H_{i\alpha,j\beta}$ are replaced by the Slater-Koster two-center integrals h_{ij} and the Goodwin-Skinner-Pettifor distance scaling function. The bond order $\Theta_{i\sigma,j\sigma}$ is equivalent to the electron density for which a concise analytical expression $\left[1+\frac{N^2(\Phi^i_{2\sigma}+\Phi^j_{2\sigma})+\Phi^i_{2\sigma}\Phi^j_{2\sigma}(2N+\triangle\Phi_{4\sigma})}{(N+\triangle\Phi_{4\sigma})^2}\right]^{-1/2}$ can be given that employs the normalized second and fourth moment $(\Phi_{2\sigma}, \Phi_{4\sigma})$ of the local density of electronic states and $\triangle\Phi_{4\sigma} = (\Phi^i_{4\sigma} + \Phi^j_{4\sigma} - \Phi^{i2}_{2\sigma} - \Phi^{j2}_{2\sigma})/(\Phi^i_{2\sigma} + \Phi^j_{2\sigma})$, $N^2 = \triangle\Phi_{4\sigma} + \Phi^i_{2\sigma}\Phi^j_{2\sigma})$. The contribution $\Phi_{4\sigma}$ to the 4^{th} moment was given in terms of the matrix-elements of the tight binding Hamiltonian,

$$\sum_{k(i)\neq j} \hat{h}^4_{ik} g^2_{jik}, \qquad \sum_{\substack{k(i)\neq j\\ k'(k)\neq i,j}} \hat{h}^2_{ik}\hat{h}^2_{kk'} g^2_{jik} g^2_{ikk'}, \qquad {\sum_{k(i),k'(i)\neq j}}' \hat{h}^2_{ik}\hat{h}^2_{ik'} g_{jik} g_{kik'} g_{ik'},$$

with the cosine of the bond angle $\mathcal{C}_{jik}$, the angular function $g_{ijk} = (1 + \hat{p}_i\mathcal{C}_{jik})/(1 + \hat{p}_i)$, reduced TB-parameters $\hat{p}_i = h_{pp\sigma}/h_{ss\sigma}$, and normalized hopping integrals $\hat{h}_{ik} = h_{ik}/h_{ij}$ etc.

The resulting semi-empirical many body potential is transferable to describe phases and configurations not included in the parameter fit, a feature not found in other empirical potentials. Moreover, transferability extends to different kinds of materials, where only the parameter need to be refitted. In the implementation of the enhanced BOP4+ a number of angular terms are included that are related to certain π bonds between neighboring atoms and contribute up to 40%, but were ignored previously. Both contributions exhibit new angular dependencies, different from those already accounted for in the expressions given in [2] and the second order BOP2 [5]. With the angle of torsion $\mathcal{C}_{ij,kk'}$ and the abbreviations $\mathcal{Z} = \mathcal{C}_{ij,kk'} + \mathcal{C}_{jik}\mathcal{C}_{ikk'}$ and $\xi = \hat{\pi}_i \hat{p}_k/(1+\hat{p}_i)$ one yields the new contribution to the 4-th momentum:

$$\sum_{\substack{k(i)\neq j \\ k'(k)\neq i,j}} \hat{h}_{ik}^2 \hat{h}_{kk'}^2 \mathcal{Z}\xi \left(\frac{\mathcal{Z}\xi}{(1+\hat{p}_k)^2} + \frac{2 g_{jik} g_{ikk'}}{1+\hat{p}_k} \right).$$

Similarly on-site contributions to $\Phi_{4\sigma}$ proportional to the energy splitting δ_i are included:

$$\sum \hat{h}_{ik}^2 \left\{ g_{jik}(2\hat{\delta}_i^2 + \hat{\delta}_k^2) + \hat{p}_i \hat{\delta}_i^2 \frac{(1-\mathcal{C}_{jik})^2}{(1+\hat{p}_i)^2} \right\} + \hat{\delta}_i^4.$$

The improved BOP4+ allows nanoscopic structure calculations including electronic properties. Besides an accurate fit, the BOP requires well parameterized TB matrix elements or parameter optimizing, and the problem of transferability have to be considered separately. For BOP of order n = 2 [5] the bond-order term looks like a Tersoff potential and the numerical behavior of BOP2 and the empirical Tersoff potential are approximately equivalent. The details for the enhanced analytic BOP4+ [4] will be given elsewhere, complicated angular terms occur, reflecting the non-radial electronic structure of the bonds.

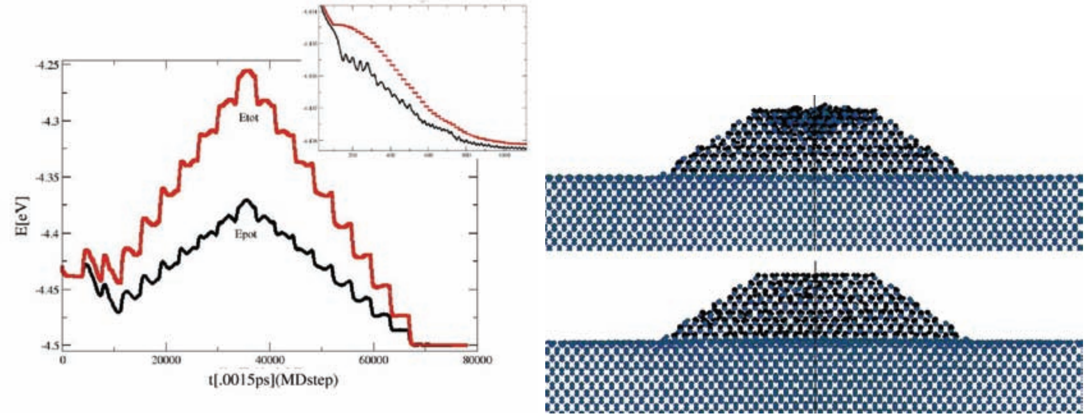

(a) (b)

Fig. 1. MD relaxation of an SiGe/Si island: (a) Potential and total energy during annealing up to 900K, inset: enlarged first 1000 steps relaxing start configuration at 0K, (b) 110 views after annealing with a Tersoff potential (top) and an analytical BOP4+ (bottom).

3 BOP4+ in MD relaxation of quantum dots

A quantum dot (QD) is a nanometer scaled island or region of suitable material free-standing on or embedded in semiconductor or other matrices. Especially shape, size and strain field of single QDs as well as quality, density, and homogeneity of equisized and equishaped dot arrangements are important features which control the optical properties, the emission and absorption of light, the lasing efficiency, etc. MD with suitable potentials allows to describe the relaxation and to predict structural properties of QDs.

Fig. 1 (a) shows the behavior of the potential and the total energy of a SiGe/Si-island and Fig. 1 (b) the structural difference after relaxing the system up to 900K with Tersoff and BOP4+ potentials, respectively. Due to the different next and overnext relations - hopping matrix elements up to 6th order - the better stiffness of the BOP4+ yields better structural stability.

4 BOP4+ in MD investigations of wafer bonded interfaces

Wafer bonding, i.e. the creation of interfaces by joining two wafer surfaces, has become an attractive method for many practical applications in microelectronics, micromechanics or optoelectronics. The macroscopic properties of bonded materials are mainly determined by the atomic processes at the interfaces during the transition from adhesion to chemical bonding. Thus, the description of the atomic processes is of increasing interest to support the experimental investigations or to predict the bonding behavior. Whereas bonding of two perfectly aligned, identical wafers yields a single, perfectly bonded wafer without defects, miscut of the wafer results in steps on the wafer surfaces and thus edge dislocations at the bonded interfaces are created. Bonding wafers with rotational twist leads additionally to a network of screw dislocations at the interface, in dependence of the twist angle different bonding behavior is observed as discussed in detail, e.g., in [6]. A special situation is the 90° twist, e.g. between monoatomic steps, giving a (2x2) reconstructed interface and consisting of structural units called the $\overline{4}2m$-dreidl [7]. The dreidl structure is found to be also the minimum energy configuration in DFT-LDA simulations. All interface relaxations, however, are strongly influenced by the atomic potential model used, as it is demonstrated in Figs. 2-4 comparing MD interface simulations with Tersoff and BOP4+, respectively. Figs. 2 and 3 show the resulting minimum structures gained for higher annealing temperatures (900K) of a wafer bonded interface with a twist rotation of 2.8°. The [001]-projections of the bonds normal to the bonded interface up to overnext neighbors is given in Figs. 2 (a) and (b) for the MD relaxation with Tersoff and BOP4+ potentials, respectively. In Fig. 3 the [110] projection is shown, with both the Tersoff and the BOP4+ simulation projected by different colors into the same view. One reveals the more located imperfectly bonded regions around the screw dislocations for the Tersoff potential, whereas the relaxation with BOP4+ yield more stability due to the higher potential stiffness according to the 6th moment

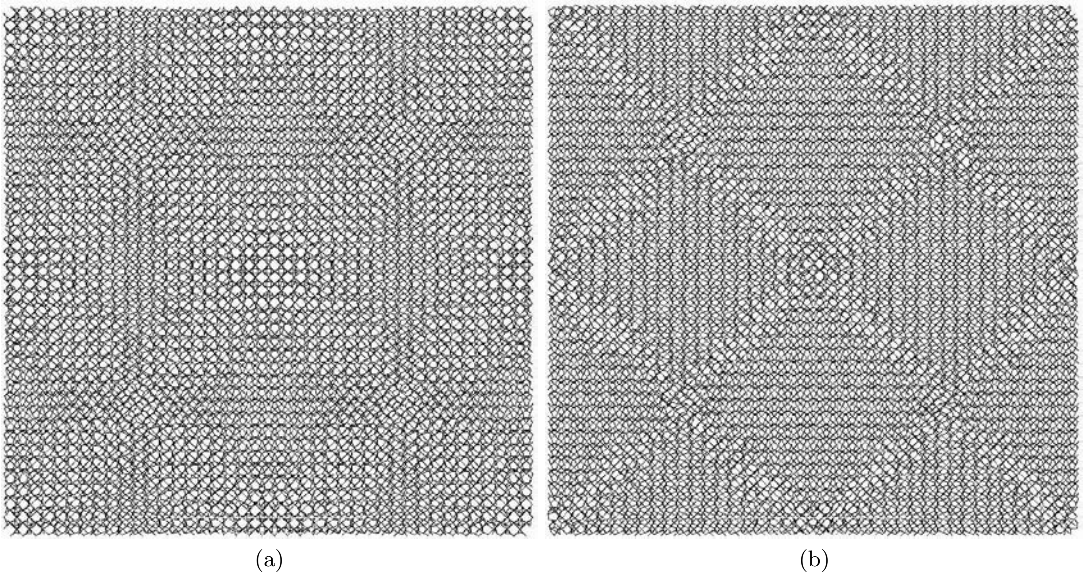

(a) (b)

Fig. 2. MD simulated structural models of bonded wafers ([001] views, bond representation of 3 lattice planes around the interface) with rotationally 2.8° twist angles (134500 atoms, 22nm box) annealed at 900K for orthogonal dimer start configurations: (a) Tersoff potential; (b) BOP4+ potential.

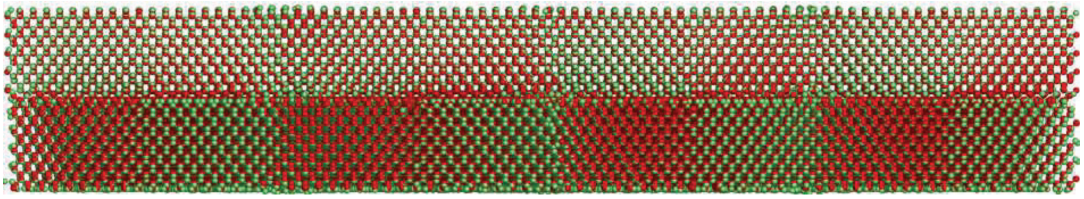

Fig. 3. MD relaxation of bonding rotationally twisted wafers ([110] view) with 2.8° angle, 22nm box, orthogonal dimers: structural difference using Tersoff (green) and BOP4+ potentials (red).

hopping terms. Finally, in Fig. 4 the pair-, bond angle-, and torsion angle distributions are shown for the 2.8°-twist bonded interface, only 3 lattice planes around the interface are considered in distance and angle counting. The Tersoff potential yields the characteristic first and second neighbor distances as well as the bond angle of 109°. The calculation with the BOP4+ demonstrates the characteristic deviations due to the better description of the electronic bond structure. So, for instance, the Tersoff potential is defined without torsion, thus the corresponding distribution in Fig. 4 (c) has no relevant peaks. However, the angular distribution Fig. 4 (b) shows remarkable maxima at 95° and 125°.

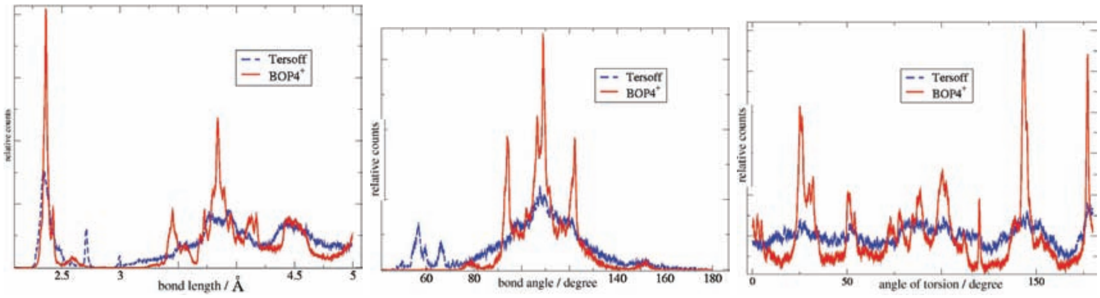

(a) (b) (c)

Fig. 4. Distribution functions for MD simulated structural models of bonded wafers with rotationally twist angle of 2.8° annealed at 900K assuming Tersoff potential (blue) and BOP4+ potential (red): (a) radial distribution function, (b) bond angles, and (c) torsion angles.

5 Conclusions

Molecular dynamics simulations (MD) based on empirical potentials are used to investigate the relaxation of nanostructures. It is demonstrated that different final structures for different potentials occur in simulating, e.g., quantum dot relaxations or the bonding of two Si(001) wafers rotationally misaligned. The angular and distance behavior near defects shows the better electronic potential structure for the enhanced BOP4 potential. It clearly demonstrates the importance of enhanced empirical potentials as it is given by the tight-binding based analytic bond-order potential BOP4+ up to 6th order momenta.

References

1. K. Scheerschmidt and P. Werner, in: *Nano-Optoelectronics: Concepts, Physics and Devices*, Springer, p.67-98, (2002); K. Scheerschmidt and V. Kuhlmann, Interface Science 12, 157 (2004).
2. A.P. Horsfield, A.M. Bratkovsky, M. Fearn, D.G. Pettifor, and M. Aoki, Phys. Rev. B 53, 12694 (1996); D.G. Pettifor, M.W. Finnis, D. Nguyen-Manh, D.A. Murdick, X.W. Zhou, and H.N.G. Wadley, Mater. Sci. Eng., A 365, 2 (2004).
3. M.W. Finnis: *Interatomic Forces in Condensed Matter*, Oxford Series on Materials Modelling (Oxford University Press, Oxford, 2003).
4. V. Kuhlmann, Thesis, Martin-Luther-Universität, Halle (2006).
5. D. Conrad and K. Scheerschmidt, Phys. Rev. B **58**, 4538 (1998); K. Scheerschmidt, D. Conrad, and A. Belov, Comput. Mater. Sci.**24** (2002) 33.
6. K. Scheerschmidt, MRS Proceedings Volume **681E** (2002), I2.3.
7. A.Y. Belov, D. Conrad, K. Scheerschmidt, and U. Gösele, Philos. Magazine A**77**, 55 (1998); A.Y. Belov, K. Scheerschmidt, and U. Gösele, phys. status solidi (a) **159**, 171 (1999); K. Scheerschmidt, D. Conrad, A. Belov, Comput. Mater. Sci. **24**, 33 (2002).

Examples of Electron Microscopy Observations at Different Length Scales

Dominique Schryvers[1], Wim Tirry[1], Zhiqing Yang[1], Barbora Bartova[1], Silvia Ignacova[2], Shanshan Cao[1], Arvind Srivastava[1]

[1]**Electron Microscopy for Materials Science (EMAT), University of Antwerp (UA), Groenenborgerlaan 171, B-2020 Antwerp, Belgium, nick.schryvers@ua.ac.be**
[2]**Institue of Physics, Academy of Sciences, Prague, 18221, Czech Republic**

ABSTRACT

The present contribution will focus on recent transmission electron microscopy observations of structures at different length scales in materials undergoing phase transformations. The examples are chosen so as to provide links to possible mathematical models describing these features at their respective length scales. The latter range from the atomic scale when dealing with atomic structures over the nanoscale when looking at structural defects such as twin boundaries to the micron scale when talking about domain structures. An example of the first is the refinement of the atomic structure of the Ni_4Ti_3 precipitate formed in Ni-rich Ni-Ti alloys to enhance the shape memory behaviour, the 3D configuration of these precipitates an example of the last. Some other examples will be shown as well.

1. Introduction

When attempting to model real life structures or systems or situations the first aim should always be to reproduce existing cases that have been well documented by experiment. Only when a modeling environment stands the test of scrutiny against reality, one should think of applying the model to unknown situations that cannot be reproduced in the lab. In the present contribution we will present some examples of recently investigated real atomic or microstructures in solid state materials and of which the understanding could severely be improved by modeling on different length scales from the atomic to the continuum.

The experimental observations are in most cases performed with transmission electron microscope (TEM) instruments which enable magnifications up to a few million times with resolutions down to one tenth of a nanometer, i.e., well below the interatomic distances in most solids. The effective nature of the technique implies that one observes a sort of 2D transformation of the internal structure (not exactly a projection, but close) with the actual image also depending on the imaging conditions such as focus of the objective lens and thickness of the sample. The latter needs to be extremely small, i.e. at least below 100 nm and for some cases even below 10 nm, and for this special sample preparation techniques need to be applied. On one occasion, the result of a three-dimensional slice-and-view technique obtained with a dual-beam scanning electron microscope (SEM) plus focused ion beam (FIB) instrument will be discussed.

Although of course many different materials could be used as examples for the present purpose, alloy systems active in the field of shape memory or superelastic components are a very good candidate as aspects on many different length scales play important roles in these systems. Indeed, the physics (electronic structure, thermodynamics, …) of the stability of the high temperature austenite versus low temperature martensite basic lattice structures determines not only the symmetry of these structures but also the transformation temperatures and their dependencies on, e.g., composition. Here discrete atomic scale modeling (e.g., density functional theory (DFT)) can be relevant to unravel the influence of different parameters such as electron density or distribution and bonding on the stability of the different structures and thus on the displacive (and sometimes more complex) transformation processes. On the next level the symmetry of martensite dictates the number of variants and austenite-martensite and martensite-martensite interfaces which in its turn leads to a variety of microstructures that can be modeled by different, usually continuum level methods. Modeling can also be used to investigate the growth of precipitates in a matrix and of the effect of that precipitate on the surrounding matrix and in the present contribution we will primarily focus on examples involving precipitates in different shape memory alloys, with the focus on Ni-based systems.

2. Precipitation in NiTi

In the near-equiatomic NiTi system, which is often used for medical applications like stents and orthodontic wires [1] the crystal transforms from a cubic (B2) to a monoclinic (B19’) phase. This transformation can occur upon cooling or under the influence of an applied stress, in which case large strains might be obtained that can be fully recovered without plastic deformation. The properties of this transformation such as transformation temperature, number of transformation steps and whether it is superelastic or not are strongly influenced by the presence of Ni_4Ti_3 precipitates [2]. These precipitates have an ordered crystal structure and occur in the matrix after an appropriate heat treatment. They are enriched in Ni and have an estimated Ni:Ti = 4:3 composition ratio. The structure of these precipitates was first proposed by Tadaki *et al.* to be rhombohedral with spacegroup R-3 [3]. A morphological study by the same authors reveals a lens shape with 8 orientation variants.

Fig 1a is a typical conventional TEM image of Ni_4Ti_3 lens shaped precipitates embedded in the matrix and oriented along different families of {111} planes. Depending on the annealing conditions (exact temperature and time) the precipitates will be larger and further apart or smaller and closer together. The particular lens shape of the precipitates is dictated by the contraction of the lattice in the direction perpendicular to the central plane of the disc of the lens. This contraction is made possible by the replacement of one Ti atom by one Ni atom and the subsequent reshuffling of atoms in the planes parallel to the central disc: Fig 1b shows a top view (i.e., looking down on the disc of the precipitate) of the refined structure revealing these shuffles. The latter was found by applying a novel technique of multi-slice least-squares optimization of electron diffraction intensities obtained from these nano-scaled precipitates [4]. Although this results from a relatively important composition change (i.e., with respect to the matrix) and although it implies a rather severe lattice change, only very small changes are observed in the fine structure of electron energy loss (so-called ELNES) spectra, which could be confirmed by density-of-states (DOS) calculations, indicating very little if any charge transfer at all [5]. The Young’s modulus, on the other hand, does change considerably, as could be shown by measurements of the position of the maximum of the plasmon peak in the low loss part of the energy loss spectrum, as seen from fig 1c. Following the criterium designed by Oleshko and Howe [6] values of 124 GPa and 175 GPa for the matrix, respectively precipitate, were obtained [5], showing a much harder precipitate in comparison with the matrix.

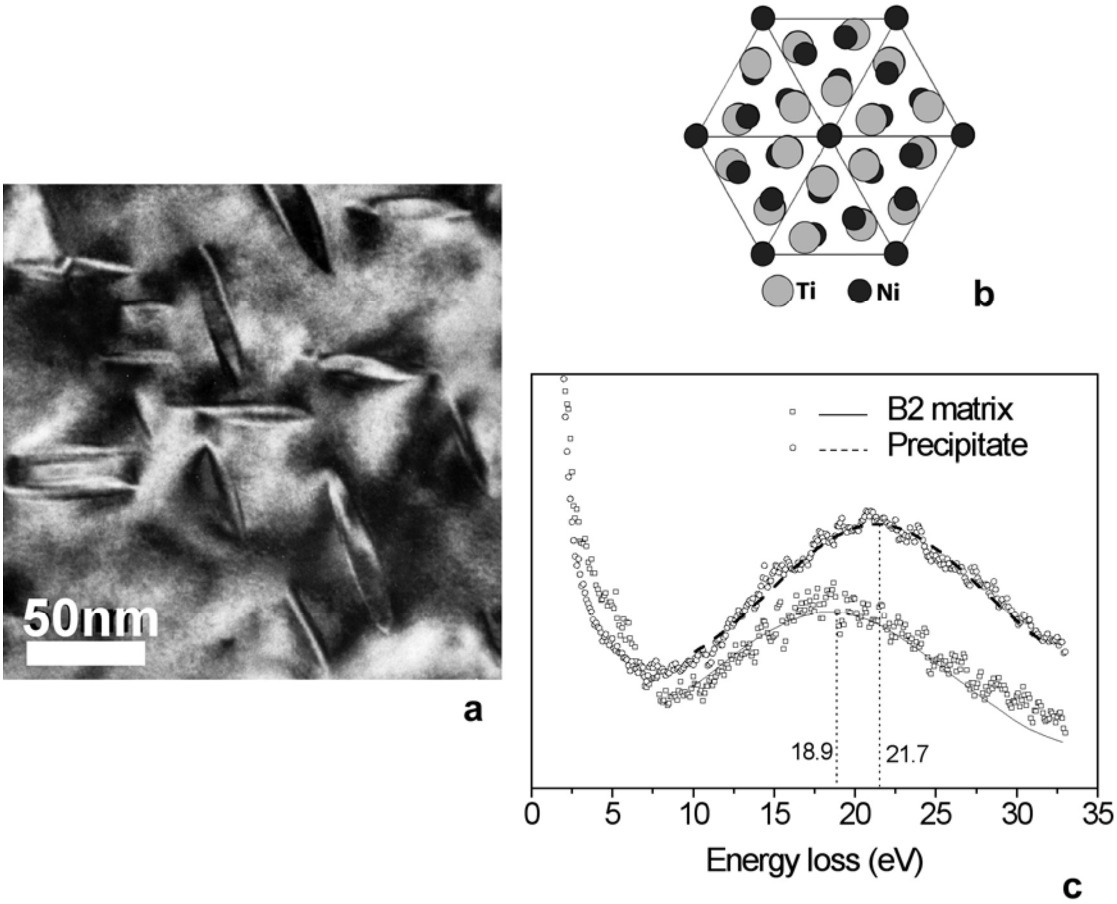

Figure 1. (a) Conventional TEM image of Ni_4Ti_3 lens shaped precipitates embedded in the NiTi matrix. (b) Projected structure of the refined structure of Ni_4Ti_3 in the $[111]_R$ direction. (c) Low loss part of the EELS spectrum showing the difference in the plasmon peaks between matrix and precipitate.

As a result of the contraction of the precipitate, the austenite matrix close by the central disc of the precipitate will be expanded (seen as strain contrast in fig 1a) which in turn will possibly affect the ensuing martensitic transformation when the material is cooled or strained. Moreover, the enrichment of Ni in the precipitate will decrease the Ni amount in the matrix in the vicinity of the precipitate and again this can have a profound influence on the martensitic transformation temperature [1]. So in order to gain insight into these different aspects of the growth of these precipitates we performed quantitative analyses of the strain and concentration gradients in the matrix surrounding the precipitates. Fig 2 shows a deformation gradient measured along the $[101]_{B2}$ direction of the NiTi matrix in between two nanoscale precipitates. The maximum deformation mounts to about 1.2% above the normal matrix lattice parameter (indicated by the horizontal dashed line in the graph on the right) and rapidly decreases after about 10 nm away from the precipitate-austenite interface. In between the precipitates there is a region of no deformation of about 20 nm. The measured deformation accounts for the total amount of strain necessary to accommodate the observed precipitates (when assuming a symmetric situation on either sides of the precipitates). These measurements were performed on high resolution images revealing the atomic lattices of the respective structures so that interplanar lattice spacings can directly or indirectly be measured [7].

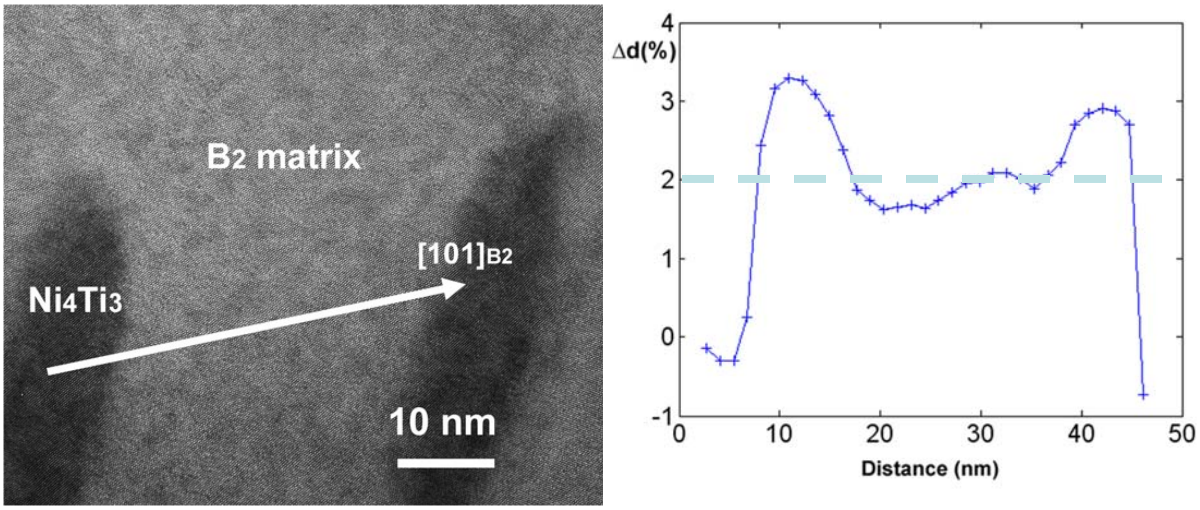

Figure 2. Deformation of the NiTi matrix as measured along the $[101]_{B2}$ direction between two small Ni_4Ti_3 precipitates

By performing spectroscopic measurements with nanoprobe or filtering techniques, concentration gradients revealing Ni depletion can be found. Regions between 10 and 150 nm wide, depending on the size of the precipitate, are depleted in Ni due to the Ni-enrichment of the precipitate: Ni/Ti ratios down to 0.94 instead of the nominal 1.04 of the matrix can be found in these areas. Again, quantification shows that these regions can provide all the Ni needed to form the precipitates [8]. For both strain and composition gradient cases, these new nanoscale quantifications may provide data that can allow for better modeling of the influence of the Ni_4Ti_3 precipitates on the martensitic transformation and thus the shape memory and superelastic behaviour of this material.

Although TEM imaging, diffraction and spectroscopy can provide a wealth of information on the structure and chemistry and electronic nature of the material, obtaining true three-dimensional information has always been a remaining challenge for microscopists working in micro- and nanoscale materials sciences. With recent evolutions of tomography, however, important steps have been taken to overcome technological as well as conceptual problems so that new results are appearing revealing the internal 3D nature of solid state materials. In fig 3 an example of again the same precipitates, but now allowed to grow much larger, is shown in which a first glance is presented into the volume configuration of these lens shapes. This result was obtained by the slice-and-view technique in which a three-dimensional bulk piece of material of NiTi containing relatively large Ni_4Ti_3 precipitates is sliced away by a focused ion beam with imaging by a scanning electron microscope after every slicing. The stack of images is then afterwards combined to form a 3D volume picture box from which different types of measurements such as volume fractions, relative orientations, cuttings, etc. can be obtained. From the present image it can, e.g., be seen that the precipitates can truly intersect, which is sometimes hard to conclude from 2D images. Of course these new possibilities for 3D imaging open new ways for interaction with modeling programs.

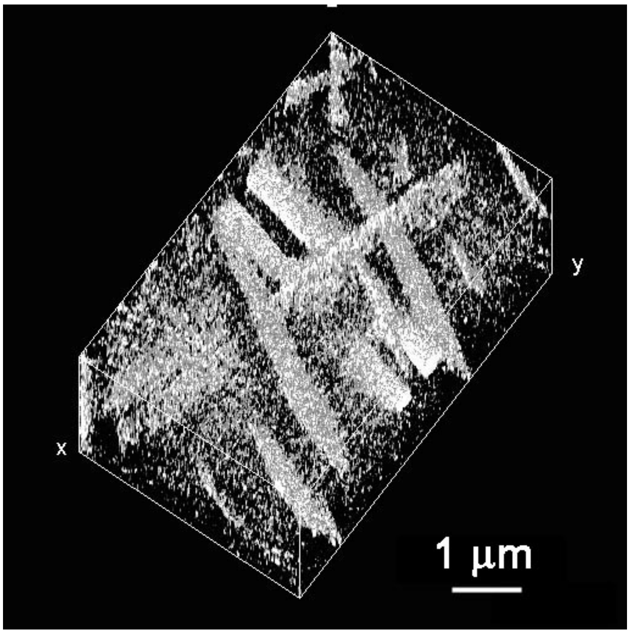

Figure 3. First 3D view of the Ni_4Ti_3 precipitates.

Instead of controlling the characteristics of the alloy by changing the composition or thermal treatment, thermomechanical treatments can even further improve the functional properties. Amongst these, low temperature annealing following appropriate cold deformation is one of the effective methods for controlling shape memory properties. Freshly rolled material shows texture of nanoscale grains and small amorphous bands in the rolling direction while in annealed material the texture is lost and the bands gradually crystallize above 400°C [9]. Further short annealing above 450°C produces Ti_2Ni precipitates while longer annealing above 500°C forms Ni_4Ti_3 precipitates. Annealing above 600°C produces Ni_3Ti_2 precipitates.

3. Precipitation in CoAlNi

Next to temperature and stress, in several novel shape memory alloys a magnetic field is used as a controlling factor of the martensitic transformation. One example is $Co_{38}Ni_{33}Al_{29}$ in which small Co rich fcc precipitates are observed in as-received material. Fig 4a shows an area with relatively large rod-like shaped precipitates with sizes about 23 nm in length and 14 nm in width. From electron diffraction it can be concluded that their crystallographic relation with the B2 matrix is of the Kurdjumov-Sachs type ($(110)_{b.c.c.}//(111)_{f.c.c.}$, $[-11-1]_{b.c.c.}//[-110]_{f.c.c.}$). Even smaller sphere-like precipitates are also observed in the same sample as seen from the high resolution image in fig 4b with fig 4c revealing the Co content in these precipitates obtained by energy filtered TEM. Again the distribution of these precipitates and their effects on the matrix will affect the martensitic transformation and thus the shape memory behaviour. Further detailed TEM investigations will provide more quantified data to exchange with modeling procedures.

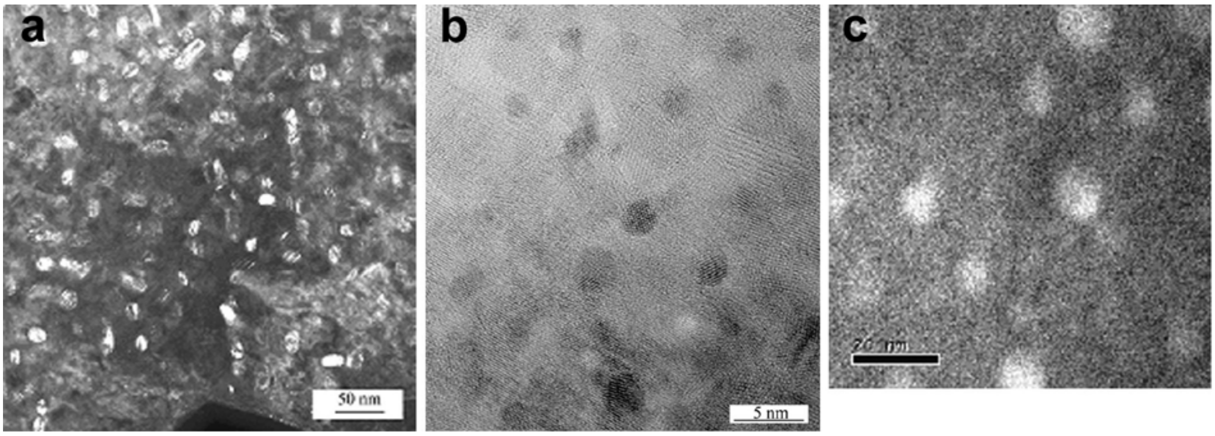

Figure 4. fcc Co rich precipitates with K-S relationship with the B2 matrix in as-received $Co_{38}Ni_{33}Al_{29}$: (a) rod-like shapes, (b) nano-spheres with (c) Co filtered image.

Acknowledgements

This work was made possible through financial support from a GOA project of the University of Antwerp on “Characterization of nanostructures by means of advanced EELS and EFTEM” a project of the National Science Foundation of Flanders on “The functional properties of shape memory alloys: a fundamental approach” and a Marie Curie Research Training Network on “Multi-scale modeling and characterization for phase transformations in advanced materials”.

References

1. K. Otsuka and X. Ren, “Physical Metallurgy of NiTi-based Shape Memory Alloys” Progress Mater. Sc. **50,** 511-678 (2005)
2. J. Khalil-Allafi, A. Dlouhy, and G. Eggeler, “Ni_4Ti_3-precipitation During Aging of NiTi Shape Memory Alloys and its Influence on Martensitic Phase transformations” Acta Mater. **50,** 4255-4274 (2002)
3. T. Tadaki, Y. Nakata, K. Shimizu, and K. Otsuka, “Crystal Structure, Composition and Morphology of a Precipitate in an Aged Ti-51at%Ni Shape Memory Alloy” JIM. **27,** 731-740 (1986)
4. W. Tirry, D. Schryvers, K. Jorissen, and D. Lamoen, “Electron diffraction structure refinement of Ni_4Ti_3 precipitates in $Ni_{52}Ti_{48}$“, Acta Cryst. (in press)
5. Z.Q. Yang and D. Schryvers, “Electron Energy-loss Spectroscopy Study of NiTi Shape Memory Alloys”, proc. ESOMAT 2006, Bochum, Germany, edited by G. Eggeler & E. Wassermann (to be published)
6. J.M. Howe and V.P. Oleshko, “Application of Valence Electron Energy-loss Spectroscopy and Plamon Energy Mapping for Determining Material Properties at the Nanoscale” Journal of Electron Microscopy, **53,** 339-351 (2004)
7. W. Tirry and D. Schryvers, “Quantitative Determination of Strain Fields Surrounding Ni_4Ti_3 Precipitates in NiTi” Acta Mater. **53,** 1041-1049 (2005)
8. Z.Q. Yang, W. Tirry, and D. Schryvers, “Analytical TEM Investigations on Concentration Gradients Surrounding Ni_4Ti_3 Precipitates in Ni-Ti Shape Memory Material” Scripta Mat. **52,** 1129-1134 (2005)
9. A.K. Srivastava, D. Schryvers, and J. Van Humbeeck, “TEM Studies on Cold-Rolled and annealed Ni-Ti Alloys” (to be published)

A Micropolar Framework for Modeling Mechanical Behavior at the Mesoscale with Taking into Account Microstructure Evolution

Igor Yu. Smolin[1], Siegfried Schmauder[2], Pavel V. Makarov[1] and
Rustam A. Bakeyev[1]

[1]Institute of Strength Physics and Materials Science SB RAS, Pr. Academicheskiy 2/1, Tomsk, 634021, Russia, e-mail: smolin@ispms.tsc.ru;
[2]Institut für Materialprüfung, Werkstoffkunde und Festigkeitslehre, Stuttgart University, Pfaffenwaldring 32, D-70569 Stuttgart, Germany.

ABSTRACT

A new model is proposed for the description of non-conventional features of mechanical behavior of metallic and composite materials with submicrocrystalline and nanostructure states, which are a result of the influence of the mesostructure of these materials. The main idea of the model is that for such materials the dislocation-based mechanisms of plastic deformation can not play the leading role due to restrictions of dimensions. On the contrary, the rotational mechanisms may play an important role, in particular in the form of grain boundary sliding. That is why using of a new degree of freedom of rotational nature is suggested in the plastic region of the deformation path. The equations of a new model for 2D plane strain case are stated. Some results of numerical calculations are presented and discussed.

1. Introduction

Microstructure investigation of materials with submicrocrystalline and nanostructures loaded in tension and compression has revealed development of rotation-shear mechanisms of plastic deformation promoted by the initial fine grain structure [1–3]. The rotational component plays the leading role in these mechanisms. Such features of mechanical behavior can not be explained by dislocation mechanisms of their deformation only. Hence, a realistic model for these materials must take into account the basic contribution of the rotational mode of inelastic deformation in the mechanical behavior. Examples of such approaches are some modifications of Cosserat continuum models [4]. They allow for taking into consideration rotational mode of deformation. The aim of this paper is to show a possible adaptation of Cosserat-like models for predicting the mechanical behaviour of materials with submicrocrystalline and nanostructures.

Some experimental and analytical investigations show that for the macroscale description the new moduli are very close to zero for most materials [5]. But it must not be the case for the other length scales. We suppose to use the ideas of Cosserat media for the description of plastic deformation of submicrocrystalline and nano structured materials at the intermediate mesoscopic scale. The physical reason for such an approach is the evidence that conventional dislocation-based mechanisms of plastic deformation seem to have difficulties due to restrictions of dimensions. Whereas there are reasons to assume that the rotational mechanisms may play a very important role due to, for example, pronounced grain boundary sliding and active behavior of interfaces in such materials. This is of particular importance for the mesoscale where the influence of material internal structure can not be neglected.

2. Description of a New Model

We shall restrict our consideration to the mesoscale only with taking into account the influence of microstructure from the micro scale by means of rotational degrees of freedom. We assume that at the initial stage of loading the conventional elasticity can be adopted. There are only displacements, symmetric strain and force stress tensors, the additional moment moduli equal zero. But starting from some critical point (specified by stress or strain) plastic deformation appears. As it grows the additional moduli increase smoothly also. This results in the appearance of asymmetric force stress, couple stress, and rotational degree of freedom. Under some conditions plastic curvature can also appear that gives rise to restrictions of not only force stress but of couple stress as well. This means that the new moment moduli are not the material parameters but functions which reflect at the mesoscale averagely the development of microscopic processes in non-stable nanostructured material under loading.

Below we shall give the equations of the model for the case of 2D plane strain conditions following to [6, 7]. There are only two displacements u_1, u_2, and one independent rotation ω . The nonzero strains and curvatures as well as three equations of motion are written in Eqn 1 and Eqn 2 respectively

$$\gamma_{11} = u_{1,1},\ \gamma_{12} = u_{2,1} - \omega,\ \gamma_{21} = u_{1,2} + \omega,\ \gamma_{22} = u_{2,2},\ \kappa_{13} = \omega_{,1},\ \kappa_{23} = \omega_{,2}. \tag{1}$$

$$\sigma_{11,1} + \sigma_{21,2} = \rho\ddot{u}_1;\ \sigma_{12,1} + \sigma_{22,2} = \rho\ddot{u}_2;\ \mu_{13,1} + \mu_{23,2} + \sigma_{12} - \sigma_{21} = \rho\ell^2\ddot{\omega}. \tag{2}$$

The equation of continuity (conservation of mass) has the conventional form. We adopt the constitutive equations in the hypoelastic form (in rates)

$$\begin{gathered}\dot{P} = -K\frac{\dot{V}}{V},\quad \tilde{\dot{s}}_{11} = 2\mu\left(\dot{\gamma}^e_{11} - \frac{1}{3}\frac{\dot{V}}{V}\right),\ \tilde{\dot{s}}_{22} = 2\mu\left(\dot{\gamma}^e_{22} - \frac{1}{3}\frac{\dot{V}}{V}\right),\ \tilde{\dot{s}}_{33} = 2\mu\left(-\frac{1}{3}\frac{\dot{V}}{V}\right),\\ \tilde{\dot{s}}_{12} = (\mu+\alpha)\dot{\gamma}^e_{12} + (\mu-\alpha)\dot{\gamma}^e_{21},\ \tilde{\dot{s}}_{21} = (\mu+\alpha)\dot{\gamma}^e_{21} + (\mu-\alpha)\dot{\gamma}^e_{12},\\ \tilde{\dot{\mu}}_{13} = (\gamma+\varepsilon)\dot{\kappa}^e_{13},\quad \tilde{\dot{\mu}}_{23} = (\gamma+\varepsilon)\dot{\kappa}^e_{23},\quad \tilde{\dot{\mu}}_{31} = (\gamma-\varepsilon)\dot{\kappa}^e_{13},\quad \tilde{\dot{\mu}}_{32} = (\gamma-\varepsilon)\dot{\kappa}^e_{23}.\end{gathered} \tag{3}$$

Here $\sigma_{ij} = -P\delta_{ij} + s_{ij}$, P is pressure, s_{ij} is the deviatoric part of force stress tensor, V is the relative volume, ℓ is the radius of inertia of the media elementary volume, K and μ are bulk and shear moduli, respectively, α, γ, ε are new material parameters, $\tilde{\dot{s}}_{ij} = s_{ij} - w_{ik}s_{kj} + s_{ik}w_{kj}$ denotes the Jaumann time derivative and $w_{ij} = 0.5(\dot{u}_{i,j} - \dot{u}_{j,i})$ are the components of rotation velocity tensor (or spin). The components of couple stress tensor μ_{31} and μ_{32} are not equal to zero but they do not enter neither in the equations of motion nor in the equation of energy. Similarly to σ_{33} they are necessary to provide the conditions of plane stress in the medium. So we need only $(\gamma+\varepsilon) = \mu(\ell^e)^2$ as the modulus for couple stress. Here we have introduced a new elastic characteristic length ℓ^e.

According to our suggestion the parameters α and ℓ^e equal zero at the initial stage of deformation. After yielding we adopt the flow rule

$$\dot{\gamma}_{11}^{p} = \dot{\lambda}_{\sigma} \frac{\partial f_{\sigma}}{\partial \sigma_{11}},\ \dot{\gamma}_{22}^{p} = \dot{\lambda}_{\sigma} \frac{\partial f_{\sigma}}{\partial \sigma_{22}},\ \dot{\gamma}_{12}^{p} = \dot{\lambda}_{\sigma} \frac{\partial f_{\sigma}}{\partial \sigma_{12}},\ \dot{\gamma}_{21}^{p} = \dot{\lambda}_{\sigma} \frac{\partial f_{\sigma}}{\partial \sigma_{21}},\ \dot{\kappa}_{13}^{p} = \dot{\lambda}_{\mu} \frac{\partial f_{\mu}}{\partial \mu_{13}},\ \dot{\kappa}_{23}^{p} = \dot{\lambda}_{\mu} \frac{\partial f_{\mu}}{\partial \mu_{23}},\quad (4)$$

and the following functions of plasticity

$$f_{\sigma}(\sigma_{ij}) = 1.5\sqrt{s_{11}^{2} + s_{12}^{2} + s_{21}^{2} + s_{22}^{2} + s_{33}^{2}} - Y,\quad f_{\mu}(\mu_{ij}) = 1.5\sqrt{\mu_{13}^{2} + \mu_{23}^{2} + \mu_{31}^{2} + \mu_{32}^{2}} - Y\ell^{p}\quad (5)$$

Here we have introduced also a plastic characteristic length ℓ^{p}. According to our assumption each of the moduli α and ℓ^{e} grow with increasing of plastic strain accumulated $e^{p} = \int \frac{2}{3}\sqrt{\dot{\gamma}_{11}^{2} + \dot{\gamma}_{22}^{2} + \dot{\gamma}_{12}^{2} + \dot{\gamma}_{21}^{2}}\,dt$. In simplest case they can be assumed to equal some constants at the initial stage of plastic deformation.

3. Results of Calculations

Using a well known finite difference scheme described e.g. in [8] a computer code was written for solving the above mentioned set of dynamic equation (with taking into account inertia terms).

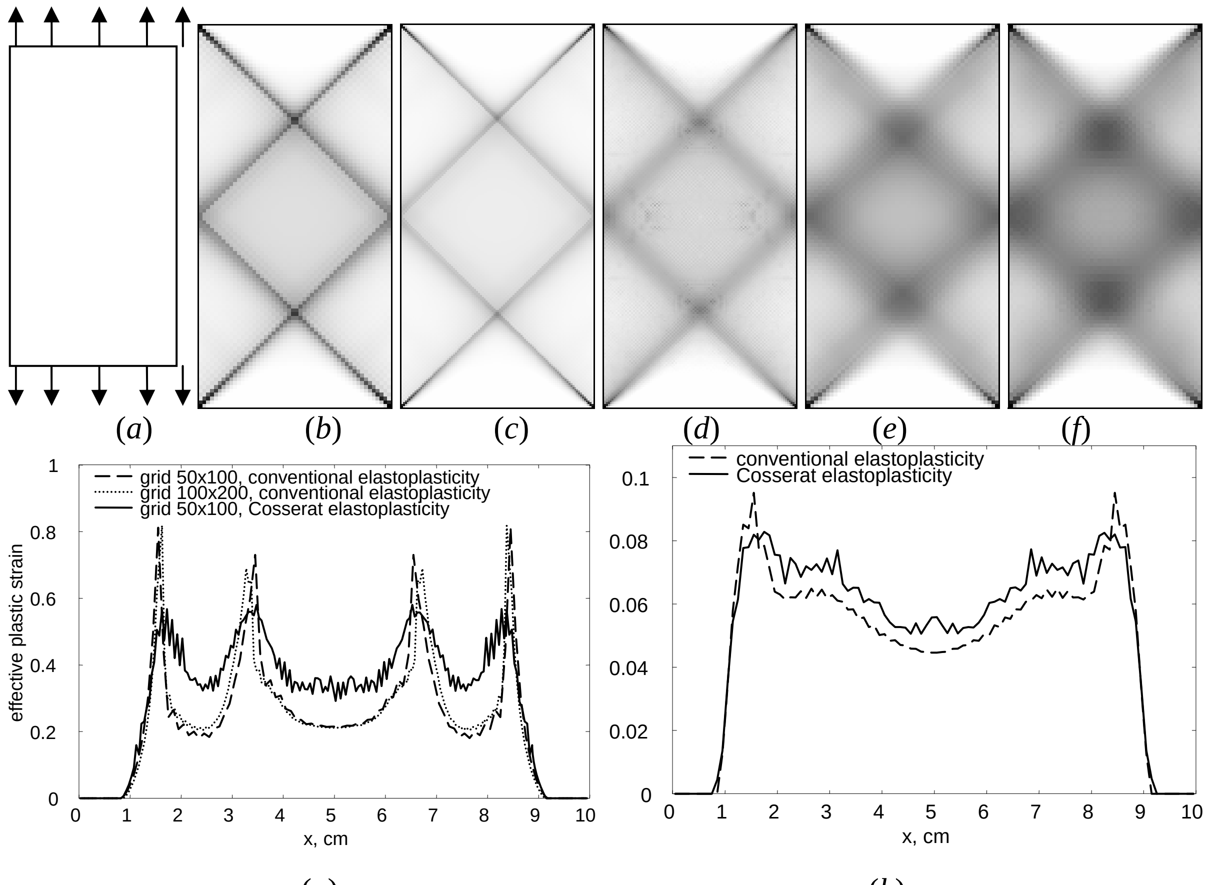

(*a*) (*b*) (*c*) (*d*) (*e*) (*f*)

(*g*) (*h*)

Figure 1. A scheme of loading (*a*) and 2D distributions of effective plastic strain for conventional elastic perfect plastic model obtained using meshes 50×100 (*b*), 100×200 (*c*), and for the proposed Cosserat model (*d*), for conventional (*e*) and Cosserat (*f*) models with hardening. Distributions of accumulated plastic deformation along the vertical section $x = 1.3$ cm for different calculation grids and ideal plastic models used (*g*) and for models with hardening (*h*).

The aim of our test calculation was to reveal the features of strain localization which the model can describe (the thickness of the bands). Stretching of an isotropic elastic perfect plastic rectangular sample 5×10 cm was considered. Upper and bottom sides were forced to move in opposite directions without possibility to move in perpendicular direction. The geometry is displayed schematically in Fig. 1, a. Such kind of loading results in stress concentration at the angular points. Four strain localization bands stem from these points. In Fig. 1 one can see the distributions of plastic strain intensity e^p (or effective von Mises strain) for different calculation grids and the model used. The material parameters were the following: $K = 166.67\,\text{GPa}$, $\mu = 76.92\,\text{GPa}$, $\alpha = 100\,\text{GPa}$, $\rho = 7.8\,\text{g/cm}^3$, $Y = 300\,\text{MPa}$, $\ell^e = \ell^p = 0.1\,\text{cm}$. The calculation results show that there is no essential mesh sensitivity in the presented numerical code for a conventional dynamical elastic perfect plastic model. Taking into account couple stress and rotations results in reduction of strain localization, the distribution of plastic strains becomes less inhomogeneous, the bands become thicker but the peak values decrease. Similar calculations carried outed for the work hardening material give the results shown in Fig. 1, e,f. Here $Y = 300\left(1 + e^p\right)^{0.2}$ MPa. One can see that in this case the bands are thicker as compared to perfect plasticity both for the conventional and Cosserast model. At the same time the difference in distributions of plastic strain for conventional and Cosserat models is smaller then in this case of the model with hardening.

Acknowledgements

The first author wishes to thank the German Research Foundation (DFG) for the financial support of his one month research stay at Stuttgart University.

References

1. Korotaev, A.D., Tyumentsev, A.N., Litovchenko, I.Yu., 2000, “Defect substructure and stress fields in the zones of deformation in high-strength metallic alloys.” Phys. Met. and Metallography. **90**, S36–S47.
2. Korotaev, A.D., Tyumentsev, A.N., Pinzhin, Yu.P., 2001, “The defect substructures and local internal stresses inherent in mesolevel plastic flows”, Theor. Appl. Fract. Mech. **35**, 163–169.
3. Valiev, R.Z., Islamgaliev, R.K., Tyumentsev, A.N., 2002, “The disclination approach to nanostructured SPD materials”, Solid State Phenom. **87**, 255–264.
4. Forest, S., 2001, “Cosserat Media”, In: *Encyclopedia of Materials: Science and Technology* (Elsevier Sciences), pp. 1715–1718.
5. Lakes, R., 1995, “Experimental methods for study of Cosserat elastic solids and other generalized elastic continua” In: *Continuum models for materials with micro-structure,* edited by H. Mühlhaus Ch. 1 (J. Wiley, New York), pp. 1–22.
6. Nowacki, W., 1986, “Theory of asymmetric elasticity”, (Pergamon, Oxford).
7. Forest, S., Sievert, R., 2003, “Elastoviscoplastic constitutive frameworks for generalized continua.” Acta Mech. **160**, 71–111.
8. Wilkins, M.L., 1964, “Calculations of elastic-plastic flow.” In: *Methods in Computational Physics*, vol. 3, edited by B. Alder, S.Fernbach, and M. Rotenberg, (Academic, New York) pp. 211–263.

Three-Dimensional Numerical Models Based on Tomogram

Ewa Soppa[1], *Gottfried Fischer*[2], *Jens Nellesen*[2], *Varvara Romanova*[3], *Horst-Arthur Crostack*[4]

[1]*Materialprüfungsanstalt Universität Stuttgart, Pfaffenwaldring 32, 70569 Stuttgart, Germany*
[2]*Dortmunder Initiative zur Rechnerintegrierten Fertigung (RIF) e.V., Joseph-von-Fraunhofer-Straße 20, 44227 Dortmund, Germany*
[3]*Institute of Strength Physics and Materials Science, SB RAS, pr.Academicheskii 2/1, 634021 Tomsk, Russia*
[4]*Lehrstuhl für Qualitätswesen (LQW), Universität Dortmund, Joseph-von-Fraunhofer Str. 20, 44227 Dortmund, Germany*

Two-dimensional finite element (FE) simulations generally do not describe the mechanical behaviour of complex materials adequately. Plane strain or plane stress conditions are simplifications which can deliver unrealistic results, if the significant details are not included. Two factors make three-dimensional calculations of the real microstructures difficult: (1) the lack of correct information about the spatial composition and (2) the enlarged number of finite elements. In this situation an important point is the thickness of the model measured in terms of the microstructural length scale. The model should be "thick" enough in order to deliver correct results, but too big thickness unnecessarily enlarges the model.

Three-dimensional calculations of the strain and stress patterns, using finite element method, were performed on the model of Al/Al2O3 composite with different thicknesses and compared with two-dimensional simulations of local strains. Moreover, local strains in tomogram-based 3D-model of an Ag/Ni-composite were simulated and compared with experimental results of plastic strains measured using the microgrid technique.

The thickness of the 3D-model of a certain structure should be at least equal to the characteristic microstructural length in order to find a realistic strain distribution on the model surface. However, a clear answer to the question "how to define the characteristic microstructural length", needs more investigations in the future. This paper tries to give a guideline, how to define the minimal dimension of the 3D-model which provides correct results concerning local strains.

Atomistic Monte Carlo simulations of diffusional phase changes

Adrian Sutton[1], *D. R. Mason*[1], *R. E. Rudd*[2]

[1]*Imperial College London, Department of Physics, Exhibition Road, SW7 2AZ, London, United Kingdom*
[2]*Condensed Matter Physics Division, L-045, Lawrence Livermore National Laboratory, 94550, Livermore, USA*

We have developed a multi-scale method to simulate diffusional phase changes in dilute binary and ternary alloys by Monte Carlo simulation of the motion of a vacancy in the presence of long-range elastic interactions [1,2]. We have applied the methodology to the formation of GP zones in Al- Cu and Al-Cu-Mg alloys. Short-range interactions are described through interatomic forces and local atomic relaxation, which lead to vacancy trapping at interfaces and misfitting solute atoms. Long-range anharmonic interactions are described through the use of the Lanczos recursion method and bias the diffusional jumps of the vacancy. The simulation is accelerated using a stochastic second order residence time algorithm. The effect of long-range elastic interactions on the microstructural development has been assessed.

* supported by EPSRC

** supported by U.S. Dept. of Energy by the Univ. of California, Lawrence Livermore National Laboratory, under Contract No. W-7405-Eng-48.

1. Stochastic Kinetic Monte Carlo algorithms for long-range Hamiltonians;, D R Mason, R E Rudd and A P Sutton, Comp. Phys. Commun. 160, 140-157 (2004).

2. Atomistic modelling of diffusional phase transformations with elastic strain;, D R Mason, R E Rudd and A P Sutton, J.Phys.: Condens. Matter 16, S2679-S2697 (2004)

Inferring the in vivo looping properties of DNA

Jose Vilar[1], *Leonor Saiz*[1], *Miguel Rubi*[2]

[1]*Computational Biology Center, Memorial Sloan-Kettering Cancer Center, 1275 York Avenue, Box #460, 10021 New York, United States of America*

[2]*Departament de Fisica Fonamental, Universitat de Barcelona, Diagonal 647, Barcelona, 08028, Spain*

The free energy of looping DNA by proteins and protein complexes determines to what extent distal DNA sites can affect each other. We inferred its in vivo value through a combined computational–experimental approach for different lengths of the loop and found that, in addition to the intrinsic periodicity of the DNA double helix, the free energy has an oscillatory component of about half the helical period. Moreover, the oscillations have such an amplitude that the effects of regulatory molecules become strongly dependent on their precise DNA positioning and yet easily tunable by their cooperative interactions. These unexpected results can confer to the physical properties of DNA a more prominent role at shaping the properties of gene regulation than previously thought.

Atomistic - continuum coupling on stepped surfaces in epitaxial growth

Axel Voigt

Research Center Caesar, Ludwig-Erhard-Allee 2, 53175 Bonn, Germany

We overcome limitations of classical step flow models, such as the Burton-Cabrera-Frank model, to far from equilibrium growth regimes by combining an atomistic description at the steps with a continuous modeling away from it. By doing so, the only remaining parameters in the model are energy barriers for individual processes of single atoms, which can be computed from first principles. We will discuss various instabilities and scaling laws for the roughening of the film. Furthermore first numerical results of the full model obtained with least-square, parametric and composite finite elements will be demonstrated.

Multi-scale modeling of dislocation pile-ups.

Roman Voskoboynikov

University of Oxford, Mathematical Institute, 24-29 St Giles', OX1 3LB, Oxford, United Kingdom

Sometimes microscopic (e.g. atomistic) considerations are too time-consuming and numerically expensive to be conducted whereas solutions of the problem at a larger scale can be obtained relatively easy. In fortunate circumstances, some details at the microscopic scale can be deduced from the large scale solution. This can happen when modelling simple configurations of large numbers of dislocations.

We illustrate this situation for dislocation pile-ups against the interface in a bimetallic solid. Provided the shear modulus of the dislocation-free half-space is larger than that of the adjacent half-space harbouring the dislocations, the interface repels the dislocations and an equilibrium dislocation distribution exists. This problem has been solved in terms of the continuum theory of dislocations [1]. However, the continuum dislocation density diverges at the interface and cannot be used for evaluation of the stress there, which the continuum model predicts to be infinite. The microscopic model on the scale of the dislocation spacing regularizes the continuum approximation and by studying this model we can approximate the equilibrium positions of the distinct dislocations and the total stress created at the interface, as a function of shear modulus, the number of dislocations and the applied loading.

[1] J.G.Kuang and T.Mura, J.Appl.Phys., 39(1968)109

Mathematical challenges in dislocation pile-up modeling

Roman Voskoboynikov

University of Oxford, Mathematical Institute, 24-29 St Giles', OX1 3LB, Oxford, United Kingdom

An accurate treatment of dislocation pile-up near the interfacial boundary is attempted. Based on the theory of pile-ups of discrete dislocations [1] in a uniform material, their equilibrium positions in a linear array against the interface in a bimetallic solid are found as roots of the solution of an ordinary differential equation (ODE) equivalent to the force balance equation in the vicinity of each dislocation. The form of the ODE depends on the continuous dislocation density in the pile-up that was found in [2]. The ODE is solved using asymptotic methods and matching at transition regions. Special attention is paid to the evaluation of the dislocation positions near the interface, where the problem is reduced to an integral equation that can be solved using the Wiener-Hopf technique. The total stress created at the interface is estimated as a function of shear modulus, the number of dislocations and the applied loading.

[1] J.D.Eshelby, F.C.Frank and F.R.N.Nabarro, Phil.Mag. 42(1951)351.

[2] J.G.Kuang and T.Mura, J.Appl.Phys. 39(1968)109

Homogenized Maxwell's Equations; A Model for Ceramic Varistors

Niklas Wellander[1], *Björn Birnir*[2]

[1]*Swedish Defence Research Agency, FOI, P.O. Box 1165, SE-581 11 Linköping, Sweden*
[2]*Department of Mathematics, University of California, 93106 Santa Barbara, USA*

Varistor ceramics are very heterogeneous nonlinear conductors, used in devices to protect electrical equipment against voltage surges in power lines. The fine structure in the material induces highly oscillating coefficients in the elliptic electrostatic equation as well as in the Maxwell equations.

We suggest how the properties of ceramic varistors can be simulated by solving the homogenized problems, i.e. the corresponding homogenized elliptic problem and the homogenized Maxwell equations. The fine scales in the model yield local equations coupled with the global homogenized equations. Lower and upper bounds are also given for the overall electric conductivity of varistor ceramics. These two bounds are associated with two types of failures in varistor ceramics. The upper bound corresponds to thermal heating and the puncture failure due to localization of strong currents. The lower bound corresponds to fracturing of the varistor, due to charge build up at the grain boundaries resulting in stress caused by the piezoelectric property of the varistor.

Studies on Meshless Thermal-Mechanical Analysis Method

LEI ZHANG

WORCESTER POLYTECHNIC INSTITUTE, 100 INSTITUTE RD, 01609 WORCESTER, United States of America

An integrated meshless thermal-mechanical analysis method is studied, with an FPM (Finite Point Method) based solidification model and an MLPG (Meshless Local Petrov-Galerkin) based thermal elastic-plastic analysis model. The MLPG method is more stable and accurate than FPM method, but it requires local background cells for the integration, which will greatly increase computation cost. To simplify the calculation of MLPG, a collocation scheme used in FPM is introduced in this study, where the radius of the cells of the inner points is set to zero. This means that the MLPG formulas on these points are only implemented once, and it is not necessary to calculate the Gauss integral points as in the original procedure. The modified method has been successfully verified and applied to the simulation of the solidification process and the thermal stress analysis of continuous casting billet in mold. The results are consistent with the measurement. It shows the characteristics of stress and strain distribution and the formation mechanism of the off-corner defects. The method is comparable in accuracy with the FEM method. The observations also show that the method is suitable for the analysis of the continuous casting process.

Hybrid Multiscale Modelling of the Propagation of Grain Boundaries in Epitaxial Growth

S. C. Hendy[1], *T. P. Schulze*[2], *Peter Zoontjens*[3,1]

[1] *MacDiarmid Institute for Advanced Materials and Nanotechnology, Industrial Research Ltd, Lower Hutt, New Zealand*

[2] *Department of Mathematics, University of Tennessee, 37996 Knoxville, USA*

[3] *School of Chemical and Physical Sciences, Victoria University of Wellington, PO box 600, 6001 Wellington, New Zealand*

A frequent defect in epitaxial growth on fcc (111) is the stacking fault. This occurs when adatom islands nucleate and grow in hcp stacking. Such islands form grain boundaries where they impinge on fcc islands. In certain conditions the grain boundaries can migrate, converting hcp islands to fcc or vice versa, which can eliminate stacking faults. Various studies [1,2] of such processes, including Kinetic Monte Carlo simulations have been carried out.

This work investigates the migration of grain boundaries and associated processes, using a hybrid multiscale model. The model decomposes the system under study into concurrently coupled Molecular Dynamics and Kinetic Monte Carlo simulations, in which the Molecular Dynamics region adaptively follows the migration of the grain boundary.

When as in this case, significant parts of the system may be treated with Kinetic Monte Carlo, the hybrid model can provide accuracy close to a full Molecular Dynamics simulation at greatly reduced computational cost. The complexity of the grain boundary makes it unsuitable for Kinetic Monte Carlo modelling. Also with the hybrid model it is feasible to study processes over longer timescales, given the cost saving compared to full Molecular Dynamics. Hence this research is expected to elucidate the mechanisms underlying the migration of grain boundaries in a range of circumstances.

[1] C. Busse et al PRL 91 056103 (2003)

[2] W.L. Ling et al PRL 95 166105 (2005)

Structure-property relations for “oriented” and “unoriented” thermoplastic elastomers

Pedro Ponte Castaneda

University of Pennsylvania, Mechanical Engineering and Applied Mechanics, 19104-6315 Philadelphia, USA

Thermoplastic elastomers (TPEs) are multiphase polymeric materials, which consist of a “soft” phase (e.g., polybutadiene) giving rise to the rubbery nature of the materials, and a “hard” glassy phase (e.g., polystyrene) yielding increased stiffness and enhanced large-deformation properties. More specifically, here we will deal with styrenic TPEs, which are ABA-triblock copolymers deriving their superior properties from a self-assembly process where the hard blocks act as anchoring points for the soft blocks in a way somewhat analogous to cross-linking in a vulcanized rubber. Because the self-assembly process takes place at the level of molecules, these materials develop a “domain” structure at the nanometer scale, or nanostructure (lamellar, double-gyroid, hexagonally distributed cylinders and BCC-distributed spheres). However, under typical processing conditions, they also develop a “granular” structure at the micron level, or microstructure, which is similar to that of metal polycrystals. Therefore, TPEs exhibit structure a two different length scales and there is growing experimental evidence that this dual structure greatly affects the overall response of macroscopic samples. Because TPEs constitute a huge industry, and are expected to replace traditional vulcanates in many applications, there is great interest in manipulating this structure to optimize their mechanical response.

We will make use of a multiscale modeling approach to characterize the strongly nonlinear dependence of the macroscopic mechanical properties of TPEs on the structure at the domain and polycrystal levels. For this purpose, variational homogenization techniques originally developed by the author will be utilized. Applications will be developed both for “oriented” (i.e., single crystal) and “unoriented” (i.e., polycrystal) samples for which comprehensive data is available for the macroscopic stress-strain response, as well as for the structure and its evolution through SAXS and TEM observations. The ultimate objective is to develop constitutive models for these materials systems, which will additionally account for the evolution of the relevant nano- and micro-structures, leading to the possible development of macroscopic instabilities.